



**Universiteit
Leiden**
The Netherlands

Structural biology of induced conformational changes

Geus, D.C. de

Citation

Geus, D. C. de. (2009, June 4). *Structural biology of induced conformational changes*. Retrieved from <https://hdl.handle.net/1887/13826>

Version: Corrected Publisher's Version

License: [Licence agreement concerning inclusion of doctoral thesis in the Institutional Repository of the University of Leiden](#)

Downloaded from: <https://hdl.handle.net/1887/13826>

Note: To cite this publication please use the final published version (if applicable).

Structural biology of induced conformational changes

Proefschrift

ter verkrijging van

de graad van Doctor aan de Universiteit Leiden,

op gezag van Rector Magnificus prof.mr. P.F. van der Heijden,

volgens besluit van het College voor Promoties

te verdedigen op donderdag 4 juni 2009

klokke 13.45 uur

door

Daniël de Geus

geboren te Utrecht

in 1977.

Promotiecommissie:

Prof. dr. J.P. Abrahams (promotor)

Prof. dr. A.M. Deelder

Dr. N. Galjart

Dr. R.B.G. Ravelli

Prof. dr. J. Brouwer

Dr. ir. P.L. Hagedoorn

Prof. dr. W.R. Hagen

Prof. dr. M.H.M. Noteborn

Prof. dr. P.C.W. Hogendoorn

Financial support:

The research described in this thesis was supported by the Netherlands Organisation for Scientific Research (NWO) and Cyttron.

Cover:

Sir Isaac Newton, the 17th- and 18th-century British mathematician and physicist, suggested that tiny layered structures were responsible for producing the iridescent color in peacock feathers (*Opticks* 1704). More recently, the coloration mechanism in peacock feathers has been revealed using a combination of optical and scanning electron microscopy [Zi et al. (2003) *PNAS* **100**, 12576-78].

Contents

Chapter 1	Introduction	1
Chapter 2	Functional proof for the translocating activity of Hsp15 in the recycling of aborted ribosomal 50S subunit-nascent chain tRNA complexes	5
Chapter 3	Characterization of a diagnostic Fab fragment binding trimeric Lewis X	23
Chapter 4	Cloning, expression, purification, crystallization and preliminary X-ray diffraction analysis of chlorite dismutase: a detoxifying enzyme producing molecular oxygen	51
Chapter 5	Crystal structure of chlorite dismutase	63
Chapter 6	Structural insight into the microtubule End Binding protein EB1 by small angle X-ray scattering: orientation of the microtubule binding and the coiled coil interacting domains	105
Nederlandse samenvatting		125
General acknowledgements		129
List of publications		131
Curriculum vitae		133

Chapter

1

General introduction and outline

Chapter 1

Before the 19th century it was generally believed that the molecules of life could only be produced by organisms. The synthesis of urea in 1828 by Friedrich Wöhler was a major breakthrough showing the possibility of artificial production of organic compounds. Moreover, this finding was a milestone on the road to the belief that, just like non-life, also life is subject to the laws of science. Many years later, life has been defined as the outcome of an elaborate organization based on trivial ingredients[‡] and ordinary forces¹.

Living systems are set aside from the rest of matter by some unique properties. They duplicate, transform energy, metabolize compounds and control their exchanges with the surrounding environment. Moreover, they are capable to maintain their internal equilibrium when changes occur in the outer world: a process commonly known as homeostasis. Various unrelated types of disturbance can be discriminated, yet all change the optimal functioning conditions of the organism and will be opposed by appropriate action.

A well known cellular stress factor is a raised temperature (or heat shock) which causes denaturation of proteins. The adaptation consists of up-regulation of chaperone and heat shock proteins (Hsps). Hsps are present in all organisms assisting the efficient folding of newly synthesized proteins and maintaining proteins in a stable conformation, preventing their aggregation under stress conditions. In **chapter 2** the recycling of ribosomal 50S-nc-tRNA complexes by Hsp15 is described. This small heat shock

[‡] Living matter consists of relatively few common chemical elements (C, H, N, O, P and S supplemented with some trace elements)

protein is extremely up-regulated during thermal stress and has a much higher affinity for blocked 50S•nc-tRNA ribosomal subunits compared to empty 50S subunits. Heat shock causes translating ribosomes to dissociate prematurely, resulting in 50S subunits that carry tRNA covalently attached to the nascent chain of an incomplete protein (50S•nc-tRNA). The 50S•nc-tRNA subunits cannot re-initiate protein synthesis, so translational reactivation of a heat shock aborted 50S•nc-tRNA complex requires removal of the nc-tRNA by severing of the aminoacyl ester bond between these moieties. Cryo-EM reconstructions and functional assays show that Hsp15 reversibly translocates the tRNA moiety from the A- to the P-site of stalled 50S subunits. By stabilising the tRNA in the P-site, Hsp15 indirectly frees up the A-site, allowing a release factor to land there and cleave off the tRNA.

Another stress factor for an organism is a viral, bacterial or parasitical attack. The host organism will attempt to defend itself by raising an immune response against the foreign material. **Chapter 3** describes the monoclonal antibody 54-5C10-A, which is used to diagnose the parasitic disease schistosomiasis in humans. The parasitic nematode *Schistosoma mansoni* expresses oligomers of Lewis X trisaccharides, a carbohydrate that normally functions, in its monomeric form, as human cell-cell interaction mediator. Our structural and biochemical studies indicate a radically different mode of binding compared to Fab 291-2G3-A, an antibody specific for monomeric Lewis X, thus providing a structural explanation of the diagnostic success of 54-5C10-A. **Chapter 4 and 5** present the bacterial detoxification enzyme chlorite dismutase. Metabolising strong oxidizing agents like perchlorate

Chapter 1

(ClO_4^-) and chlorate (ClO_3^-) as electron acceptors, the bacterium *Azospira oryzae* forms the toxic chlorite (ClO_2^-) as a byproduct. To prevent *Azospira* from poisoning itself, this chlorite waste is converted very efficiently into chloride and molecular oxygen. The X-ray structure of the chlorite dismutase gives insight into the active site of the first described haem enzyme performing O-O bond formation as its primary task. Furthermore, native mass spectrometry data demonstrate that the oligomeric organization of chlorite dismutase is different than the hitherto supposed tetramer.

In **chapter 6** analytical ultracentrifugation, gelfiltration and small-angle X-ray solution scattering (SAXS) experiments have been used to obtain the low resolution structure of full length EB1. The end-binding protein 1 (EB1) is a highly conserved group of proteins that uses its localization at the plus-ends of microtubules to regulate microtubule dynamics and chromosome segregation. Our results show that the distance between the centers of gravity of the two globular microtubule binding domains of EB1 is about 80 to 90 Å. This is close to the distance between adjacent tubulin subunits along a microtubule protofilament. Binding of EB1 could stabilize the GTP or GDP-Pi conformation of tubulin and promote the lateral interactions of protofilaments when they assemble into the microtubule lattice.

References

1. Palade, G.E. (1964). The organization of living matter. *Proc. Natl. Acad. Sci. U. S. A* **52**, 613-634.

Functional proof for the translocating activity of Hsp15 in the recycling of aborted ribosomal 50S subunit-nascent chain tRNA complexes[†]

Daniël C. de Geus, Linhua Jiang, Christiane Schaffitzel, Rouven Bingel-Erlenmeyer, Nenad Ban, Philipp Korber, Roman I. Koning, Jasper R. Plaisier, Jan Pieter Abrahams

[†] This chapter is based on “Recycling of aborted ribosomal 50S subunit-nascent chain tRNA complexes by the heat shock protein Hsp15.” Linhua Jiang, Christiane Schaffitzel, Rouven Bingel-Erlenmeyer, Nenad Ban, Philipp Korber, Roman I. Koning, Daniël C. de Geus, Jasper R. Plaisier, Jan Pieter Abrahams *J. Mol. Biol.* (2008). It focuses on Daniël de Geus’ contribution to this paper, which was to provide functional proof for a mechanism that was deduced from structural data.

Abstract

When heat shock prematurely dissociates a translating bacterial ribosome, its 50S subunit is prevented from re-initiating protein synthesis by tRNA covalently linked to the unfinished protein chain that remains threaded through the exit tunnel. Hsp15, a highly up-regulated bacterial heat shock protein, is essential for re-activating such dead-end complexes. Here we show with functional assays that Hsp15 translocates the tRNA moiety from the A- to the P-site of stalled 50S subunits to expose the aminoacyl ester bond between tRNA and nascent chain to ribosome mediated cleavage. These assays complement cryo-EM reconstructions of the complex of the 50S•nc-tRNA sub-unit in the absence and in the presence of Hsp15. By stabilising the tRNA in the P-site, Hsp15 indirectly frees up the A-site, allowing a release factor to land there and cleave off the tRNA. Such a release factor must be stop codon independent, suggesting a possible role for a poorly characterised class of putative release factors that are up-regulated by cellular stress, lack a codon recognition domain and that are conserved in eukaryotes.

2.1 Introduction

Heat shock up-regulates many proteins that function as chaperones or as proteases. Heat shock also increases the transcription of the small heat shock protein Hsp15, which is an RNA/DNA binding protein. It targets aborted ribosomal 50S subunits rather than misfolded proteins¹. Its ~50-fold transcriptional increase is even higher than the upshift in expression of well-characterized heat shock proteins such as GroEL/ES, DnaK and ClpA, indicating the high relevance of Hsp15 for adapting to thermal stress².

Translating ribosomes can dissociate prematurely upon heat shock, resulting in 50S subunits that carry tRNA covalently attached to the nascent chain (nc-tRNA) of an incomplete protein that is threaded through the 50S exit tunnel[‡]. These 50S•nc-tRNA subunits cannot re-initiate protein synthesis and their accumulation would constitute a problem for the cell. In the intact 70S ribosome, the tRNA is released from the nascent chain by a release factor, which binds in the vacant A-site to cleave the peptidyl esterbond. All well-characterised release factors are stop codon dependent³⁻⁵, yet the release factor that recycles blocked 50S subunits must be stop codon-independent, as there is no stop codon in the dissociated 50S subunit.

Rescuing such blocked 50S subunits requires the presence of Hsp15, which specifically binds blocked 50S•nc-tRNA ribosomal subunits with high affinity ($K_d < 5$ nM), while its affinity for empty, functional 50S subunits is

[‡] Presumably tRNA attached to a short peptide would still dissociate, hence we use the term 'nc-tRNA' throughout the chapter to distinguish it from tRNA attached to very short peptides.

significantly lower⁶. It was established that Hsp15 is not a release factor, since the 50S•nc-tRNA•Hsp15 is stable and the tRNA moiety is not released⁷. It remained unclear how Hsp15 discriminates between active and aberrantly terminated 50S subunits and how it contributes to recycling blocked, non-functional 50S•nc-tRNA complexes.

In this chapter, puromycin nascent chain release assays are described which were used to prove a conjecture based on electron microscopy (EM) 3D reconstructions of the complexes involved. These EM results are reported in detail elsewhere⁸. Briefly, the structure of the complex of the 50S•nc-tRNA subunit both in the absence and presence of Hsp15 were determined by cryo-EM and single particle analysis to resolutions of 14 and 10 Å, respectively. The 3D models of these complexes were reconstructed and X-ray structures of 50S, tRNA and Hsp15 were subsequently fitted into EM density maps as described elsewhere⁸. To summarize the cryo-EM results, the 50S•nc-tRNA reconstruction revealed clear additional density located at the A site (Figure 1A), corresponding to the tRNA covalently attached to the nascent polypeptide chain that is extending through the ribosomal exit tunnel. In contrast, the tRNA appears at the P site in the 50S•nc-tRNA•Hsp15 reconstruction (Figure 1B).

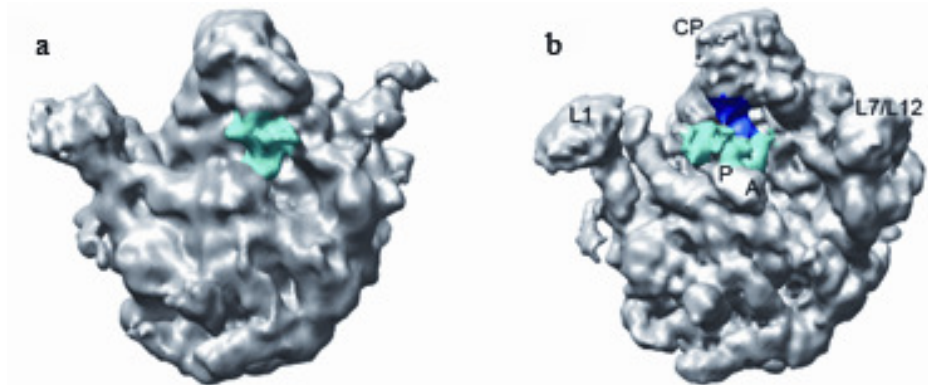


Figure 1 Reconstructions of: **a**) the 50S•nc-tRNA complex (the density of tRNA is in cyan, 14 Å resolution) and **b**) the 50S•nc-tRNA•Hsp15 complex (the density of tRNA is in cyan and of Hsp15 in blue, 10 Å resolution). The Central Protuberance (CP), the L1 and L7/L12 domains and the P- and A-sites are indicated.

2.2 Experimental procedures

2.2.1 Preparation of 50S•nc-tRNA complexes

The plasmid pUC19Strep3FtsQSecM was transcribed *in vitro* and translated in a membrane-free *E. coli* cell extract as previously described⁷. The translation mix was loaded directly onto a 38 ml sucrose gradient (10 – 50 % sucrose in 50 mM Hepes-KOH, 100 mM KOAc, 0.3 mM Mg(OAc)₂, pH 7.5) and centrifuged for 15 hours at 23000 rpm, 4°C in a SW32 Ti rotor (Beckman Coulter). The 50S fraction was loaded onto a 300 µl Strep-Tactin sepharose column (IBA, Göttingen Germany) equilibrated with buffer 1 (20

mM Hepes-KOH, 150 mM NH₄Cl, 1 mM Mg(OAc)₂, 4 mM β-mercaptoethanol, pH 7.5) at 4°C, eluted with 2.5 mM desthiobiotin in buffer 2 (20 mM Hepes-KOH, 150 mM NH₄Cl, 12 mM Mg(OAc)₂, 4 mM β-mercaptoethanol, pH 7.5) and pelleted by ultracentrifugation (3 h, 55000 rpm, 4°C, TLA-55 rotor (Beckman)). The 50S•nc-tRNA (50S-nc) pellet was dissolved in buffer 2 by gentle shaking on ice.

2.2.2 Purification of Hsp15

The plasmid pTHZ25¹ was transformed in *E. coli* BL21(DE3) and the cells were cultured as described. Cells were ruptured by two passages through an EmulsiFlex-C5 homogenizer (Avestin) at 15000 psi and the lysate cleared by ultracentrifugation (1h, 18000 rpm, 4°C, Ti70 rotor (Beckman)). The supernatant was loaded onto a Q sepharose FF column (GE Healthcare) and a phenyl-sepharose column (GE Healthcare) as described¹. The purified protein was dialyzed against 30 mM Hepes-KOH, 1 mM EDTA pH 7.0, concentrated with a Centriplus concentrator (MWCO 3 kDa, Amicon), flash-frozen and stored at -80 °C.

2.2.3 Binding assays of Hsp15

15 μg 50S-nc, 50S and 70S were incubated in a 1:1 and 1:10 molar ratio with purified Hsp15 in buffer 3 (20 mM Hepes-KOH, 100 mM NH₄Cl, 25 mM Mg(OAc)₂, pH 7.5) on ice for 30 min. The mix was centrifuged 5 min at 14000 rpm in a table top centrifuge at 4°C and then loaded onto a 1.5 ml

sucrose cushion (30% w/v sucrose in buffer 3). The ribosomes and ribosomal subunits were pelleted by ultracentrifugation (5 h, 55000 rpm, 4°C, TLA-55 rotor (Beckman)). The ribosomal pellet was quantified and loaded onto a 16% SDS gel.

2.2.4 Puromycin assay

60 nM 50S•nc-tRNA•Hsp15 complex in buffer 2 (or buffer 2 with increased Mg^{2+} concentration to 100 mM to favour Hsp15 dissociation) was incubated with 2 mM puromycin for 3 h at 37 °C. Samples at 45 min intervals were withdrawn, mixed with an equal volume of loading buffer and separated on a low-pH SDS-based Tris-acetate gel to minimize hydrolysis of the ester bond linking tRNA to the nascent chain⁹. Immunodetection of the nascent chain was carried out on PVDF membrane using a Strep-tag monoclonal antibody conjugated to horseradish peroxidase (IBA, Göttingen Germany). Detection was performed by electrochemiluminescence and spots on the X-ray films were quantified densitometrically.

2.3 Results and Discussion

2.3.1 Generation of stable 50S•nc-tRNA complexes

Stable, homogenous 70S•nc-tRNA complexes were generated by *in vitro* transcription and *in vitro* translation using the plasmid pUC19Strep3FtsQSecM with an N-terminal triple Strep-tag for affinity purification⁷. To span the ribosomal exit tunnel, the FtsQ sequence and the

17 amino acids-long SecM translational arrest motif were C-terminally fused to the affinity tag. The SecM peptide interacts tightly with the ribosomal tunnel¹⁰ and thereby significantly stabilizes the 70S•nc-tRNA complexes, without the need of using chloramphenicol antibiotic. After *in vitro* translation, the translating ribosomes were loaded onto a sucrose gradient with low concentration of magnesium ions causing dissociation of the 70S•nc-tRNA complexes into 50S•nc-tRNA and 30S (Figure 2A) complexes. The 50S•nc-tRNA complexes were further purified and separated from empty 50S using a Strep-Tactin sepharose column and finally pelleted by ultracentrifugation. The complex with Hsp15 was reconstituted by adding a 20-fold molar excess of Hsp15.

Binding assays confirmed that Hsp15 neither binds 70S ribosomes nor empty 50S subunits under the assay conditions (Figure 2B). However, a low level of binding of Hsp15 to empty 50S subunits was observed, when the sucrose cushion was omitted from the sedimentation assay (not shown). This is in agreement with the previously described non-specific nucleic acid binding activity of Hsp15¹. Hsp15 only had a high affinity for 50S subunits when they contained nc-tRNA. Also, Hsp15 had to be present in a 1:10 molar ratio (Figure 2B).

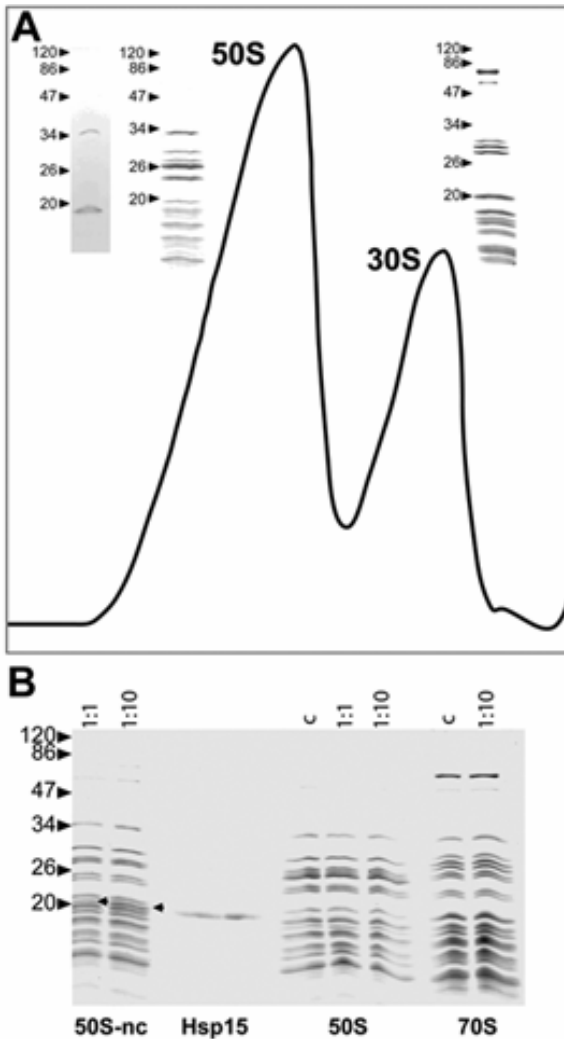


Figure 2

a) Preparation of 50S•nascent chain-tRNA complexes (50S-nc/50S•nc-tRNA).

Sucrose gradient profile of an in vitro translation reaction in the presence of 0.3 mM Mg(OAc)₂. The two peaks (50S and 30S) are analyzed on a Coomassie-stained SDS gel. The presence of the nascent chain in the 50S is shown by Western blotting (left side) using Streptactin-alkaline phosphatase conjugate. The upper band at ~34 kDa corresponds to nc-tRNA, the lower band to the nascent peptide alone. **b)** Binding assay of Hsp15. Binding of purified Hsp15 to 50S-nc, to 50S and to 70S was analyzed by ribosomal pelleting through a sucrose cushion.

As a control (indicated with c), 50S and 70S was loaded alone. Hsp15 did not migrate through the sucrose cushion (not shown). Hsp15 was added in a 1:1 and 1:10 molar ratio. Hsp15 was found only in the pellet of 50S-nc as indicated with arrows in lanes 1 and 2; in the 1:1 molar ratio somewhat less Hsp15 was recovered. As a positive control, 100 ng Hsp15 was loaded onto the SDS gel.

2.3.2 Functional assay of Hsp15 induced tRNA translocation

The P-site specific antibiotic puromycin is a functional equivalent of a stop codon independent release factor. Mimicking the 3' end of aminoacyl tRNA at the A-site, it binds at the A-site and allowing the ribosome to cleave off P-site tRNA from the nascent chain, which is transferred to the A-site moiety. Puromycin is used in functional assays to distinguish P-site tRNA from A-site tRNA and establish A-site occupancy. It was established that puromycin abolishes binding of Hsp15 to 50S•nc-tRNA complexes in cell extracts⁶. Presumably, puromycin released the tRNA from the 50S subunit and the resulting empty 50S subunits would no longer have a high affinity for Hsp15. This observation already indicated that the tRNA must reside in the P-site in the 50S•nc-tRNA•Hsp15 complex in cell extracts. Here we show that no additional factors were involved: also in highly purified 50S•nc-tRNA•Hsp15 samples, puromycin was able to cleave off the nascent chain (Figure 3).

N-acetylated Phe-tRNA_{Phe} is a nc-tRNA homologue that can freely diffuse into and out of the P-site of 50S subunits, where can react with A-site bound puromycin. This reaction proceeds optimally at 100 mM Mg²⁺ in isolated 50S subunits, but is slower at lower Mg²⁺ concentrations¹². However, for the 50S•nc-tRNA•Hsp15 we found the opposite effect: raising the Mg²⁺ concentration *reduced* the puromycin reactivity.

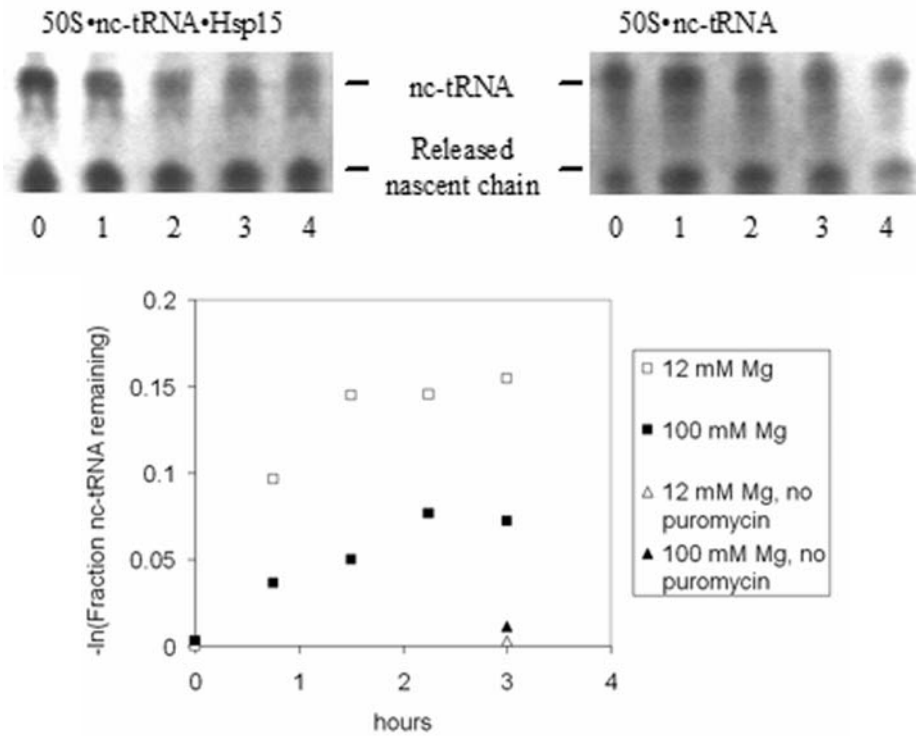


Figure 3 a) Puromycin reaction of 50S•nc-tRNA•Hsp15 at 37 °C in 12 mM and 100 mM Mg²⁺. Controls without puromycin do not show any cleavage of the ester bond between tRNA and nascent chain, even after 3 hours of incubation. At the outset of the reaction, there is already a substantial amount of released nascent chain present (lower band). b) The negative natural logarithm of the remaining nc-tRNA was plotted against the incubation time. In a first order reaction this is expected to be a straight line, which we indeed observe for 2-3 hours after initiating the reaction. The data shown in a) are plotted. The puromycin induced cleavage of nc-tRNA was determined by measuring the increase of the intensity of the band corresponding to the released nascent chain as a fraction of the total intensity corresponding to nascent chain (whether bound to tRNA or not). The higher reactivity at 12 mM Mg²⁺ can be explained by the fixation of tRNA at the P-site by Hsp15 at this Mg concentration. The experiments were performed in duplicate.

The cryo-EM structure provided a straightforward explanation of this observation. At 100 mM Mg^{2+} , Hsp15 dissociates more easily from 50S•nc-tRNA complexes⁶. If Hsp15 is essential for stabilising the tRNA moiety in the P-site, as suggested by the structures, its dissociation from the 50S•nc-tRNA•Hsp15 complex should result in a relocation of the tRNA to the A-site, where it cannot be cleaved by puromycin.

2.3.3 Recycling ribosomal complexes by Hsp15: discussing the model

Translational reactivation of a heat shock aborted 50S•nc-tRNA complex requires removal of the nc-tRNA by severing of the aminoacyl ester bond between these moieties. In the cell, this hydrolysis requires the tRNA to be located in the P-site and a release factor to bind at the vacant A-site. In the absence of Hsp15, the tRNA moiety of nc-tRNA, although being somewhat disordered, was clearly located in the A-site (Figure 1A). This A-site location of the tRNA moiety is further corroborated by a puromycin assay (Figure 3). At first sight this is a surprising result, as in the complete 70S ribosome, peptidyl tRNA has a preference for the P-site. However, in the 70S complex, peptidyl tRNA is stabilized at the P-site by extensive contacts with the mRNA, 16S RNA and protein residues of the 30S subunit (e.g., Ref. 13) and these interactions are obviously absent in the 50S•nc-tRNA complex. On the other hand, the A-site location of the tRNA is stabilized by additional interactions with residues of the 50S subunit that lie outside the peptidyl transfer center, e.g. helix 38 of the ‘A-site Finger’¹⁴. Apparently, in the absence of the 30S subunit, these interactions are strong enough to direct

the tRNA moiety in the 50S•nc-tRNA complex to the A-site. Our observation explains why the 50S•nc-tRNA complex cannot be recycled: a tRNA moiety in the A-site prevents release factors from binding and severing the aminoacyl ester bond between the tRNA and the nascent chain. Hsp15 located the tRNA in the P-site. Locked in the P-site, the CCA end of the nc-tRNA is optimally positioned in the peptidyl transferase centre for hydrolytic attack of its aminoacyl ester bond by a release factor. The translocation of the tRNA to the P-site in the Hsp15 containing complex is in full agreement with the puromycin assay (Figure 3) and with puromycin sensitivity of dissociated translating ribosomes in cell lysates⁶. Translocation of the nc-tRNA from the A- to the P-site would allow a release factor to bind in the A-site. In the 70S ribosome, this translocation requires energy: EF-G hydrolyses GTP in the process. Our results indicate that in the absence of interactions with the 30S subunit, the binding energy of the Hsp15 to the 50S•nc-tRNA complex is sufficient to induce translocation.

Which release factor cleaves the aminoacyl ester bond between tRNA and nascent chain in the 50S•nc-tRNA•Hsp15 complex? All well-characterized release factors interact with translating ribosomes and mimic a tRNA molecule. They all have a stop-codon recognizing domain at one end and a GGQ peptidyl hydrolase domain at the other end, which interacts with the peptidyl transferase center of the ribosome^{3-5;15}. In the blocked 50S•nc-tRNA•Hsp15 complex there is no stop-codon. The putative 15 kD, 140 aminoacid protein with unassigned function encoded by the *yaeJ* gene in *E. coli* is a likely candidate to serve as a release factor for 50S•nc-tRNA-

Hsp15 complexes.. In *E. coli* *yaeJ* is transcribed immediately ahead of *cutF/nplE*, a factor involved in the extracytoplasmic stress response; both apparently belong to the same stress-induced operon¹⁶. YaeJ contains the conserved GGQ peptidyl hydrolase domain, but lacks a stop-codon recognizing domain. Due to the presence of the GGQ motif, YaeJ is placed in the same cluster of orthologous groups as the release factors RF1 and RF2¹⁵. Thus, YaeJ could bind to the A site of the 50S•nc-tRNA•Hsp15 complex and hydrolyze the peptidyl-tRNA ester bond without needing a stop codon recognizing domain.

Residues 10 to 112 of YaeJ have a significant 29% identity and 55% similarity with the small human protein ICT1, indicating both share the same fold. ICT1 is a 23.6 kD protein with unknown function, but it becomes more highly expressed upon neoplastic transformation of colon epithelial cells¹⁷ and is predicted with high significance (P>0.9) to be targeted to mitochondria¹⁸. On the basis of its GGQ peptidyl hydrolase domain, ICT1 is classified as a putative release factor, even though, like *yaeJ*, it lacks an anticodon recognizing domain. If ICT1 recycles stress-induced mitochondrial 50S•nc-tRNA complexes, this might explain its upregulation in neoplastic transformation, which is a process requiring the inhibition of apoptosis, for instance by the reduction of mitochondrial stress. Details will differ, as we did not find a eukaryotic homologue of Hsp15.

In this work, the SecM peptide was chosen for practical reasons – to stabilize the complexes by interaction of the nascent polypeptide with the ribosomal tunnel. This is a very unique peptide that causes translational arrest, prompting the question whether it is valid to extrapolate the results to

the general case. However, the presence of the SecM peptide is necessary, though not sufficient, for ribosome stalling: puromycin can still efficiently attack a tRNA carrying the SecM peptide^{7;19}, indicating P-site location of the tRNA moiety in the 70S complex and a functional peptidyl transfer centre. Full stalling by the SecM peptide additionally requires the presence of Pro-tRNA^{Pro} at the A site¹⁹. In the stalled 50S subunit, this second condition cannot be met for obvious reasons, so the SecM-stalled nc-tRNA•50S complex most likely does represent the general case of a heat-shocked 50S-peptidyl tRNA complex. In addition, the finding that Hsp15 only has specificity for 50S ribosomal subunits with a tRNA, regardless of the sequence of the nascent chain⁶, further supports the general relevance of our finding. In conclusion, we propose that Hsp15 rescues heat-induced abortive 50S•nc-tRNA subunits by fixing the tRNA moiety to the P-site, regardless of the nature of the nascent chain (Figure 4). This allows a (specialized) release factor to bind at the A-site and cleave the aminoacyl ester bond between tRNA and nascent chain. The cleavage allows tRNA and nascent chain to diffuse away and the 50S particle to become translationally active again.

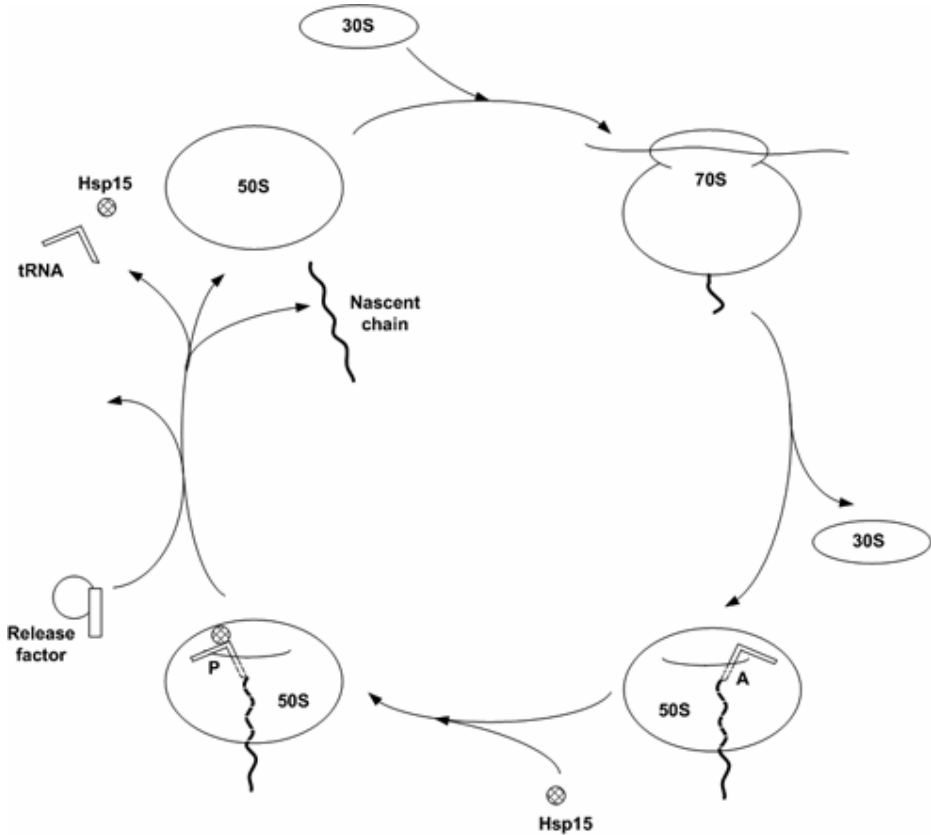


Figure 4 Rescue cycle of the stalled ribosomal 50S subunit. Heat shock can erroneously dissociate a translating ribosome into a 30S subunit and a blocked 50S subunit carrying a tRNA linked to the unfinished nascent chain (*upper right*). Here we show that in these stalled 50S•nc-tRNA complexes, the tRNA is located at the A-site (*bottom right*) and that the small heat shock protein Hsp15 translocates the tRNA to the P-site (*bottom left*), where it can be liberated by a release factor (*top left*).

References

1. Korber, P., Zander, T., Herschlag, D., & Bardwell, J.C. (1999). A new heat shock protein that binds nucleic acids. *J. Biol. Chem.* **274**, 249-256.
2. Richmond, C.S., Glasner, J.D., Mau, R., Jin, H., & Blattner, F.R. (1999). Genome-wide expression profiling in *Escherichia coli* K-12. *Nucleic Acids Res.* **27**, 3821-3835.
3. Klaholz, B.P., Pape, T., Zavialov, A.V., Myasnikov, A.G., Orlova, E.V., Vestergaard, B., Ehrenberg, M., & van Heel, M. (2003). Structure of the *Escherichia coli* ribosomal termination complex with release factor 2. *Nature* **421**, 90-94.
4. Petry, S., Brodersen, D.E., Murphy, F.V., Dunham, C.M., Selmer, M., Tarry, M.J., Kelley, A.C., & Ramakrishnan, V. (2005). Crystal structures of the ribosome in complex with release factors RF1 and RF2 bound to a cognate stop codon. *Cell* **123**, 1255-1266.
5. Rawat, U.B., Zavialov, A.V., Sengupta, J., Valle, M., Grassucci, R.A., Linde, J., Vestergaard, B., Ehrenberg, M., & Frank, J. (2003). A cryo-electron microscopic study of ribosome-bound termination factor RF2. *Nature* **421**, 87-90.
6. Korber, P., Stahl, J.M., Nierhaus, K.H., & Bardwell, J.C. (2000). Hsp15: a ribosome-associated heat shock protein. *EMBO J.* **19**, 741-748.
7. Schaffitzel, C. & Ban, N. (2007). Reprint of "Generation of ribosome nascent chain complexes for structural and functional studies" [*J. Struct. Biol.* 158 (2007) 463-471]. *J. Struct. Biol.* **159**, 302-310.
8. Jiang, L., Schaffitzel, C., Bingel-Erlenmeyer, R., Ban, N., Korber, P., Koning, R.I., de Geus, D.C., Plaisier, J.R., & Abrahams, J.P. (2008). Recycling of Aborted Ribosomal 50S Subunit-Nascent Chain-tRNA Complexes by the Heat Shock Protein Hsp15. *J. Mol. Biol.*
9. Kirchdoerfer, R.N., Huang, J.J., Isola, M.K., & Cavagnero, S. (2007). Fluorescence-based analysis of aminoacyl- and peptidyl-tRNA by low-pH sodium dodecyl sulfate-polyacrylamide gel electrophoresis. *Anal. Biochem.* **364**, 92-94.
10. Nakatogawa, H. & Ito, K. (2002). The ribosomal exit tunnel functions as a discriminating gate. *Cell* **108**, 629-636.
11. Plaisier, J.R., Jiang, L., & Abrahams, J.P. (2007). Cyclops: new modular software suite for cryo-EM. *J. Struct. Biol.* **157**, 19-27.

Chapter 2

12. Wohlgemuth, I., Beringer, M., & Rodnina, M.V. (2006). Rapid peptide bond formation on isolated 50S ribosomal subunits. *EMBO Rep.* **7**, 699-703.
13. Noller, H.F., Hoang, L., & Fredrick, K. (2005). The 30S ribosomal P site: a function of 16S rRNA. *FEBS Lett.* **579**, 855-858.
14. Stark, H., Orlova, E.V., Rinke-Appel, J., Junke, N., Mueller, F., Rodnina, M., Wintermeyer, W., Brimacombe, R., & van Heel, M. (1997). Arrangement of tRNAs in pre- and posttranslocational ribosomes revealed by electron cryomicroscopy. *Cell* **88**, 19-28.
15. Baranov, P.V., Vestergaard, B., Hamelryck, T., Gesteland, R.F., Nyborg, J., & Atkins, J.F. (2006). Diverse bacterial genomes encode an operon of two genes, one of which is an unusual class-I release factor that potentially recognizes atypical mRNA signals other than normal stop codons. *Biol. Direct.* **1**, 28.
16. Connolly, L., De Las, P.A., Alba, B.M., & Gross, C.A. (1997). The response to extracytoplasmic stress in *Escherichia coli* is controlled by partially overlapping pathways. *Genes Dev.* **11**, 2012-2021.
17. van Belzen, N., Dinjens, W.N., Eussen, B.H., & Bosman, F.T. (1998). Expression of differentiation-related genes in colorectal cancer: possible implications for prognosis. *Histol. Histopathol.* **13**, 1233-1242.
18. Emanuelsson, O., Nielsen, H., Brunak, S., & von Heijne, G. (2000). Predicting subcellular localization of proteins based on their N-terminal amino acid sequence. *J. Mol. Biol.* **300**, 1005-1016.
19. Muto, H., Nakatogawa, H., & Ito, K. (2006). Genetically encoded but nonpolypeptide prolyl-tRNA functions in the A site for SecM-mediated ribosomal stall. *Mol. Cell* **22**, 545-552.

Chapter

3

Characterization of a diagnostic Fab fragment binding trimeric Lewis X.

Daniël C. de Geus, Anne-Marie M. van Roon, Ellen A.J. Thomassen, Cornelis H. Hokke, André M. Deelder and Jan Pieter Abrahams

Proteins: Structure, Function, and Bioinformatics (2009) (in press)

Abstract

Lewis X trisaccharides normally function as essential cell-cell interaction mediators. However, oligomers of Lewis X trisaccharides expressed by the parasite *Schistosoma mansoni* seem to be related to its evasion of the immune response of its human host. Here we show that monoclonal antibody 54-5C10-A, which is used to diagnose schistosomiasis in humans, interacts with oligomers of at least three Lewis X trisaccharides, but not with monomeric Lewis X. We describe the sequence and the 2.5 Å crystal structure of its Fab fragment and infer a possible mode of binding of the polymeric Lewis X from docking studies. Our studies indicate a radically different mode of binding compared to Fab 291-2G3-A, which is specific for monomeric Lewis X, thus providing a structural explanation of the diagnostic success of 54-5C10-A.

3.1 Introduction

Individuals suffering from schistosomiasis raise an immune response against a variety of schistosomal carbohydrate elements including Galbeta1-4(Fucalpha1-3)GlcNAcbeta (Lewis X, LeX), a trisaccharide that is expressed both in monomeric and polymeric form in different life stages of the schistosomes.¹ Schistosomiasis (originally named bilharzia) is the main human parasitic disease after malaria in tropical and subtropical areas. Infection occurs when cercariae, free-swimming larval forms of schistosomes or blood flukes, enter the human host through the skin during contact with infected surface water. After penetrating the body the cercariae lose their typical forked tail and transform into schistosomula. This altered form of the parasite migrates *via* dermal veins to its final destination within the host's blood circulation where it develops into male and female adult worms. Schistosomes have an average life span of 3-5 years (and may survive up to 30 years) in the hostile environment of their definitive host. Thus, this parasite must have developed remarkable mechanisms to escape the immune response of its host. It is thought that the glycoconjugates, which are abundantly expressed throughout all life stages of the parasite play an important role in many of these escape mechanisms. Parasite glycans were found to induce immunomodulatory effects, for instance by down-regulating the host-protective TH-1 type immune response or the induction of anti-inflammatory responses². Lewis X both in monomeric and oligomeric form is one of the glycoconjugates, which is abundantly expressed throughout the different life stages of the parasite.³ Individuals

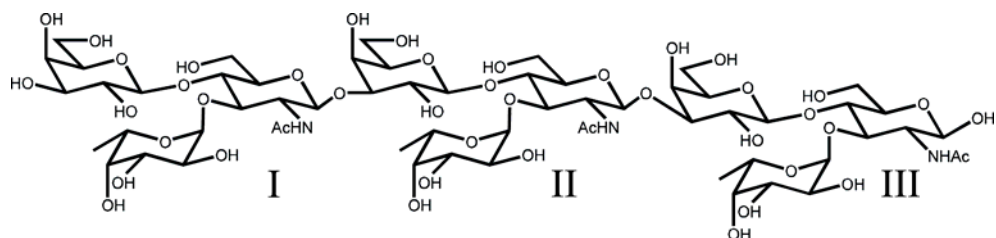


Figure 1 The antigen recognized by Fab 54-5C10-A is trimeric Lewis X. The repeating Lewis X units of the trimeric entity are labeled with Roman numerals.

with a schistosomal infection mount an immune response against the different oligomeric forms of Lewis X.⁴⁻⁸ One of the antigens regularly released from the gut of adult worms, the circulating cathodic antigen (CCA), contains different oligomeric presentations of the carbohydrate Lewis X. Most of these presentations contain trimeric Lewis X (Figure 1) as part of a longer carbohydrate chain. CCA is excreted in such high amounts that sensitive assays to diagnose schistosomiasis are based on its detection in an ELISA using anti-Lewis X monoclonal antibodies. Recently a reagent strip assay was developed containing anti-CCA Mab 54-5C10-A in its capture matrix providing a simple and rapid alternative to the ELISA which can be used in endemic areas. The activity and intensity of a schistosomal infection can easily be measured by using this reagent strip based on the detection of CCA in urine of patients.⁹

International efforts to generate anti-schistosome vaccines are part of schistosomiasis control programs.¹⁰ Despite one potential candidate antigen (Sh28 GST) proceeding as far as Phase I and II clinical trials currently no effective vaccine against the disease exists.¹¹ Although (medical) treatment

with praziquantel cures up to 96% of the patients, reinfection easily takes place in most of the endemic areas.¹¹⁻¹⁴ A simple and rapid specific assay is therefore required both for initial diagnosis and for the follow-up of chemotherapy.

In this chapter, as a contribution towards the immunology of schistosomiasis, we report an analysis of the characteristics of the diagnostically important antibody fragment 54-5C10-A. We show that it exclusively binds oligomeric Lewis X and not monomeric Lewis X. The crystal structure to 2.5 Å demonstrates a binding groove which is able to accommodate a trimeric Lewis X molecule. The structure of this trimeric LeX binding Fab is compared to the monomeric Lewis X binding Fab 291-2G3-A.¹⁵

3.2 Experimental procedures

3.2.1 Purification of Fab 54-5C10-A

The murine Fab 54-5C10-A (IgG3κ isotype) was obtained from hybridoma cell culture supernatant using standard biochemical methods as described before.¹⁶ During the purification, isoelectric focusing gel electrophoresis showed different isoforms of Fab 54-5C10-A with pI values of 9.3, 7.7 and 7. This mixture was dialyzed against 20 mM Tris-HCl pH 8 containing 0.02% (w/v) NaN₃ and loaded on an anion exchange column (UNO Q-1, Biorad). After elution with a 0-1 M NaCl gradient the flowthrough containing the two isoforms with the highest pI values was dialyzed against

20 mM glycine buffer pH 9. However, these isoforms could not be separated by ion exchange chromatography, so the sample was concentrated to 15 mg mL⁻¹ using an Ultrafree Centrifugal Filter Unit (Millipore) and used for crystallization.

3.2.2 Immunofluorescence assay

The immunofluorescence assay (IFA) was carried out on 6 µm thick sections of *S. mansoni* adult worms in frozen infected hamster liver tissue. Slides were incubated with Mab 54-5C10-A (25 µg/ml) in phosphate-buffered saline (PBS; 0.035 M phosphate, 0.15 M NaCl, pH 7.8), washed, and incubated with fluorescein isothiocyanate (FITC) labeled goat anti-mouse immunoglobulin according to manufacturer's instructions (Nordic, Tilburg, the Netherlands). Images were recorded using a Leica HC microscope equipped with a Leica DRC 350FX camera, using the appropriate filter combination for FITC fluorescence.

3.2.3 Surface plasmon resonance analysis of 54-5C10-A binding Lewis X-type neoglycoconjugates

Human serum albumin (HSA) neoglycoconjugates containing LNFPIII, di- or trimeric LeX were purchased from Isosep AB (Tullinge, Sweden) and contained on average 22 mol sugar per mol HSA. LNFPIII or lacto-N-fucopentaose III (Galβ1-4(Fuca1-3)GlcNAcβ1-3Galβ1-4Glcβ) is a pentasaccharide containing Lewis X at its non-reducing end. The BIAcore 3000 instrument, CM5 sensor chips and an amino coupling kit were

purchased from BIAcore AB (Uppsala, Sweden). The Lewis X neoglycoconjugates were immobilized on a CM5 sensor chip to a level of 7,500 RU using the procedures described before.¹⁵ Unmodified HSA was coupled on one flow channel of each sensor chip as a control. Five μL of purified 54-5C10-A (1 mg mL^{-1} in 0.035 M phosphate-buffered saline, PBS) was injected. All analyses were performed, corrected and evaluated as previously.¹⁵

3.2.4 Sequencing of the variable domains

Standard molecular biology protocols were used to synthesize and amplify cDNA of the IgG variable regions from total hybridoma mRNA.¹⁵ The resulting DNA fragments were cloned in the pSTBlue-1 cloning vector according to the protocol of the Perfectly Blunt Cloning Kit (Novagen) and transformed into NovaBlue Singles Competent cells. Transformants were selected for the kanamycin resistance marker of the cloning vector and for the vector carrying an insert with X-Gal (5-bromo-4-chloro-3-indolyl- β -galactopyranoside). Sequences were obtained commercially (Base Clear, Leiden, the Netherlands) by automated dideoxy chain-termination technology using the T7 and SP6 promoter primers.

3.2.5 Crystallization and data collection

Prior to crystallization, the protein sample was filtered through a low binding protein 0.22 μm filter (Millipore) to remove dust particles and protein precipitate. Crystallization trials were performed using the sitting

drop vapour-diffusion technique at 295 K using equal volumes of protein and reservoir solution.

Data collection at cryogenic temperatures utilized crystals soaked in a solution containing 0.1 M sodium citrate pH 4, 11% polyethylene glycol 3350 and 22.5% glycerol, flash-frozen in a stream of nitrogen gas at 100 K using an Oxford Cryosystems Cryostream device. Data were collected by the rotation method for 180 frames with 1.0° rotation and 25 seconds exposure time per frame, using a MAR Research 165 mm CCD detector on beamline BM14 at the European Synchrotron Radiation Facility (ESRF), Grenoble, France. The intensities were indexed using MOSFLM¹⁷ and scaled using SCALA¹⁸.

3.2.6 Structure determination

The structure of Fab 54-5C10-A was solved by molecular replacement with MOLREP¹⁹ from the CCP4 program suite^{19;20} using the (uncomplexed) structure of the anti-monomeric Lewis X Fab fragment (PDB code 1UZ6) as a search model. The molecular-replacement solution was improved by rigid-body refinement and restrained refinement with REFMAC5²¹. Rebuilding was done with ARP/wARP²² and Coot²³ and the refinement continued using TLS (translation, libration and screw) parameters²⁴. The quality of the final model with $R_f = 0.20$ and $R_{free} = 0.26$, was checked using PROCHECK²⁵ and WHATIF²⁶. Illustrations were prepared using Pymol (Figures 4 and 5; <http://pymol.sourceforge.net/>) and Accelrys DS Visualizer (Figure 7; <http://www.accelrys.com/>).

3.2.7 Docking trimeric Lewis X into the binding groove

Currently no crystal structure is available for the trimeric Lewis X antigen (Figure 1), hence a 3D model for this saccharide was generated using the program Sweet2²⁷. The potential binding sites on the solvent accessible surface of one Fab 54 molecule (chain A and B) were determined with the grid-based cavity prediction implemented in the Molegro Virtual Docker (MVD) software (Molegro ApS, Aarhus, Denmark). The cavity corresponding to the antigen binding site was selected as the search space origin employing a 25 Å radius. Subsequently, the flexible ligand docking protocol of the MVD software was used and the resulting poses were imported back to MVD for visual inspection. The best pose, having the lowest scoring energy (the sum of the ligand-protein interaction energy and the internal ligand energy), was further analyzed.

3.3 Results and discussion

3.3.1 Screening antibodies for their meric Lewis X specificity

Previously, a large set of anti-schistosome monoclonal antibodies has been produced²⁸ and screened by SPR for their interaction with HSA Lewis X neoglycoconjugates²⁹. Depending on their interaction behaviour Mabs were split up in three groups. Group I binds mono-, di- and trimeric Lewis X oligomers, group II interacts with both di- and trimeric Lewis X and group III has specific affinity for trimeric Lewis X. The sensorgrams of Mab 291-2G3-A (representing group I) and Mab 54-5C10-A (group III) shown in

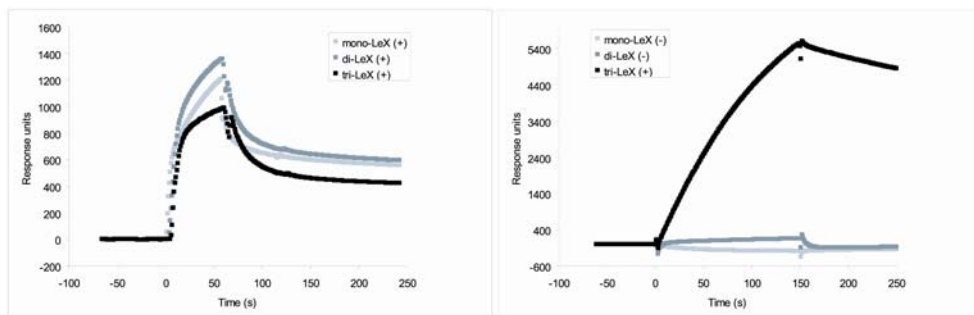


Figure 2 SPR sensorgrams of Mab 291-2G3-A (*left*) and Mab 54-5C10-A (*right*) with mono-, di- and trimeric Lewis X HSA-glycoconjugates. The interaction of the antibody was interpreted as binding (+) or non-binding (-).

Figure 2 indicate that mono-, di- and trimeric Lewis X are immunologically discernible entities.

The natural epitope of Mab 54-5C10-A on adult worms *S. mansoni* worms is shown by immunofluorescence (Figure 3). Sections of schistosomes

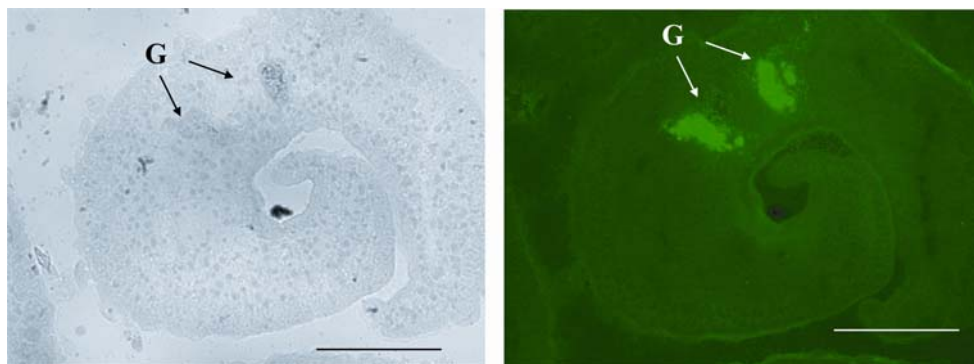


Figure 3 IFA: normal light (*left*) and immunofluorescence (*right*) microscopy image of a section of an adult *S. mansoni* worm incubated with Mab 54-5C10-A specific for the circulating cathodic antigen (CCA). Fluorescence is specifically observed in the gut (G) of the worm. Bar = ~ 100 μ m.

Table I Data-processing statistics for the Fab 54-5C10-A crystal

X-ray source	ESRF BM 14
Wavelength (Å)	0.95372
Resolution range (Å)	28.7-2.5 (2.64-2.5) ^a
Crystal system	monoclinic
Spacegroup	P2 ₁
Unit cell parameters (Å, °)	$a = 51.4, b = 161.0, c = 53.5$ $\beta = 103.1$
Observed reflections	109380 (15957)
Unique reflections	29262 (4281)
Redundancy	3.7 (3.7)
Completeness (%)	99.9 (100.0)
Average I/σ(I)	10.6 (3.2)
R_{merge}^b (%)	5.5 (23.5)
Solvent content (%)	42.7
V_M (Å ³ /Da) ^c	2.2

^a Data of the outer resolution shell are given in parentheses

^b $R_{\text{merge}} = \sum |I - \langle I \rangle| / \sum I$, where I is the integrated intensity of an observed reflection and $\langle I \rangle$ is the average intensity over symmetry-equivalent measurements

^c Matthews coefficient³⁰

incubated with Mab 54-5C10-A and subsequently with FITC-labeled secondary antibody showed distinct fluorescent patterns in the gut of the worm.

3.3.2 Crystals and structure of the Fab fragment

Rectangular plate-shaped crystals of maximum dimensions 1.3 x 0.1 x 0.1 mm³ were grown from 0.1 M sodium citrate pH 4, 11% polyethylene glycol

3350. A single crystal was used for the data collection with data-processing statistics as shown in Table 1. Analysis of the X-ray diffraction pattern indicated that along the k axis reflections were only present if $k = 2n$, identifying the space group as $P2_1$.

The Fab 54-5C10-A structure (later referred to as Fab 54) was determined to 2.5 Å resolution. The statistics of the final model (Figure 4) are shown in Table 2. The framework region of the Fab 54 shows the usual immunoglobulin fold with elbow angles between the VL:VH and CL:CH1 pseudo-twofold axes of 134.6° (chain A,B) and 133.1° (chain E,F). Small elbow angles like these are the most preferred among κ chain type Fabs.³¹

3.3.2.1 Model quality of the native Fab 54 crystal structure

In the final model of Fab 54 with $R_f = 0.20$ and $R_{free} = 0.26$ the amino acid residues 126 to 132 of the heavy chain F (and 127 to 131 of heavy chain B) are missing. This region is located in a flexible loop with higher than average sequence variability according to the variability index for constant domain sequences and is often disordered in Fab crystal structures.³² Extra density in the vicinity of the protein chain in the model was interpreted as glycine, azide and glycerol molecules (used in the crystallization and cryoprotection). The structure of Fab 54 has 89 % of all residues in the most favoured region, having less than 1 % in the disallowed area of the Ramachandran plot. In both light chains the residue Val L51 (Kabat

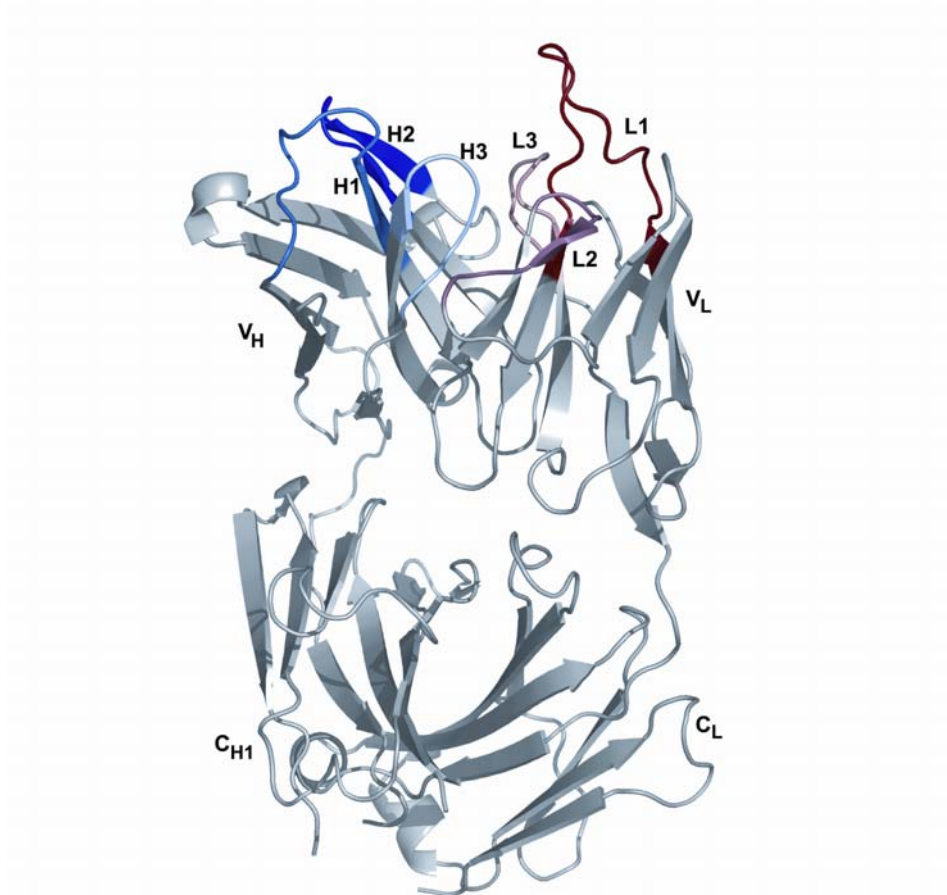


Figure 4 Ribbon representation of the Fab fragment 54-5C10-A. Complementarity determining regions of the light and heavy chain are depicted as CDR-L1 (red), L2 (raspberry), L3 (salmon) CDR-H1 (darkblue), H2 (blue) and H3 (lightblue).

numbering), which lies in a turn located between two β -strands at the beginning of CDR-L2, is a Ramachandran outlier. This is commonly observed in other Fabs.³³

Table II Refinement statistics for the Fab 54-5C10-A crystal

Refinement	Fab 54-5C10-A
Resolution range (Å)	25.0-2.5
R-factor	0.203 (0.260)
Number of Fab molecules in the AU	2
Number of TLS groups	28
Protein residues	848
Water molecules	214
Ligands	8 glycines/ 3 glycerols /1 azide
Rms deviations bonds (Å)	0.020
Rms deviations angles (°)	1.668
Average B value (Å ²)	
protein/ solvent	43.0/38.9
glycerol/glycine/azide	51.6/47.0/46.1
Ramachandran statistics overall (%)	88.8/8.3/2.0/0.8 ^b
A, B chain	89.6/8.7/1.1/0.5
E, F chain	88.0/8.2/2.7/1.1

^a Data statistics of R_{free} are given in parentheses

^b Order: most favoured, additionally allowed, generously allowed and disallowed regions. The Ramachandran plot was generated with PROCHECK³⁴

3.3.2.2 Analysis of the Fab 54 hypervariable loops: sequence and structure

The Fab 54 structure showed a rather long and narrow cleft separating the hypervariable parts of the heavy and light chain (Figure 5a and 5b). The dimensions of this binding channel are approximately 11 Å wide, 7 Å deep and 24 Å long (measured in Coot³⁵) contrasting with the relatively small

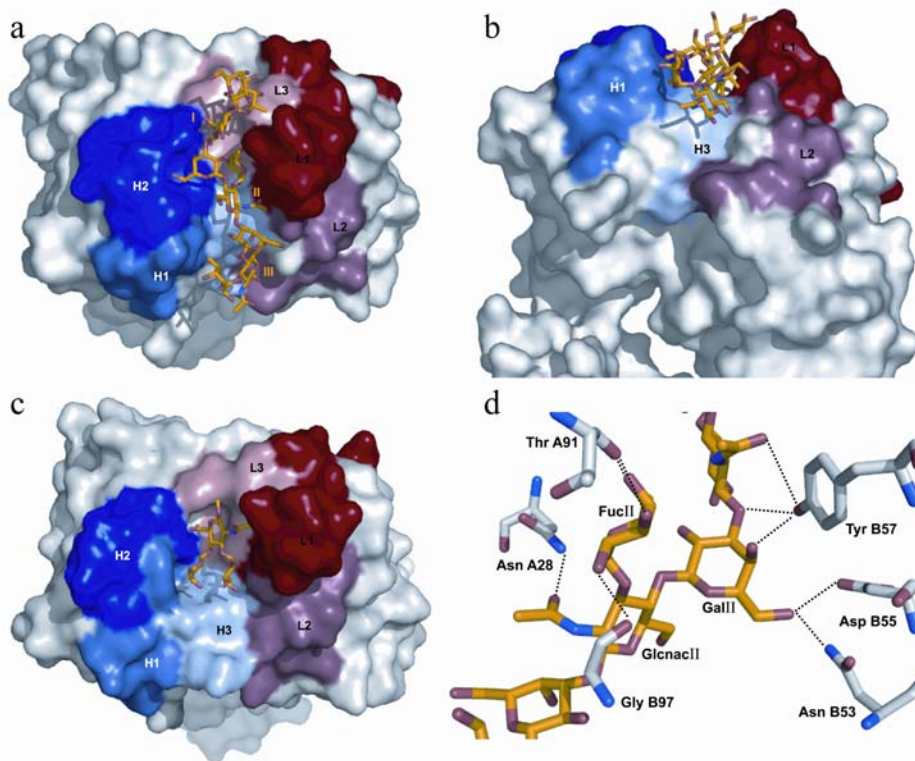


Figure 5 Comparison of two Lewis X binding sites. The complementarity determining regions of the light and heavy chain are depicted as in Figure 4. (a,b) Crystal structure of the light and heavy chain from Fab 54-5C10-A with trimeric Lewis X (yellow) docked into the antigen binding site. The repeating Lewis X units of the trimeric entity are labeled with Roman numerals as in Figure 1 and Table III (c) Crystal structure of the light and heavy chain from Fab 291-2G3-A in complex with monomeric Lewis X. (d) Close view of the docked trimeric Lewis X showing the intermolecular hydrogen bonding interactions. For reasons of clarity, only the central part of the carbohydrate chain is depicted.

binding pocket of Fab 291 (Figure 5c). The latter accommodates the Lewis X trisaccharide in a pocket 13 Å wide, 10 Å deep and 15 Å long.¹⁵

It is known that hydrogen bonds and van der Waals contacts are the most important factors in stabilizing protein-carbohydrate complexes³⁶ and sugar binding sites are therefore usually populated by planar polar side chains partaking in hydrogen bond networks. Aromatic side chains can form additional hydrogen bonds with sugar residues (see Tyr B57 in Figure 5d) and are able to stack with the hydrophobic face of the sugar ring. Indeed almost half of the binding site residues in Fab 54 have polar or aromatic side chains, but this fraction is identical in the case of Fab 291 (Figure 6) which binds a monomer of Lewis X only.

Analysis of the six CDRs in the Fab 54 sequence classified CDR-L1, L2 and L3 to the same structural clusters as the corresponding regions in Fab 291 (4/16A, 1/7A and 1/9A, respectively), but the heavy chain CDRs belong to different classes for the two Fabs. CDR-H1 of Fab 54 is a class 3/12A and CDR-H2 a 1/9A loop (1/10A and 3/10B in Fab 291, respectively). Among the six CDRs, the H3 segment has a distinctive role in antigen recognition and the largest diversity in length, sequence and structure.³⁷⁻³⁹ Based on the 'H3-rules' describing the relationship between the sequence and the CDR-H3 conformation derived from crystal structures, the H3 loop of Fab 54 is predicted to be a kinked base.³⁹ Indeed the side chain of Asp H101 forms a salt bridge with Arg H94 at the start of CDR-H3. Fab 291 should also form the kinked base according to the 'H3-rules', but the protein model shows an extended structure, probably caused by the presence of the charge and size of Arg H99 and Phe H100.

3.3.2.3 Modeling trimeric Lewis X into the binding groove

We were not able to grow crystals containing the trimeric Lewis X antigen, neither using co-crystallization nor soaking. We decided to use docking as an alternative way to study and predict the Fab 54 interaction with trimeric Lewis X. The molecule in the asymmetric unit showing the best Ramachandran statistics (chain A and B) was selected and the flexible ligand docking protocol of Molegro Virtual Docker resulted in the optimal fit of the carbohydrate into the antigen binding site as shown in Figure 5a, 5b and 5d. All three Lewis X moieties are in contact with the antibody paratope, while the middle one seems to anchor with the most and tightest hydrogen bonds (Table 3 and Figure 5d). Binding of the trimeric Lewis X buries 822 Å² of the 19170 Å² solvent accessible surface of one Fab molecule, whereas the monomeric Lewis X in the crystal structure of 291-2G3-A buries 302 Å² upon binding. In both cases residues of all CDRs are involved in hydrogen bonds bridging the antigen. One striking feature of the Fab 54 binding groove is that it is dominated by aromatic residues like the binding pocket in Fab 291, but more extended over the entire binding surface. Aromatic stacking is observed for the Fab 54 amino acids residues Phe A32, which interacts with FucII, and Trp B52 with GalII.

Burial of nonpolar groups at the interface also contributes to the trimeric Lewis X binding affinity. The methyl group of the GlcNAcI acetyl function is stabilized by the side chains of Val A94 and Tyr B57, while the FucI methyl makes a van der Waals interaction with the Ser A27E OG atom. The Fab 291 light chain residue Tyr 27d, forming several hydrogen bonds and a

Table III Hydrogen bonds between trimeric Lewis X and the CDRs of Fab 54 (Kabat numbering)

CDR	Fab 54-5C10-A residue	Atom	Distance (Å)	Sugar residue ^a	Atom
L1	Asn A28	ND2	3.2	GlcnaclI	O7
L2	Lys A50	NZ	3.2	GalIII	O6
L3	Thr A91	O	2.7	FucII	O3
L3	Thr A91	O	2.7	FucII	O4
L3	His A93	ND1	2.9	FucI	O4
H1	Ser B32	O	3.2	FucIII	O4
H2	Asn B53	ND2	3.2	GalII	O6
H2	Asp B55	OD2	3.1	GalII	O6
H2	Tyr B57	OH	3.2	GlcnaclI	O1
H2	Tyr B57	OH	2.6	GalII	O4
H3	Gly B97	O	2.6	FucII	O2

^a Numbering of the sugar residues is according to the Lewis X units (indicated with Roman numerals in Figure 1 and 5a)

van der Waals interaction with its monomeric antigen, has been replaced by His A27d in Fab 54 to make several van der Waals interactions with the FucII methyl group. Furthermore, Ser B32 and Gly B33 in Fab 54 are substitutes for the bulkier heavy chain residues Tyr 32 and Trp 33 of Fab 291. The Ser and Gly side chains create, in concert with Met B34, an intermediate hydrophobic surface stabilizing the methyl of FucIII. The overall hydrophobic character of the binding groove with a few flanking charges involved in hydrogen bonding, is shown in Figure 7.

The structure of the Lewis X trisaccharide is relatively rigid in solution, corresponding closely to the conformation found in the crystal structure. In

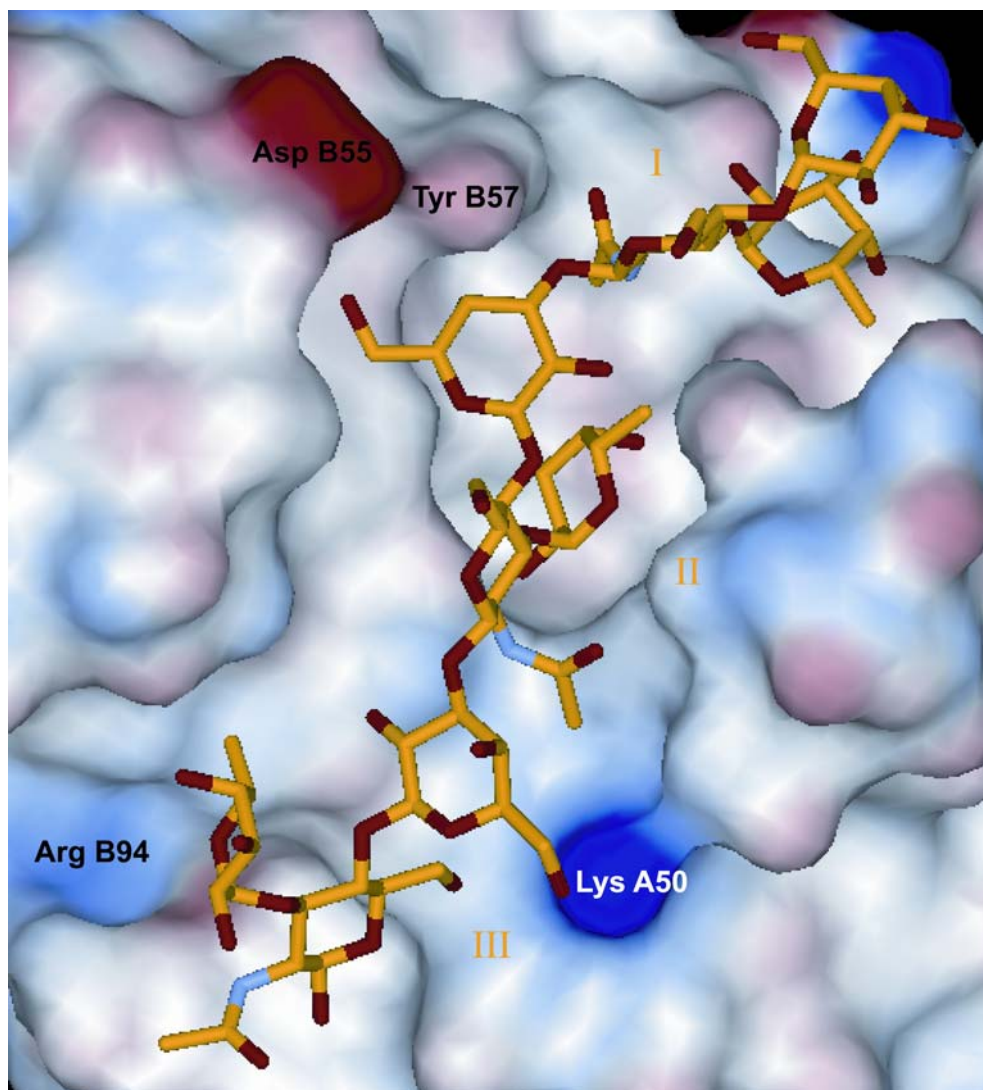


Figure 7 Molecular surface (colored according to electrostatic potential) for the Fab 54 binding site. Proximal residues with the largest charge are labelled.

general, the monomer is stabilized by stacking of the hydrophobic face of the fucose with the galactose ring. The structure of trimeric Lewis X is unknown and therefore the docked model has been analyzed by evaluating the torsion angles at the glycosidic linkages (see Table IV). The torsion angles were compared to those present in carbohydrate structures in the Protein Data Bank using GlyTorsion.⁴¹ All torsion angles of the trimeric Lewis X model are in the range of most commonly observed angles for the Fuc α (1-3)Glcnac linkage (of 214 torsions analysed), while the only outlier for the Gal β (1-4)Glcnac bond (of 120 torsions analysed) is Ψ 1 of the third Lewis X unit. While the Lewis X units I and II resemble the monomeric Lewis X conformation in terms of torsion angles and hydrophobic stacking of the fucose with the galactose ring, the third Lewis X differs the most. Possibly the absence of hydrophobic stacking in this third unit is compensated by hydrogen bonds between GalIII and Lys A50 from the CDR-L2 and between FucIII and Ser B32 from CDR-H1.

The recognition site for the second Lewis X unit (Figure 5a) is comparable in appearance to the monomeric binding pocket (Figure 5c). Despite this similarity, the mode of binding of the target is different. Lewis X unit II in Fab 54 is rotated approximately 180° in the binding groove compared to the monomeric Lewis X in Fab 291. The resulting orientation of Lewis X unit II is very similar to the binding mode of the Lewis X moiety in the crystal structure of the Fab BR96-nLewis Y complex. BR96 is a tumour selective antibody binding the nonoate methyl ester derivative of Lewis Y, a tetrasaccharide containing Lewis X.⁴² The presence of at least three Lewis X units is essential for binding Fab 54 (Figure 2). The absence

Table IV Comparison of the torsion angles^a at the glycosidic linkages in Lewis X

Linkage	Torsion angle of trimeric Lewis X unit		
	I	II	III
Gal β (1-4)Glcnac (Φ 1/ Ψ 1)	-67.1/-118.4	-49.8/-72.8	-65.6/-58.8
Fuc α (1-3)Glcnac (Φ 2/ Ψ 2)	-59.1/155.2	-72.6/134.7	-58.6/149
	Torsion angle of monomeric Lewis X in		
	crystal ^b	cocrystal ^c	solution ^d
Gal β (1-4)Glcnac (Φ 1/ Ψ 1)	-70.5/-107.7	-66.7/-114.4	-75/-104
Fuc α (1-3)Glcnac (Φ 2/ Ψ 2)	-76.7/139	-82.7/136.7	-81/151

^a Torsion angles are defined as Φ 1 = O5gal-C1gal-O4glcnac-C4glcnac, Ψ 1 = C1gal-O4glcnac-C4glcnac-C5glcnac, Φ 2 = O5fuc-C1fuc-O3glcnac-C3glcnac and Ψ 2 = C1fuc-O3glcnac-C3glcnac-C4glcnac.

^b Values for one of the two molecules present in the asymmetric unit⁴³

^c Lewis X conformation as observed in one of the two Fab291-Lewis X complexes present in the asymmetric unit¹⁵

^d Calculated lowest energy conformation⁴⁴

of one or two Lewis X units would leave a considerable part of the binding pocket unoccupied. It has been demonstrated for the anti-tumour antibody BR96 that even the absence of one hexose unit of its tetrasaccharide antigen nLewis Y resulted in the disappearance of binding, while the concerning hexose unit is interacting solely with one His residue in the BR96-nLewis Y complex.⁴⁵

We anticipate that higher oligomeric forms than trimeric Lewis X might bind to Fab 54 as well. This requires a movement of CDR-H3 to convert the combining site from a 24 Å long channel into one sufficiently extended to accommodate additional Lewis X units. However, this is not unlikely to happen since structural changes of CDR-H3 side chains up to 15 Å movements are known.^{46;47}

3.4 Conclusions

To better understand molecular recognition of trimeric Lewis X, we have determined the sequence and the structure of the anti-CCA Fab 54. The SPR results from this study clearly demonstrate that the described Fab 54 needs at least three repeating units of the Lewis X trisaccharide to bind CCA. We have docked this trimeric Lewis X ligand into the groove type antigen binding site and conclude that all six CDRs contribute to binding. Together with the Fab 291-monomeric Lewis X structure, the current model provides a framework for understanding the specificity for the different Lewis X antigens involved in schistosomiasis. The crystal structures show a striking difference in the morphology of the antigen binding site: a long channel in Fab 54 in contrast to a rather shallow binding pocket in Fab 291. In addition, the crystal structure of this diagnostic Fab 54 fragment implies that a more extended, repeating epitope fits into its binding site. The current study has revealed the property of Fab 54 to recognize oligomers of at least three Lewis X units which enables the CCA detection from urine while excluding cross reactivity with shorter endogenous Lewis X fragments from the infected host.

Coordinates and sequences

Coordinates and structure factors have been deposited in the Protein Data Bank (accession code 2VQ1). The sequences of the variable domain of the heavy and light chain have been deposited in the EMBL/GenBank/DBJ database (AM944590 and AM944591, respectively).

Acknowledgements

We thank René van Zeyl for culturing hybridoma cells containing Mab 54-5C10-A and Hans de Vrind for his practical assistance with sequencing and purification. The European Synchrotron Radiation Facility (ESRF) staff at beamline BM14 is gratefully acknowledged for access to the synchrotron radiation source and assistance with station alignment.

References

1. Hokke, C.H., Deelder, A.M., Hoffmann, K.F., & Wuhler, M. (2007). Glycomics-driven discoveries in schistosome research. *Exp. Parasitol.* **117**, 275-283.
2. Thomas, P.G. & Harn, D.A., Jr. (2004). Immune biasing by helminth glycans. *Cell Microbiol.* **6**, 13-22.
3. Hokke, C.H. & Deelder, A.M. (2001). Schistosome glycoconjugates in host-parasite interplay. *Glycoconj. J.* **18**, 573-587.
4. Nyame, A.K., Pilcher, J.B., Tsang, V.C., & Cummings, R.D. (1996). Schistosoma mansoni infection in humans and primates induces cytolytic antibodies to surface Le(x) determinants on myeloid cells. *Exp. Parasitol.* **82**, 191-200.
5. Nyame, A.K., Pilcher, J.B., Tsang, V.C., & Cummings, R.D. (1997). Rodents infected with Schistosoma mansoni produce cytolytic IgG and IgM antibodies to the Lewis x antigen. *Glycobiology* **7**, 207-215.
6. Richter, D., Incani, R.N., & Harn, D.A. (1996). Lacto-N-fucopentaose III (Lewis x), a target of the antibody response in mice vaccinated with irradiated cercariae of Schistosoma mansoni. *Infect. Immun.* **64**, 1826-1831.
7. van Remoortere, A., van Dam, G.J., Hokke, C.H., van den Eijnden, D.H., van Die, I., & Deelder, A.M. (2001). Profiles of immunoglobulin M (IgM) and IgG antibodies against defined carbohydrate epitopes in sera of Schistosoma-infected individuals determined by surface plasmon resonance. *Infect. Immun.* **69**, 2396-2401.
8. van Remoortere, A., Vermeer, H.J., van Roon, A.M., Langermans, J.A., Thomas, A.W., Wilson, R.A., van Die, I., van den Eijnden, D.H., Agoston, K., Kerekgyarto,

- J., Vliegenthart, J.F., Kamerling, J.P., van Dam, G.J., Hokke, C.H., & Deelder, A.M. (2003). Dominant antibody responses to Fucalpha1-3GalNAc and Fucalpha1-2Fucalpha1-3GlcNAc containing carbohydrate epitopes in Pan troglodytes vaccinated and infected with *Schistosoma mansoni*. *Exp. Parasitol.* **105**, 219-225.
9. van Dam, G.J., Wichers, J.H., Ferreira, T.M., Ghati, D., van Amerongen, A., & Deelder, A.M. (2004). Diagnosis of schistosomiasis by reagent strip test for detection of circulating cathodic antigen. *J. Clin. Microbiol.* **42**, 5458-5461.
 10. Hagan, P., Doenhoff, M.J., Wilson, R.A., Al Sherbiny, M., & Bergquist, R. (2000). Schistosomiasis vaccines: a response to a devils' advocate's view. *Parasitol. Today* **16**, 322-323.
 11. Lebens, M., Sun, J.B., Czerkinsky, C., & Holmgren, J. (2004). Current status and future prospects for a vaccine against schistosomiasis. *Expert. Rev. Vaccines.* **3**, 315-328.
 12. Grover, J.K., Vats, V., Uppal, G., & Yadav, S. (2001). Anthelmintics: a review. *Trop. Gastroenterol.* **22**, 180-189.
 13. Ross, A.G., Bartley, P.B., Sleight, A.C., Olds, G.R., Li, Y., Williams, G.M., & McManus, D.P. (2002). Schistosomiasis. *N. Engl. J. Med.* **346**, 1212-1220.
 14. Wu, G.Y. & Halim, M.H. (2000). Schistosomiasis: progress and problems. *World J. Gastroenterol.* **6**, 12-19.
 15. van Roon, A.M., Pannu, N.S., de Vrind, J.P., van der Marel, G.A., van Boom, J.H., Hokke, C.H., Deelder, A.M., & Abrahams, J.P. (2004). Structure of an anti-Lewis X Fab fragment in complex with its Lewis X antigen. *Structure.* **12**, 1227-1236.
 16. van Roon, A.M., Pannu, N.S., Hokke, C.H., Deelder, A.M., & Abrahams, J.P. (2003). Crystallization and preliminary X-ray analysis of an anti-LewisX Fab fragment with and without its LewisX antigen. *Acta Crystallogr. D. Biol. Crystallogr.* **59**, 1306-1309.
 17. Leslie, A.G. (1999). Integration of macromolecular diffraction data. *Acta Crystallogr. D. Biol. Crystallogr.* **55**, 1696-1702.
 18. Evans, P. (2006). Scaling and assessment of data quality. *Acta Crystallogr. D. Biol. Crystallogr.* **62**, 72-82.
 19. Vagin, A. A. and Teplyakov, A. (1997) MOLREP: an automated program for molecular replacement. *J. Appl. Crystallogr.* **30**, 1022-1025.

20. Collaborative Computational Project Number 4 (1994) The CCP4 suite: programs for protein crystallography. *Acta Crystallogr. D. Biol. Crystallogr.* **50**, 760-763.
21. Murshudov, G.N., Vagin, A.A., & Dodson, E.J. (1997). Refinement of macromolecular structures by the maximum-likelihood method. *Acta Crystallogr. D. Biol. Crystallogr.* **53**, 240-255.
22. Perrakis, A., Morris, R., & Lamzin, V.S. (1999). Automated protein model building combined with iterative structure refinement. *Nat. Struct. Biol.* **6**, 458-463.
23. Emsley, P. & Cowtan, K. (2004). Coot: model-building tools for molecular graphics. *Acta Crystallogr. D. Biol. Crystallogr.* **60**, 2126-2132.
24. Winn, M.D., Isupov, M.N., & Murshudov, G.N. (2001). Use of TLS parameters to model anisotropic displacements in macromolecular refinement. *Acta Crystallographica Section D-Biological Crystallography* **57**, 122-133.
25. Laskowski, R.A., MacArthur, M.W., Moss, D.S., & Thornton, J.M. (1993). PROCHECK: a program to check the stereochemical quality of protein structures. *J. Appl. Cryst.* **26**, 283-291.
26. Vriend, G. (1990). WHAT IF: a molecular modeling and drug design program. *J. Mol. Graph.* **8**, 52-56.
27. Lutteke, T., Bohne-Lang, A., Loss, A., Goetz, T., Frank, M., & der Lieth, C.W. (2006). GLYCOSCIENCES.de: an Internet portal to support glycomics and glycobiology research. *Glycobiology* **16**, 71R-81R.
28. Deelder, A.M., van Dam, G.J., Kornelis, D., Fillie, Y.E., & van Zeyl, R.J. (1996). Schistosoma: analysis of monoclonal antibodies reactive with the circulating antigens CAA and CCA. *Parasitology* **112**, 21-35.
29. van Roon, A. M. Thesis, Schistosoma mansoni: structural and biophysical aspects of Lewis X-antibody interactions. Leiden University, 2005.
30. Matthews, B.W. (1968). Solvent content of protein crystals. *J. Mol. Biol.* **33**, 491-7.
31. Stanfield, R.L., Zemla, A., Wilson, I.A., & Rupp, B. (2006). Antibody elbow angles are influenced by their light chain class. *J. Mol. Biol.* **357**, 1566-1574.
32. Stanfield, R.L., Fieser, T.M., Lerner, R.A., & Wilson, I.A. (1990). Crystal structures of an antibody to a peptide and its complex with peptide antigen at 2.8 Å. *Science* **248**, 712-719.

33. Barbas, C.F., III, Heine, A., Zhong, G., Hoffmann, T., Gramatikova, S., Bjornestedt, R., List, B., Anderson, J., Stura, E.A., Wilson, I.A., & Lerner, R.A. (1997). Immune versus natural selection: antibody aldolases with enzymic rates but broader scope. *Science* **278**, 2085-2092.
34. Laskowski, R. A. (1993) PROCHECK; a program to check the stereochemical quality of protein structures. *J. Appl. Crystallogr.* **26**, 283-291.
35. Emsley, P. & Cowtan, K. (2004). Coot: model-building tools for molecular graphics. *Acta Crystallogr. D. Biol. Crystallogr.* **60**, 2126-2132.
36. Quioco, F.A. (1986). Carbohydrate-binding proteins: tertiary structures and protein-sugar interactions. *Annu. Rev. Biochem.* **55**, 287-315.
37. Al Lazikani, B., Lesk, A.M., & Chothia, C. (1997). Standard conformations for the canonical structures of immunoglobulins. *J. Mol. Biol.* **273**, 927-948.
38. Chothia, C., Lesk, A.M., Tramontano, A., Levitt, M., Smith-Gill, S.J., Air, G., Sheriff, S., Padlan, E.A., Davies, D., & Tulip, W.R. (1989). Conformations of immunoglobulin hypervariable regions. *Nature* **342**, 877-883.
39. Shirai, H., Kidera, A., & Nakamura, H. (1999). H3-rules: identification of CDR-H3 structures in antibodies. *FEBS Lett.* **455**, 188-197.
40. Martin, A.C. (1996). Accessing the Kabat antibody sequence database by computer. *Proteins* **25**, 130-133.
41. Lutteke, T., Frank, M., & der Lieth, C.W. (2005). Carbohydrate Structure Suite (CSS): analysis of carbohydrate 3D structures derived from the PDB. *Nucleic Acids Res.* **33**, D242-D246.
42. Jeffrey, P.D., Bajorath, J., Chang, C.Y., Yelton, D., Hellstrom, I., Hellstrom, K.E., & Sheriff, S. (1995). The x-ray structure of an anti-tumour antibody in complex with antigen. *Nat. Struct. Biol.* **2**, 466-471.
43. Perez, S., Mouhous-Riou, N., Nifant'ev, N.E., Tsvetkov, Y.E., Bachet, B., & Imberty, A. (1996). Crystal and molecular structure of a histo-blood group antigen involved in cell adhesion: the Lewis x trisaccharide. *Glycobiology* **6**, 537-542.
44. Imberty, A., Mikros, E., Koca, J., Mollicone, R., Oriol, R., & Perez, S. (1995). Computer simulation of histo-blood group oligosaccharides: energy maps of all constituting disaccharides and potential energy surfaces of 14 ABH and Lewis carbohydrate antigens. *Glycoconj. J.* **12**, 331-349.

45. Hellstrom, I., Garrigues, H.J., Garrigues, U., & Hellstrom, K.E. (1990). Highly tumor-reactive, internalizing, mouse monoclonal antibodies to Le(y)-related cell surface antigens. *Cancer Res.* **50**, 2183-2190.
46. Schuermann, J.P., Henzl, M.T., Deutscher, S.L., & Tanner, J.J. (2004). Structure of an anti-DNA fab complexed with a non-DNA ligand provides insights into cross-reactivity and molecular mimicry. *Proteins* **57**, 269-278.
47. Chi, S.W., Maeng, C.Y., Kim, S.J., Oh, M.S., Ryu, C.J., Kim, S.J., Han, K.H., Hong, H.J., & Ryu, S.E. (2007). Broadly neutralizing anti-hepatitis B virus antibody reveals a complementarity determining region H3 lid-opening mechanism. *Proc. Natl. Acad. Sci. U. S. A* **104**, 9230-9235.

Chapter

4

Cloning, expression, purification, crystallization and preliminary X-ray diffraction analysis of chlorite dismutase: a detoxifying enzyme producing molecular oxygen.

Daniël C. de Geus, Ellen A.J. Thomassen, Clarisse L. van der Feltz and Jan Pieter Abrahams

Acta Crystallogr. Sect. F. Struct. Biol. Cryst. Commun. (2008) **64**:730-2.

Abstract

Chlorite dismutase, a multimeric haem-based protein, is one of the key enzymes of (per)chlorate reducing bacteria. It is highly active (>2 kU/mg) in reducing the toxic compound chlorite into the innocuous chloride anion and molecular oxygen. Chlorite itself is produced as the intermediate product of (per)chlorate reduction. We have identified the chlorite dismutase gene in *Azospira oryzae* strain GR-1 employing degenerate primers and subsequently overexpressed the active enzyme in *Escherichia coli*. Chlorite dismutase was purified, proven to be active, and crystallized using sitting-drops with PEG 2000 MME, KSCN and ammonium sulfate as the precipitants. The crystals belong to space group $P2_12_12$, with most likely 6 subunits in the asymmetric unit. Refined unit-cell parameters are $a = 164.46$, $b = 169.34$, $c = 60.79$ Å. The crystals diffract X-rays to 2.1 Å resolution on a synchrotron-radiation source and a three wavelength MAD dataset has been collected. Determination of the chlorite dismutase structure will provide insights into the active site of the enzyme, for which no structures are currently available.

4.1 Introduction

Azospira oryzae strain GR-1 (DSM 11199) is one of the first described perchlorate-reducing bacteria^{1,2}. The key enzymes of the dissimilatory (per)chlorate reducing pathway, (per)chlorate reductase and chlorite dismutase (Cld), were originally purified and characterized from this organism^{3,4}. Besides perchlorate (ClO_4^-) and chlorate (ClO_3^-) it can utilize O_2 , NO_3^- and Mn(IV) as electron acceptors, while using various carbon compounds, *e.g.* fatty acids and dicarboxylic acids, or hydrogen as electron donor¹.

Complete reduction of ClO_4^- into Cl^- and O_2 occurs in a few steps: ClO_4^- is reduced to ClO_3^- by a (per)chlorate reductase [EC 1.97.1.1]. Subsequently, the same enzyme catalyzes the reduction of ClO_3^- to ClO_2^- . The (per)chlorate reductase has a molecular mass of 420 kD with subunits of 95 and 40 kD (in an $\alpha_3\beta_3$ composition) containing one [3Fe-4S] cluster, two [4Fe-4S] clusters and one molybdenum cofactor per heterodimer. Although many denitrifying bacteria can reduce ClO_3^- to ClO_2^- , the latter compound is toxic to these cells³.

(Per)chlorate respiration is made possible by the action of yet another enzyme, chlorite dismutase (EC 1.13.11.49) which reduces the toxic ClO_2^- to environmentally innocuous Cl^- while producing O_2 . Cld is a multimeric protein containing one iron protohaem IX per 30 kDa subunit^{4,5}. Iron-protoporphyrin IX or haem is a ubiquitous enzyme cofactor in nature and haem-based proteins are known to catalyze a wide range of biologically

important reactions in all kingdoms of life ^{6;7}. However, knowledge about the biochemistry of the (per)chlorate reductive pathway is still limited.

Determination of the structure of Cld may offer insights into the mechanism of the final step in (per)chlorate reduction. We anticipate that the structural analysis will also open up new ways in bioremediative technology of oxochlorate contaminated water.

Here we report the overexpression, purification, crystallization and preliminary X-ray analysis of Cld from *Azospira oryzae* strain GR-1.

4.2 Experimental procedures

4.2.1 Selection of the *cld* gene for overexpression

Azospira oryzae strain GR-1, previously known as bacterial strain GR-1, was grown on chlorate containing medium and the native chlorite dismutase was purified as described before ⁵.

The N-terminal amino acid sequence was determined by selecting the 30 kD band of the purified, native Cld monomer from a 15% SDS-PAGE gel. This sample was subjected to 11 cycles of Edman (phenylisothiocyanate) degradation (Eurosequence, the Netherlands).

The resulting sequence (M/S)QPMQ(P/A)MKIER was reverse translated and used to design degenerate forward primers. However, it became also clear that the *Azospira oryzae* Cld N-terminus is nearly identical to that of 11 N-terminal amino acids of *Dechloromonas aromatica* Cld, which is MQPMQSMKIER. The backward degenerate primer was therefore based on

the DNA sequence corresponding to the C-terminus of *Dechloromonas aromatica* Cld. Combination of these primers yielded a 747 basepair product in a PCR reaction with *Azospira* whole cells. The fragment was purified on an agarose gel and sequenced (Baseclear, the Netherlands).

Although the gene amplified by PCR was now available, generating the restriction sites and insertion into the plasmid was unsuccessful. Due to these practical problems, the *cld* gene was chemically synthesized and cloned into pET28a using NdeI and BamHI restriction sites, creating the vector pET28a-CDBC (Baseclear, the Netherlands) that includes an N-terminal His tag and a thrombin cleavage site. The resulting expressed protein from this plasmid carries 20 extra amino acids at the N-terminus, MGSSHHHHHSSGLVPRGSH. The new construct was sequenced again, shown to be free of mutations or other errors and transformed into *E. coli* BL21(DE3)pLysS cells.

4.2.2 Overexpression and purification of Cld

To produce haem-containing protein for crystallization and subsequent structural analysis, 10 ml cultures were grown overnight on a rotary shaker (220 rpm) at 310 K. Erlenmeyer flasks with 500 ml LB medium including hemin ($40 \mu\text{g ml}^{-1}$), kanamycin ($50 \mu\text{g ml}^{-1}$) and chloramphenicol ($25 \mu\text{g ml}^{-1}$) were inoculated 1:50 from these overnight cultures. Growth was continued under the same conditions until the absorbance at 600 nm reached a value of 0.5. The temperature of the incubator was lowered to 303 K and 1 mM IPTG was added. Cultures were left to grow overnight (approximately

16 h) and cells were harvested by centrifugation at 277 K. Pellets were frozen immediately for storage prior to purification.

To purify Cld, cell paste from 0.5 l culture was resuspended in 10 ml of buffer A (20 mM Tris-HCl buffer pH 7.5, 500 mM NaCl) with 50 mM imidazole. Benzonase (50 units; Sigma-Aldrich) was added to reduce the viscosity due to released DNA and cells were disrupted by sonication on ice. The lysate was centrifuged and loaded onto a 5 ml HisTrap FF crude column. The column was washed with 5 column volumes of 20 mM Tris-HCl buffer pH 7.5, 500 mM NaCl and 50mM imidazole and the bound protein was directly eluted with 20 mM Tris-HCl buffer pH 7.5, 500 mM NaCl and 500mM imidazole. After a step elution of five column volumes of buffer A supplemented with 500 mM imidazole the Cld was desalted on a HiPrep 26/10 column equilibrated with 20 mM Tris-HCl pH 7.5. Subsequently, Cld was bound to a resource S cation exchange column, washed with the low ionic strength desalting buffer and eluted with a gradient of 0 to 1 M NaCl in 20 mM Tris-HCl pH 7.5. A highly concentrated, dark red fraction corresponding to active Cld eluted at approximately 135 mM NaCl. This solution was loaded onto a HiLoad 16/60 Superdex 200 prep grade column equilibrated with 20 mM Tris-HCl pH 7.5, 135 mM NaCl. At a low flow rate (0.3 ml min⁻¹) the red colored, multimeric species was separated from a small amount of colorless monomeric Cld. All columns were obtained from Amersham Biosciences (Sweden), mounted on an Äktexpress protein purification system (GE Healthcare) and all purification steps were performed at 277 K. The haem containing Cld fractions of the gelfiltration step were combined and

concentrated to 75 mg ml^{-1} using an Amicon concentrator. The purified Cld was stored in 20 mM Tris-HCl pH 7.5, 135 mM NaCl at 193 K until further use.

To assay the activity of the monomeric and multimeric Cld, one μl sample (15 mg ml^{-1}) was mixed with an equal volume of a 15 mM ClO_2^- solution and observed through a microscope. When multimeric Cld was used gas bubbles evolved immediately upon mixture of the droplets indicating that the multimeric Cld used in the crystallisation experiments is in the active form.

4.2.3 Crystallization and data collection

Prior to crystallization, the protein sample was filtered through a low binding protein 0.22 μm filter (Millipore) to remove dust particles and protein precipitate. Crystallization attempts were made using different commercially available screens. Thin needle shaped crystals were observed in the JCSG+ screen (Qiagen) condition 81, 0.1M potassium thiocyanate and 30 % (w/v) PEG MME2000. This condition was optimised on Q-plates using sitting drop vapour-diffusion at 295 K and a grid with 0 - 1.0 M potassium thiocyanate, 0 - 35 % (w/v) PEG MME 2000 in a pH range from 3.6 - 9.0 using different buffers. Therefore one μl of protein (6 mg ml^{-1} in 20 mM Tris-HCl pH 7.5, 135 mM NaCl) and 1 μl reservoir solution were mixed and equilibrated against 750 μl of the same reservoir solution. Very thin rectangular plate-shaped crystals appeared in 100 mM MES

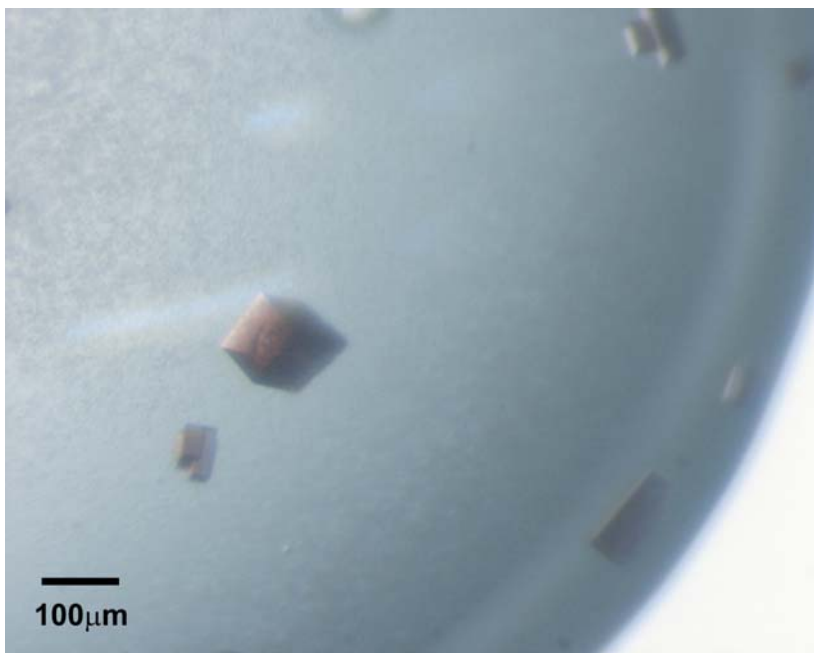


Figure 1 Crystals of Cld grown in 0.1 M MES pH 5.5, 25 % (w/v) PEG MME 2K, 0.3 M KSCN, 5 % glycerol and 180 mM ammonium sulfate. Maximum dimensions were reached after 7-10 days.

buffer pH 5.5, 25 % (w/v) PEG MME 2000, 0.3 M KSCN. This condition was further optimized using the additive screen (Hampton Research). Hence 1 μl of protein (6 mg ml^{-1} in 20 mM Tris-HCl pH 7.5, 135 mM NaCl) and 1 μl reservoir solution (100 mM MES buffer pH 5.5, 25 % (w/v) PEG MME 2000, 0.3 M KSCN) were mixed with 0.2 μl additive solution. The condition with 0.1 M $(\text{NH}_4)_2\text{SO}_4$ as the additive resulted in bigger crystals. Finally the $(\text{NH}_4)_2\text{SO}_4$ concentration was varied between 0.05 M and 0.3 M with or without the addition of 5 % (v/v) glycerol. Triangular plates, cubic

and bipyramidal crystals up to approximately $100 \times 100 \times 100 \mu\text{m}^3$ in size were grown from well solutions containing 100 mM MES buffer pH 5.5, 25 % (w/v) PEG MME 2000, 0.3 M KSCN, 5% (v/v) glycerol and 160-260 mM $(\text{NH}_4)_2\text{SO}_4$. An example of a cubic shaped Cld crystal is shown in Figure 1. The two other crystal shapes were also tested but appeared to be of less diffraction quality. The data were not sufficient to determine whether all these crystal shapes belong to the same space group.

Prior to data collection at cryogenic temperatures crystals were soaked in a solution containing the mother liquor including 16% glycerol and flash-frozen in a stream of nitrogen gas at 100 K using an Oxford Cryosystems Cryostream device. Multiple wavelength anomalous dispersive (MAD) data were collected using an ADSC Quantum Q315r detector on beamline ID23-1 at the ESRF, Grenoble, France. Three wavelengths were chosen near the iron-absorption edge based on an X-ray fluorescence scan of the frozen crystal. The f'' component (peak) and the $\Delta f'$ (remote) were maximized, while the f' component (inflection) was minimized. Data were collected with a 1° rotation and 0.2 seconds exposure time per frame. The intensities were indexed with MOSFLM ⁸ and scaled using SCALA ⁹ from the CCP4 program suite ¹⁰.

The refined unit-cell parameters are $a = 164.46$, $b = 169.34$, $c = 60.79 \text{ \AA}$ and analysis of the X-ray diffraction pattern showed that along the h and k axis reflections were only present if $h, k, = 2n$, identifying the space group as $P2_12_12$. A Matthews coefficient ¹¹ of $2.54 \text{ \AA}^3/\text{Da}$ suggested the presence of 6 subunits of 28 kDa in the asymmetric unit, corresponding to 51.6 % solvent content. Statistics of the data collection are shown in Table 1. The six iron sites

Table 1 Data-collection and processing parameters for a single Cld crystal. Data statistics of the outer resolution shell are given in parentheses, where applicable.

	Peak	Inflection point	High energy remote
Crystal dimensions (μm^3)	$80 \times 80 \times 80$	$80 \times 80 \times 80$	$80 \times 80 \times 80$
Temperature (K)	100	100	100
Crystal system	orthorhombic	orthorhombic	orthorhombic
Space-group	P2 ₁ -2 ₁ -2	P2 ₁ -2 ₁ -2	P2 ₁ -2 ₁ -2
Unit cell parameters (Å)	$a = 164.71, b = 169.55, c = 60.85$	$a = 165.00, b = 169.80, c = 60.92$	$a = 164.46, b = 169.34, c = 60.79$
Wavelength (Å)	1.7382	1.7399	0.9834
Resolution range (Å)	50-2.7 (2.85-2.70)	50-2.9 (3.06-2.90)	40.13-2.1 (2.21-2.1)
Reflections	660269 (96695)	538131 (78769)	731403 (107833)
Unique reflections	47838 (6864)	38886 (5579)	100003 (14403)
Redundancy	13.8 (14.1)	13.8 (14.1)	7.3 (7.5)
R_{sym}^a (%)	10.7 (41.0)	10.9 (42.0)	10.5 (48.8)
Completeness (%)	100 (100)	100 (100)	100 (100)
Mean ((I)/sd(I))	25.1 (6.3)	25.3 (6.1)	15.8 (3.8)
R_{anom}^b (%)	3.8 (10.9)	3.4 (10.9)	4.3 (19.3)
Anom multiplicity	7.2 (7.2)	7.3 (7.3)	3.7 (3.7)
Anom completeness (%)	100 (100)	100 (100)	100 (100)

^a $R_{\text{sym}} = \sum_h \sum_i |I_{hi} - \langle I_{hi} \rangle| / \sum_h \sum_i |I_{hi}|$, where I_{hi} is the intensity of the i th measurement of the same reflection and $\langle I_{hi} \rangle$ is the mean observed intensity for that reflection

^b $R_{\text{anom}} = \sum_h |I_{hi} - \langle I_{hi} \rangle| / \sum_h \langle I_{hi} \rangle$, where I_{hi} and $\langle I_{hi} \rangle$ are Friedel pairs

could be identified, phases could be obtained and model building has been started. The phasing and the structure determination will be described in detail in the next chapter.

References

1. Rikken, G.B., Kroon, A.G.M., & van Ginkel, C.G. (1996). Transformation of (per)chlorate into chloride by a newly isolated bacterium: Reduction and dismutation. *Applied Microbiology and Biotechnology* **45**, 420-426.
2. Wolterink, A., Kim, S., Muusse, M., Kim, I.S., Roholl, P.J., van Ginkel, C.G., Stams, A.J., & Kengen, S.W. (2005). *Dechloromonas hortensis* sp. nov. and strain ASK-1, two novel (per)chlorate-reducing bacteria, and taxonomic description of strain GR-1. *Int. J. Syst. Evol. Microbiol.* **55**, 2063-2068.
3. Kengen, S.W., Rikken, G.B., Hagen, W.R., van Ginkel, C.G., & Stams, A.J. (1999). Purification and characterization of (per)chlorate reductase from the chlorate-respiring strain GR-1. *J. Bacteriol.* **181**, 6706-6711.
4. van Ginkel, C.G., Rikken, G.B., Kroon, A.G., & Kengen, S.W. (1996). Purification and characterization of chlorite dismutase: a novel oxygen-generating enzyme. *Arch. Microbiol.* **166**, 321-326.
5. Hagedoorn, P.L., De Geus, D.C., & Hagen, W.R. (2002). Spectroscopic characterization and ligand-binding properties of chlorite dismutase from the chlorate respiring bacterial strain GR-1. *Eur. J. Biochem.* **269**, 4905-4911.
6. Wilson, M.T. & Reeder, B.J. (2008). Oxygen-binding haem proteins. *Exp. Physiol* **93**, 128-132.
7. Hou, S., Larsen, R.W., Boudko, D., Riley, C.W., Karatan, E., Zimmer, M., Ordal, G.W., & Alam, M. (2000). Myoglobin-like aerotaxis transducers in Archaea and Bacteria. *Nature* **403**, 540-544.
8. Leslie, A.G. (1999). Integration of macromolecular diffraction data. *Acta Crystallogr. D. Biol. Crystallogr.* **55**, 1696-1702.
9. Evans, P. (2006). Scaling and assessment of data quality. *Acta Crystallogr. D. Biol. Crystallogr.* **62**, 72-82.

Chapter 4

10. (1994). The CCP4 suite: programs for protein crystallography. *Acta Crystallogr. D. Biol. Crystallogr.* **50**, 760-763.
11. Matthews, B.W. (1968). Solvent content of protein crystals. *J. Mol. Biol.* **33**, 491-497.

Chapter

5

Crystal structure of chlorite dismutase, a detoxifying enzyme producing molecular oxygen

**Daniël C. de Geus, Ellen A.J. Thomassen, Peter-Leon Hagedoorn,
Navraj S. Pannu, Esther van Duijn and Jan Pieter Abrahams**

J. Mol. Biol. (2009) **387**: 192-206.

Abstract

Chlorite dismutase is a key enzyme of perchlorate and chlorate respiration. This haem-based protein reduces the toxic compound chlorite in a very efficient way into the innocuous chloride anion while producing molecular oxygen. A sequence comparison between Cld homologues shows a highly conserved family. The crystal structure of *Azospira oryzae* strain GR-1 chlorite dismutase is reported to 2.1 Å resolution. The structure reveals a hexameric organisation of the Cld while each monomer exhibits a ferredoxin-like fold. The six subunits are organized in a ring structure with a maximal diameter of 9 nm and an inner diameter of 2 nm. The haem active site pocket is solvent accessible both from the inside and the outside of the ring. Moreover, a second anion binding site has been identified near the active site which could accommodate the assumed reaction intermediate ClO^- for further transformation.

The environment of the haem cofactor was investigated using EPR spectroscopy. Apart from the high-spin ferric signal of the five-coordinate resting state enzyme, two low-spin signals were found corresponding to six-coordinate species. The current crystal structure confirms and complements a recently proposed catalytic mechanism that proceeds via a ferryl species and a ClO^- anion. Our structural data exclude co-operativity between the iron centers.

5.1 Introduction

Chlorite dismutase (Cld) catalyzes the reduction of the toxic compound ClO_2^- to environmentally innocuous Cl^- while producing O_2 . This detoxification reaction is an essential step in the dissimilatory perchlorate reductive pathway. Recently, (per)chlorate reducing bacteria have attracted attention due to their potential usefulness in remediation of water contaminated with oxyanions of chlorine. The toxic compounds perchlorate (ClO_4^-), chlorate (ClO_3^-), chlorite (ClO_2^-), hypochlorite (ClO^-) are not formed on a large scale in nature. Although traces of perchlorate are found in Chile saltpeter, the use of such fertilizer has not been associated with the current contamination levels. The occurrence of harmful quantities of chloro-oxyanions in surface and groundwaters in the United States is caused by the large scale chemical production, the wide range of applications and the chemical stability of chlorine anions in water. Most of the ClO_4^- contamination in the environment originates from its use in ammonium perchlorate as the solid oxidant in rocket propulsion, explosives and fireworks¹. ClO_3^- is used as a herbicide^{2,3}, and it is released when chlorine dioxide (ClO_2) is used as a bleaching agent in paper and pulp industry. ClO_2^- is a drinking water disinfection byproduct with potential nervous system effects for children and a suspected health risk concerning anemia. The Environmental Protection Agency has therefore limited the maximum ClO_2^- concentration in drinking water to one milligram per litre⁴. *Azospira oryzae* strain GR-1 (DSM 11199) is one of the first described perchlorate-reducing bacteria^{5,6}. This organism and its biochemical pathways that

completely reduce ClO_4^- and ClO_3^- to Cl^- plus O_2 via the ClO_2^- intermediate have been researched for more than a decade. This research was inspired by potential practical applications in waste water treatment and by fundamental interest in the mechanism of chlorite transformation. The key enzymes of the dissimilatory (per)chlorate reducing pathway, (per)chlorate reductase and Cld, were originally purified and characterized from *Azospira oryzae* strain GR-1^{7,8}. It was discovered that complete reduction of ClO_4^- by *Azospira oryzae* strain GR-1 into Cl^- and O_2 occurs in a few steps. First ClO_4^- is reduced to ClO_3^- by a (per)chlorate reductase [EC 1.97.1.1]. Subsequently, the same enzyme catalyzes the reduction of ClO_3^- to ClO_2^- . Finally, Cld (EC 1.13.11.49) converts the ClO_2^- into Cl^- while producing O_2 . The (per)chlorate reductase contains one [3Fe-4S] cluster, two [4Fe-4S] clusters and one molybdenum cofactor per $\alpha_3\beta_3$ heterodimer and produces a water molecule at each successive $2e^-$ reduction step. Although many denitrifying bacteria can reduce ClO_3^- to ClO_2^- using nitrate reductase, the latter compound is toxic to these cells⁷.

Cld is a multimeric protein containing one iron protohaem IX per 28 kDa subunit^{8,9}. Intriguing properties of this enzyme are the extraordinary specificity for chlorite and the efficiency of the chlorite conversion. Moreover, currently Cld is the only known haem-based enzyme which is able to perform O-O bond formation catalysis as its primary function. An introduction to the current biochemical knowledge about chlorite dismutase has been written by Streit and DuBois¹⁰. Very recently a mechanism involving a compound I intermediate and subsequent recombination of the resulting hypochlorite and compound I was proposed for the chlorite

dismutase reaction. High-valent oxo intermediates were characterized by stopped-flow UV-vis spectroscopy in this study ¹¹. Here, we report the crystal structure of Cld, new insights into the quaternary state of the protein and the structural implications for the proposed catalytic mechanism.

5.2 Experimental procedures

5.2.1 Cloning, overexpression and purification of Cld from *Azospira oryzae* strain GR-1

The Cld gene was chemically synthesized without the region coding for the signal sequence and then cloned into the pET28a vector, creating the vector pET28a-CDBC (BaseClear, the Netherlands). The resulting expressed protein from this plasmid includes a His-tag with a thrombin cleavage site, extending the amino terminus with 20 extra amino acids: MGSSHHHHHSSGLVPRGSH. The protein used in the crystallisation trials was digested with thrombin to remove this linker. Details about the cloning, overexpression and purification of Cld have been described ¹². The specific activity of the purified Cld was $1.5 (\pm 0.5) \times 10^3 \mu\text{mol ClO}_2^- \text{min}^{-1} \text{mg}^{-1}$.

5.2.2 Determination of Stokes radius

The molecular Stokes radius of Cld was estimated by calibrated gel filtration chromatography on an ÄKTExpress protein purification system

(GE Healthcare). A HiLoad 16/60 Superdex 200 prep-grade column equilibrated with 20 mM Tris-HCl pH 7.5, 135 mM NaCl was run at a low flow rate (0.3 ml min^{-1}). The column was calibrated using the following gel filtration standards (Bio-Rad) with known molecular weights and radii: thyroglobulin (670 kD, 86.0 Å), bovine gamma globulin (158 kD, 52.3 Å), chicken ovalbumin (44 kD, 30.5 Å) and equine myoglobin (17 kD, 19.1 Å)^{13;14}. Samples were loaded onto the Superdex column and the relative elution volume ($-\log K_{av}$)^{1/2} plotted versus the molecular Stokes radius. The partition coefficient, K_{av} , was calculated from the elution volume of the protein, V_e , and the total gel bed volume, V_t , using the expression $K_{av} = (V_e - V_0) / (V_t - V_0)$. The void volume, V_0 , was determined by running blue dextran (average molecular weight 2000 kD) through the Superdex column.

5.2.3 Mass Spectrometry

Mass spectrometry (MS) measurements were performed in positive ion mode using an electrospray ionization time-of-flight (ESI-TOF) instrument (LCT, Waters, UK) equipped with a Z-spray nano-electrospray ionization source. Needles were made from borosilicate glass capillaries (Kwik-Fil, World Precision Instruments, Sarasota, FL) on a P-97 puller (Sutter Instruments, Novato, USA), coated with a thin gold layer by using an Edwards Scancoat (Edwards Laboratories, Milpitas, USA) six Pirani 501 sputter coater.

Chlorite dismutase was buffer exchanged to 50 mM ammonium acetate pH 6.8 using centrifugal filter units with a cut-off of 30kDa (Millipore, UK).

Chlorite dismutase was analyzed at a monomer concentration of 5 μ M. To produce intact gas phase ions from large complexes in solution, the source was operated at a pressure of 6.7 mbar¹⁵. Mass spectra were recorded with a capillary voltage of 1.3 kV and cone voltage of 200 V. The ToF pressure was $1.2 \cdot 10^{-6}$ mbar. Spectra were mass calibrated using an aqueous solution of CsI (25 mg/ml).

5.2.4 Tandem Mass Spectrometry

Tandem mass spectra were recorded on a modified Q-ToF 1 instrument (Waters, UK) in positive ion mode. The pressure in the source region was increased to 10 mbar. Xenon was used as collision gas at a pressure of 1.5–2 mbar. The capillary voltage and cone voltages were kept at 1400 and 175V respectively. The collision voltage was varied from 10 to 200V.

5.2.5 Activity assay with the Clark oxygen electrode

Cld activity was measured amperometrically by the evolution of O₂ using a modified Clark electrode (YSI) with home-made instrumentation, a Labview interface (National Instruments) and home-made Labview data acquisition and analysis software as described previously¹⁶. The assay was performed in 100 mM KP_i, pH 7.0 at 25 °C. After removal of oxygen by bubbling with high-purity argon, NaClO₂ was added to 6mM final concentration. The reaction was started by adding 2–8 nM (final concentration) of Cld.

5.2.6 EPR spectroscopy and redox titration

To determine the midpoint potential of the haem iron of Cld, an EPR monitored redox titration was performed in an anaerobic glovebox (Coy). The titration buffer was 50 mM KP_i pH 7.2 with 10 % glycerol. A mediator mix was prepared in the same buffer containing per 100 ml 2.6 mg N,N,N',N'-tetramethyl-p-phenylenediamine, 5.2 mg dichlorophenol indophenol, 5.4 mg phenazine ethosulfate, 6 mg methylene blue, 3.8 mg resorufine, 7.5 mg indigodisulfonate, 2.8 mg 2-OH-1,4-naphtaquinone, 5.3 mg anthraquinone-2-sulfonate, 5.2 mg phenosafranin, 5.6 mg safranin O, 4.6 mg neutral red, 6.6 mg benzyl viologen and 5 mg methyl viologen. To the titration vessel 0.32 ml 1.5 mM Cld, 1.0 ml mediator mix and 1.28 ml titration buffer were added. The titration cell was connected to a reference Ag/AgCl electrode (SSE) and a platinum wire electrode. The electrodes were connected to a voltmeter. The potential was varied using sodium dithionite and potassium ferricyanide as reductor and oxidator, respectively. At various potentials, samples of 200 μ l were taken from the titration vessel, transferred to an EPR tube, and immediately frozen in liquid nitrogen. EPR data were recorded on a Bruker ER200D EPR spectrometer with Labview interface (National Instruments) and home-made Labview data acquisition and analysis software, the liquid helium cooling was as previously described¹⁷. The microwave frequency was measured with a HP5350B microwave frequency counter. The modulation frequency was always 100 kHz.

5.2.7 Crystallisation

The crystallisation of Cld has been published in details elsewhere ¹². In short, after optimisation trials, dark red cubic crystals up to approximately $100 \times 100 \times 100 \mu\text{m}^3$ in size could be grown from well solutions containing 100 mM MES buffer pH 5.5, 25 % (w/v) PEG MME 2000, 0.3 M KSCN, 5% (v/v) glycerol and 160-260 mM $(\text{NH}_4)_2\text{SO}_4$. The crystals were soaked in a solution containing the mother liquor including 16% glycerol prior to data collection.

5.2.8 Crystallographic data collection and processing

A MAD dataset was collected on beam-line ID23-1 at the European Synchrotron Radiation Facility (ESRF) at a wavelength of 1.7382 Å (peak), 1.7399 Å (inflection point) and 0.98340 Å (high energy remote) using the anomalous signal of the iron atoms. The crystal was flash-frozen and kept at 100K during data collection and 360 images were collected for the peak and inflection point and 185 images for the high energy, all with a rotation angle of 1°. Reflections were integrated with MOSFLM ¹⁸ and merged with SCALA ¹⁹ from the CCP4 suite ²⁰. For data statistics see Table I and ¹².

5.2.9 Structure solution and refinement

The structure was built automatically, with over 90% of the residues correctly docked, with the Crank ²¹ structure solution suite (version 1.2.0) using the three wavelength MAD data. Crank used Scaleit ²⁰ for scaling the

data sets, Afro (Pannu, in preparation) for Fa estimation, Crunch2²² for substructure determination, Bp3²³ for phasing, Solomon²⁴ for enantiomorph determination and density modification and Buccaneer²⁵ with Refmac5²⁶ using the MLHL function²⁷ for automated model building and refinement.

Manual rebuilding of the model and addition of the unbuilt residues was done with COOT²⁸. Refinement to 2.1 Å resolution was done using REFMAC including NCS restraints for residues 10-217 and 231-248 and water molecules were added using COOT. Illustrations were prepared using PyMOL²⁹.

5.3 Results and Discussion

5.3.1 Structure determination

The structure of Cld was determined by three-wavelength multiple anomalous dispersion (MAD) using the anomalous signal from iron atoms. The Cld crystallised in space group P2₁2₁2, with unit cell dimensions of 164.46 x 169.34 x 60.79 Å. The crystals contained six molecules in the asymmetric unit, which results in a solvent content of 52.6 % and a Wilson temperature factor of 26.6 Å². The electron density map for each monomer showed clear density of residues 8-217 and 231-248 (monomer A), 9-217 and 228-248 (monomer B), 10-217 and 229-248 (monomer C), 8-217 and 229-248 (monomer D), 8-217 and 229-248 (monomer E), 9-217 and 231-248 (monomer F). All monomers contain one protoporphyrin IX (haem) and one thiocyanate in the active site. In all but one monomer (monomer D

Table I Crystallographic data and refinement statistics

	Peak set	Inflection point	High energy remote
<i>A. Data collection</i>			
Beam-line	ESRF ID23-1	ESRF ID23-1	ESRF ID23-1
Wavelength (Å)	1.7382	1.7399	0.9834
Resolution range (Å)	50-2.7 (2.85-2.70) ^a	50-2.9 (3.86-2.90)	40.13-2.1 (2.21-2.10)
Reflections	660269 (96695)	538131 (78769)	731403 (107833)
Unique reflections	47838 (6864)	38886 (5579)	100003 (14403)
Multiplicity	13.8 (14.1)	13.8 (14.1)	7.3 (7.5)
Completeness (%)	100 (100)	100 (100)	100 (100)
Mean (I)/sd(I)	25.1 (6.3)	25.3 (6.1)	15.8 (3.8)
R _{sym} ^b (%)	10.7 (41.0)	10.9 (42.0)	10.5 (48.8)
Rano (%)	3.8 (10.9)	3.4 (10.9)	4.3 (19.3)
Ano multiplicity	7.2 (7.2)	7.3 (7.3)	3.7 (3.7)
Ano completeness(%)	100 (100)	100 (100)	100 (100)
<i>B. Phasing</i>			
Number of Fe-sites		6	
FOM Overall		0.214	
FOM 2.21-2.10 Å		0.04	
<i>C. Refinement</i>			
Resolution range (Å)		40.13-2.10 (2.15-2.10)	
No. of reflections used in refinement		94936 (6889)	
No. of reflections used for R-free		4994 (381)	
R-factor ^c		0.22 (0.25)	
R-free		0.25 (0.30)	
No. of protein / water atoms		10939 / 555	
Average B-value	protein / solvent (Å ²)	26.3/ 27.0	

Average B-value	haem / HCO ₃ ²⁻	20.9/ 42.2
	thiocyanate	20.1
Ramachandran statistics ^d (%)		94.7 / 5.3 / 0 / 0
R.m.s. deviations ^e (bonds, Å / angles, °)		0.013 / 1.298

^a Values in parentheses are for the highest resolution bin, where applicable.

^b $R_{\text{sym}} = \sum_h \sum_i |I_{hi} - \langle I_h \rangle| / \sum_h \sum_i |I_{hi}|$, where I_{hi} is the intensity of the i^{th} measurement of the same reflection and $\langle I_h \rangle$ is the mean observed intensity for that reflection.

^c $R = \sum ||F_{\text{obs}}(hkl)| - |F_{\text{calc}}(hkl)|| / \sum |F_{\text{obs}}(hkl)|$.

^d According to the program PROCHECK³⁰. The percentages are indicated of residues in the most favoured, additionally allowed, generously allowed and disallowed regions of the Ramachandran plot, respectively.

^e Estimates provided by the program REFMAC²⁶.

showed poor electron density) a hydrogen carbonate anion is present in close proximity of the haem. The final model has good stereochemistry and R-factors (Table I) and next to 10939 protein atoms it contains 6 haem molecules including 6 Fe³⁺, 6 thiocyanate molecules, 5 hydrogen carbonate anions and 555 water molecules.

5.3.2 Quaternary state of Cld

Cld forms a hexamer in the crystal. The six subunits form a 65 Å high ring with a maximum diameter of 90 Å. The inner diameter of the ring is approximately 20 Å (Figure 1). A surface area of ~ 3000 Å² per monomer is buried, which is within the range of true oligomeric protein contacts rather than non-specific crystal packing artefacts³¹. Previously, it was assumed that the wildtype and recombinant Cld from different sources formed

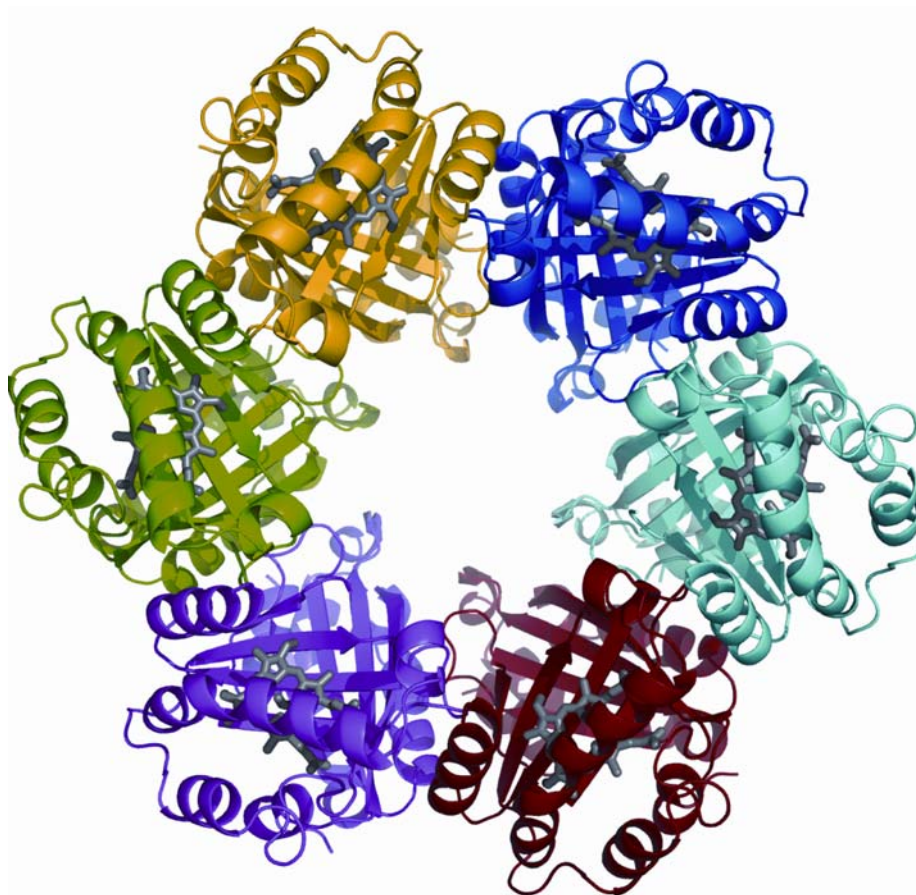


Figure 1 View of the chlorite dismutase quaternary fold. The six monomers are shown in different colors. The haem is depicted in sticks and colored grey in all monomers.

tetramers^{8;10;12;32;33}. These molecular weight determinations were based on analytical gel filtration experiments that were calibrated with globular protein standards. However, the elution position of a protein on a gel

filtration column is not correlated with molecular weight but instead is a function of the Stokes radius³⁴. Employing this relationship, it was found that the Cld ring structure present in the crystal elutes at the same elution volume as a globular tetramer would (Figure S1A and S1B).

In order to obtain a more accurate quaternary state determination of Cld in solution, native mass spectrometry was performed. The mass spectrum illustrates that the multimeric species of Cld in solution is preserved as a pentameric complex ion in the gas phase (Figure 2A). The monomeric mass of Cld shows two peaks with a 134 Da difference, which was interpreted as a loss of the N-terminal methionine during expression (Figure 2B). Using tandem mass spectrometry the stoichiometry of the Cld oligomer was confirmed to be a pentamer. By collisional activation of the ions a single highly charged monomer was ejected from the pentamer. Concomitantly the low charged tetramer counter complex ions were also observed.

It may be that the thiocyanate ion present in the crystallization condition affects the quaternary structure of Cld. Thiocyanate is a lipophilic ion that has the capacity to interfere with ionic pairs located either on the protein surface or the hydrophobic core of folded proteins. Moreover, thiocyanate dependent changes in quaternary state have been observed with flavoproteins previously^{35;36}. Low concentrations of thiocyanate did not affect the quaternary state, judged by mass spectrometry. Concentration levels of thiocyanate similar to that present in the mother liquor are too high for MS analysis.

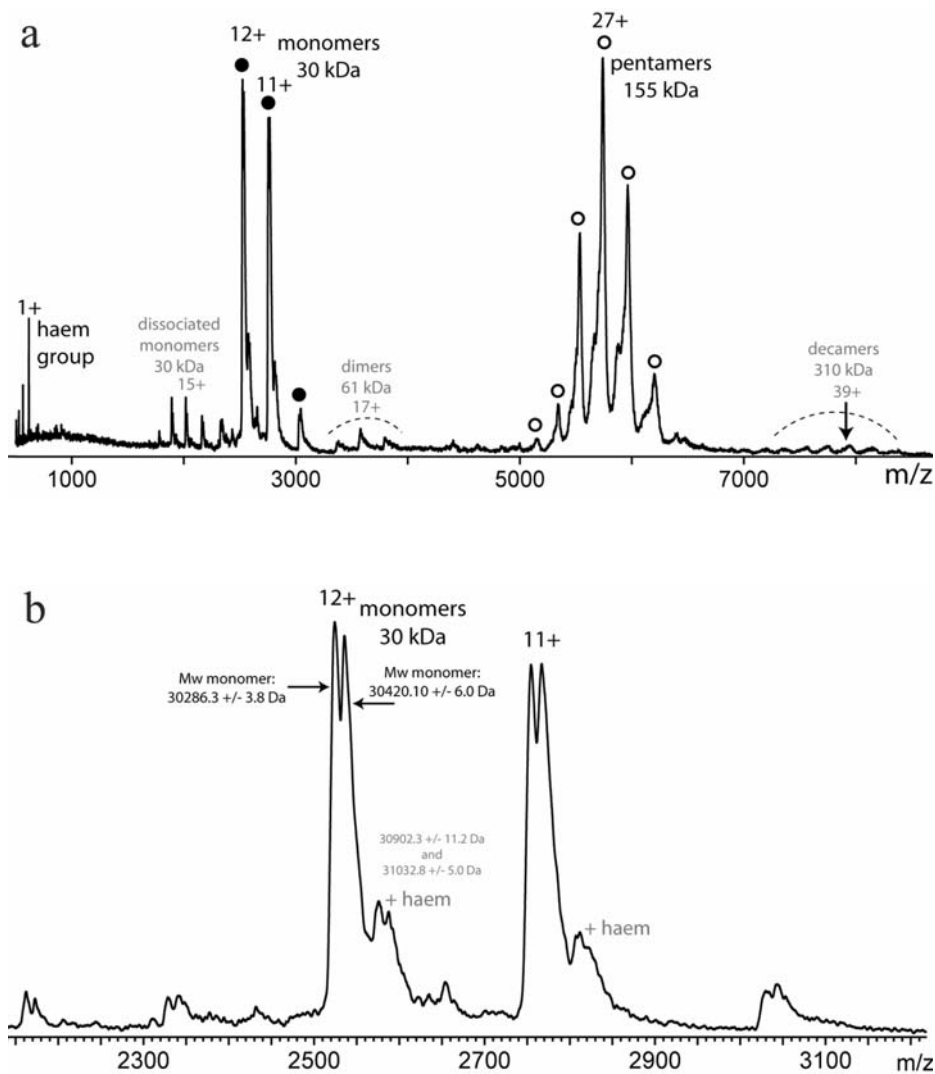


Figure 2 Native mass spectrometry of Cld. **a)** Main mass spectrum of Cld electrosprayed from an aqueous ammonium acetate solution. **b)** Close-up of the indicated region of the main spectrum showing the Cld monomeric mass.

5.3.3 Structure overview and the active site

The Cld monomer has an $\alpha+\beta$ structure consisting of an eight-stranded antiparallel β -sheet forming a β -barrel with the α -helices lying next to these sheets on the outside of the protein (Figure 3A). Each Cld monomer consists of two similar structural domains with a ferredoxin-fold (Figure 3B).

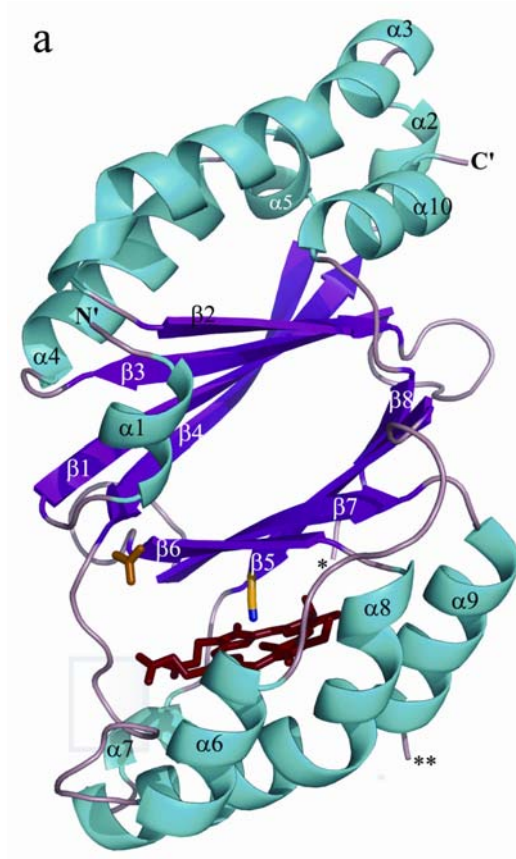


Figure 3 Cld secondary structure and haem cavity. **a)** View of the chlorite dismutase overall fold. The α helices and β strands are labelled according to the ferredoxin fold and colored light blue and purple, respectively. The haem is colored red with the coordinating thiocyanate in yellow and blue (nitrogen atom). The amino acids forming the hydrogen bond network (see also Figure 2) are located within the boundaries of the grey frame. The hydrogen carbonate anion located next to $\beta 6$, is colored in orange. In monomer A between ******(Leu217) and *****(Phe229) a part of the structure is not present due to a highly disordered loop. The picture was prepared with PyMol ²⁹.

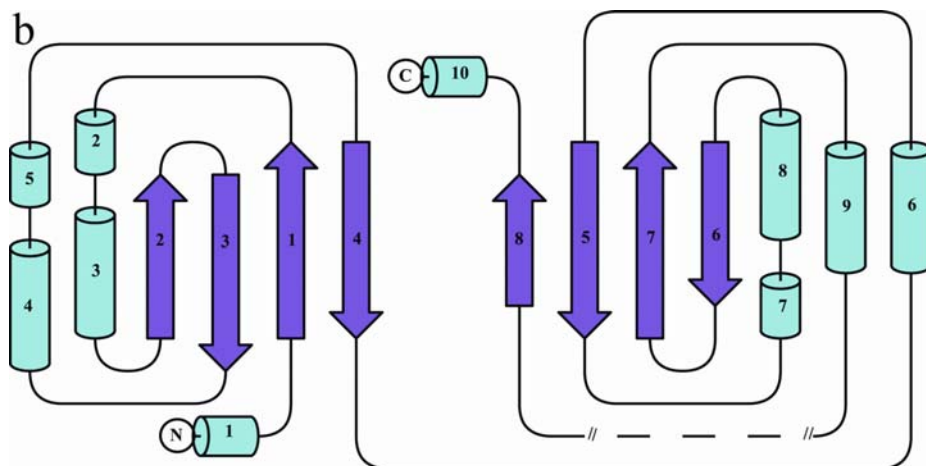


Figure 3 (continued) **b)** Topology diagram of chlorite dismutase. The α helices are depicted as cylinders and colored light blue, the β strands are depicted as arrows and colored purple. The $4\uparrow 1\downarrow 3\uparrow 2\downarrow$ and $8\uparrow 5\downarrow 7\uparrow 6\downarrow$ antiparallel β sheet is a distinct feature. The topology diagram has been prepared using TopDraw³⁷.

A single ferredoxin-fold contains a beta sheet formed by four antiparallel β -strands³⁸. In a Cld monomer the β -barrel is formed by the $4\uparrow 1\downarrow 3\uparrow 2\downarrow$ β -sheet from one domain and the topologically equivalent $8\uparrow 5\downarrow 7\uparrow 6\downarrow$ sheet from the other (haem binding) domain. A haem (protohaem IX) is bound in a well-defined pocket between beta strands ($\beta 5$ - $\beta 8$) and alpha helices ($\alpha 6$ - $\alpha 9$). This pocket is accessible from the inner channel as well as from the outside of the hexameric ring (Figure 3C). The surface of the cavity is created by 31 conserved, mainly hydrophobic residues (boxed residues in Figure 4). The iron atom in the haem cofactor is coordinated by His170 and (in our structure) a thiocyanate molecule. Thiocyanate was present in the mother

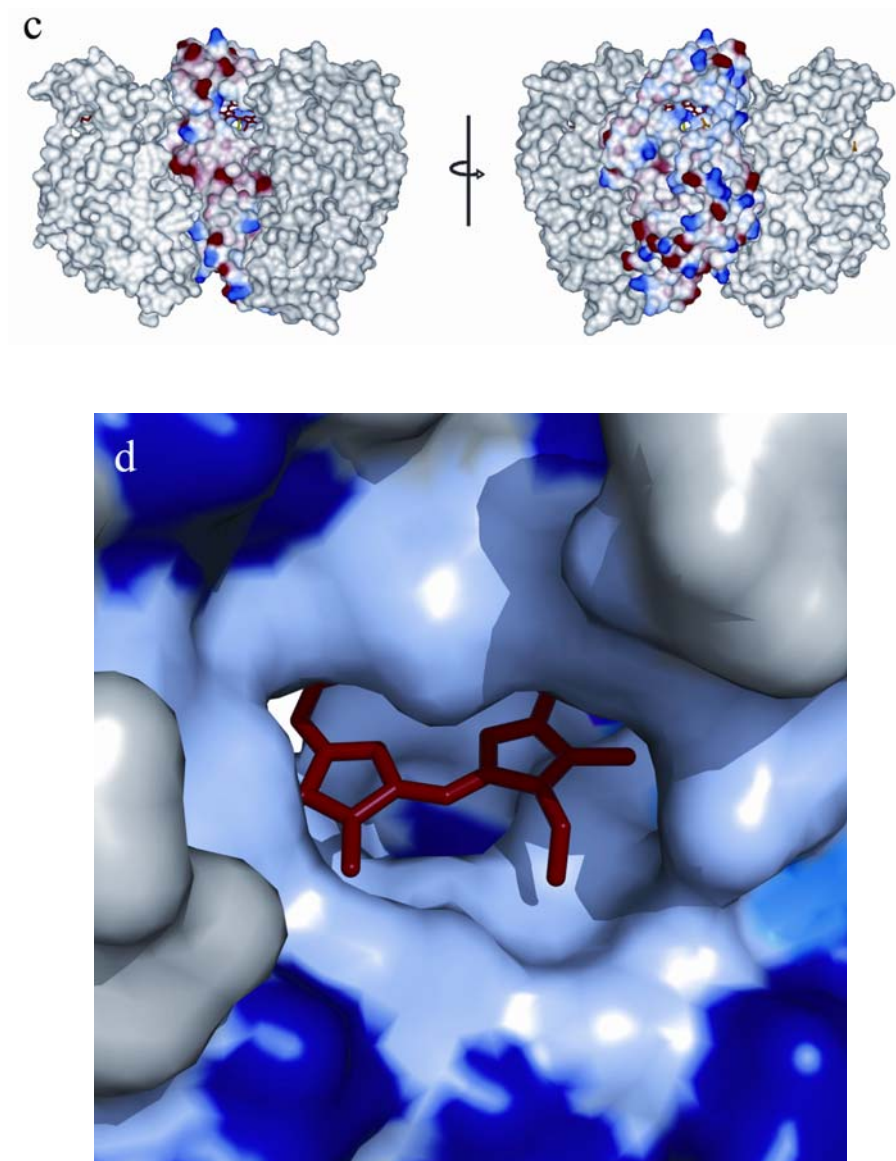


Figure 3 (continued) **c** Left: surface representation of three monomers viewed from the inside of the ring, perpendicular to the 6-fold non-crystallographic axis. Right: rotated

180° counter clockwise around the 6-fold non-crystallographic axis, showing the outside surface of the hexameric ring. The electrostatic surface of subunit A (negative and positive charges are indicated with red and blue, respectively) is represented amid the two flanking subunits E and F (grey surface). This figure shows the solvent accessibility of the haem cofactor (red) and the bound thiocyanate molecule (green). A hydrogen carbonate anion (orange) binds near the haem cavity at the end of a striking deep groove, present on the outer surface of each monomer. **d)** Surface representation of the Cld cavity. Increasing distances from the haem cofactor to amino acid residues are shown in different colors: up to 4 Å (light blue), 4-5 Å (marine blue), 5-6 Å (purple blue), and from 6-8 Å (dark blue). Residues further away from the haem are depicted in grey. This shows the binding pocket underneath the haem available for accomodating the ClO_2^- .

liquor at a concentration of 0.3 M. Cyanide is a strong inhibitor (100%) at 20 mM concentration when the reaction was performed in the presence of 15 mM chlorite⁸ and we assume that thiocyanate is also an inhibitor of the reaction, indicating that the structure represents an inhibited state of the enzyme. Presumably, the thiocyanate will be replaced by chlorite in the reaction. To accomodate the substrate a small distal cavity about 2 Å deeper (purple blue) than the surface of the surrounding haem cavity (light blue) is present (Figure 3D). The two propionate groups of the haem cofactor (Figure 5A) form hydrogen bonds with 3 water molecules and amino acid Asn117, Tyr118, Ile119, and Trp155. Residues 117-119 are present in the loop between β_4 and α_6 which connects the two ferredoxin-like domains. The Trp155 residue, present in α_7 , is conserved in all aligned sequences and resides in close proximity to the heme propionate side chain (Figure 3A and 4). The corresponding Trp189 residue from *Dechloromonas aromatica* Cld

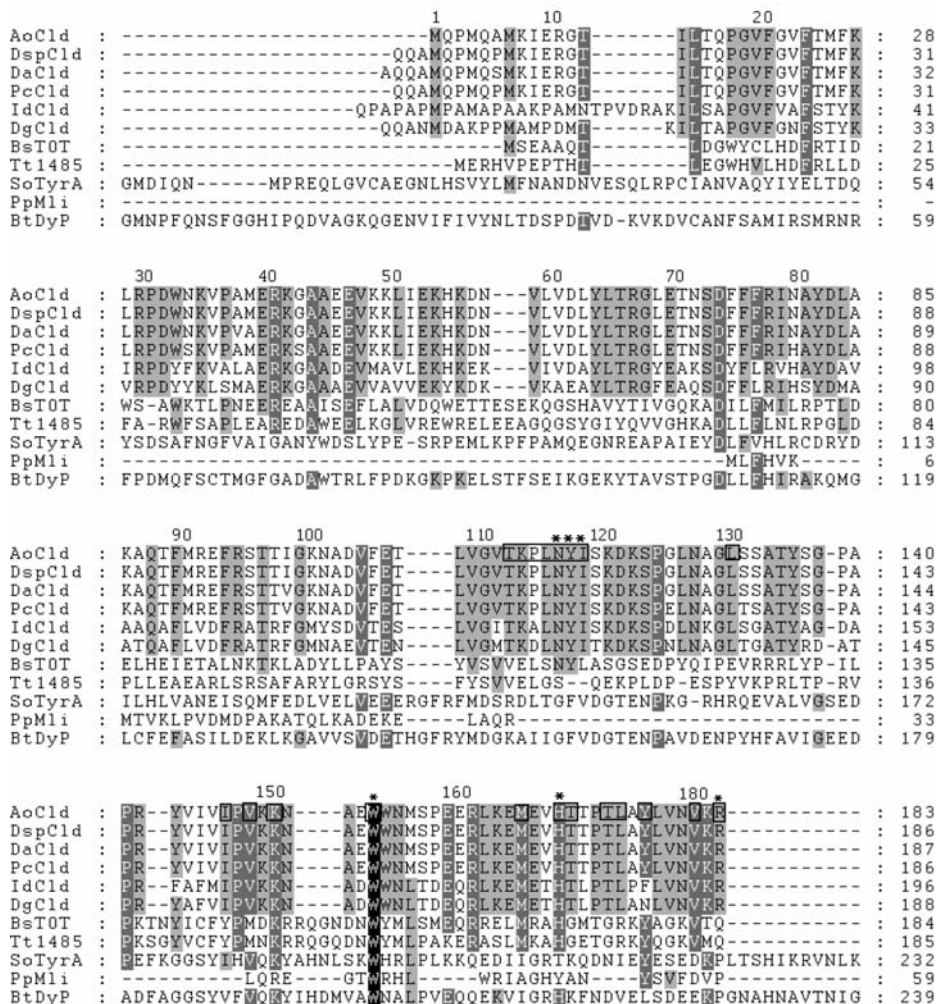


Figure 4 Multiple sequence alignment of *Azospira oryzae* strain GR-1 Cld and related proteins using ClustalW³⁹ and GeneDoc⁴⁰. The numbering is according to the residue numbers of AoCld in the PDB (entry 2vxh). The first 6 sequences are chlorite dismutases from the different organisms: AoCld, *Azospira oryzae* strain GR-1, DspCld, *Dechlorosoma* sp. KJ, DaCld, *Dechloromonas aromatica* RCB, PcCld, *Pseudomonas chloritidis*mutans, IdCld, *Ideonella dechloratans*, DgCld, *Dechloromonas agitata*. Signal

Crystal structure of Cld, a detoxifying enzyme producing molecular oxygen

	190	200	210	220	
AoCld :	-----KLYHSTGLDDTD* FI TYFETD DLTA EN NLM LS LA QVK--EN KFH V R W G :	228			
DspCld :	-----KLYHSTGLDDTDFIT Y FETD DLTA EN NLM LS LA QVK--EN KFH V R W G :	231			
DaCld :	-----KLYHSTGLDDTDFIT Y FETD DLTA EN NLM LS LA QVK--EN KFH V R W G :	232			
PcCld :	-----KLYHSTGLDDTDFIT Y FETD DLTA EN N V V LS LA QVK--EN KFH V R W G :	231			
IdCld :	-----KLYHSTGLDDTDFIT Y FETD DLGA EN NLM LS LA KVP--EN KYH V R W G :	241			
DgCld :	-----KLYHSTGLDDTDFIT Y FET ADLGA EN NLM L AL AKVP--EN KYH V R W G :	233			
BsT0T :	-----IITGSVGLDDFEWGVTLFSD DALQ KKLVYEMRFDE--VSARFGE F :	229			
Tt1485 :	-----VISGAQGLDDWEWGVDFSE D PV Q KKLVYEMRFDE--VSARYGE F :	230			
SoTyrA :	DENGK S IEILRQ S MP V G--S L KEQGLMFISTCRTPD H EKMLH S VMVFGD G AG HD HL M H F :	290			
PpMli :	-----SVE A LHDTLM Q L P LF P -----YM :	77			
BtDyP :	DD----LKIVRANMPFAN T SKGEYGY T Y F IGYAST F ST R RMLEN M FI G SPAG T DRLL D F :	295			

	230	240	%ID
AoCld :	SPTTL G TIHSP E DVIKALAD-- :	248	
DspCld :	SPTTL G TIHSP E DVIKALAD-- :	251	99
DaCld :	SPTTL G TIHSP E DVIKALAD-- :	252	98
PcCld :	SPTTL G TIHSP E DVIKAL E -- :	251	95
IdCld :	NPTV L GT I QPI E NLVK T LSM G N :	263	63
DgCld :	SPTV L GT I QSF D SVV N TLSM G R :	255	62
BsT0T :	-SFFV G IRL P ME N V S FF H V-- :	248	16
Tt1485 :	-PFFV G K Y L D E E AL R A F L G L-- :	249	12
SoTyrA :	TSALT S SS F F A PS L DF L M Q F D N :	312	12
PpMli :	DIEV D GLCR H PS S I H SD D R-- :	96	8
BtDyP :	STAIT G L L FF V PS Y DL L GE L GE :	317	8

Figure 4 (continued) sequences were predicted using SignalP⁴¹ and removed. BtDyp and SoTyrA are dye-decolorizing peroxidases from *Bacteroides thetaiotaomicron* and *Shewanella oneidensis*, respectively. Tt1485 is a hypothetical protein from *Thermus thermophilus* HB8 with remote homology to chlorite dismutase, suggested to function as a novel haem peroxidase. BsT0T is a putative Cld from *Bacillus stearothermophilus* with PDB entry 1t0t. PpMli is *Pseudomonas putida* muconolactone isomerase, a protein structurally similar to Tt1485. However, residues in the active sites of Tt1485 and PpMli are not conserved, implying that the proteins are not functionally related⁴². Residues conserved in the aligned sequences are shown white on black (100% identical), white on grey (70%) or black on grey (50%). The residues in AoCld directly involved in haem binding are marked with asterisks while those forming the haem cavity are boxed. Note that Trp155 is a conserved residue in all sequences which partakes in formation of the haem pocket. The column labeled with ID% represents overall percentage sequence identity to AoCld.

has been suggested to generate the EPR-active tryptophanyl radical appearing from a broad porphyrin π -cation radical signal in a Cld-chlorite

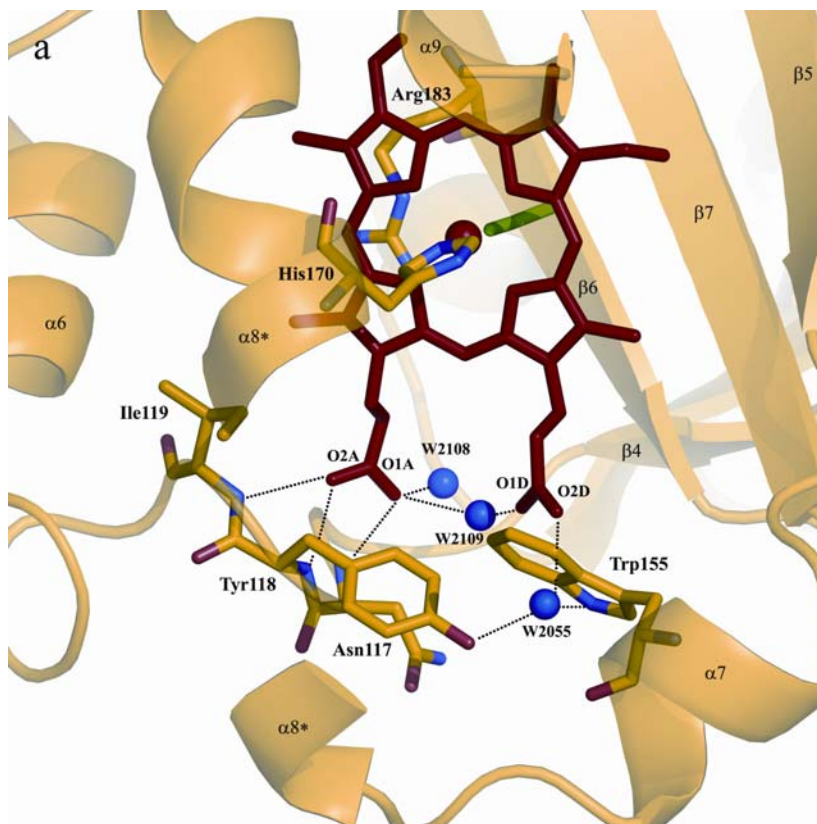


Figure 5 Metal binding site and possible hydrogen bonds **a)** The haem is presented in sticks and colored red, the coordinating His170 is colored yellow (carbon), blue (nitrogen) and red (oxygen). The same coloring is used for the amino acids Ile 119, Tyr118, Asn117, Arg183 and Trp155. The coordinating thiocyanate is colored green and the waters (W) are depicted as blue circles. For reasons of clarity a part of the helix $\alpha 8$ (between the asterisks) has been omitted from this drawing. The possible hydrogen bonds are presented as black dots. **b)** Active site superposition of cytochrome c peroxidase (pdb code 2cyp; labels and residues in grey) and Cld (2vxh; labels in black and residues in color) made with Superpose⁴³. The proximal His, the distal Arg and the Trp residues near the haem propionate group occupy comparable positions in the active sites of both enzymes.

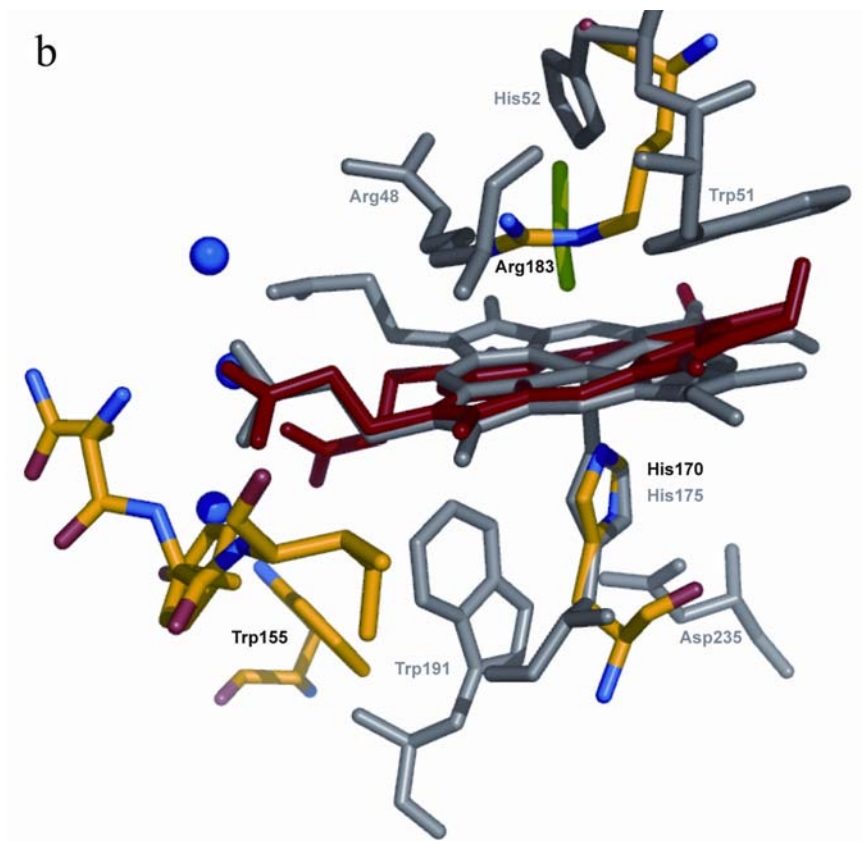


Figure 5 (legend on previous page)

mixture¹¹. Strikingly, in cytochrome c peroxidase a tryptophan residue is situated adjacent to the heme propionate like in Cld. Moreover, based on kinetic data Cld is predicted to share functional similarities with heme-dependent catalases and peroxidases¹⁰. A structural alignment of the active sites of cytochrome c peroxidase and Cld shows a conserved arginine (residue 183 in Cld) at a similar position in the distal heme pocket (Figure

5B). The presence of a positively charged side chain can promote charge separation in the transition state. In cytochrome c peroxidase the distal arginine has a key role in activating the substrate and its sidechain shifts toward the active site in the presence of an anionic ligand⁴⁴.

In Cld Arg183 is present in a rather striking conformation, at a distance of 6.5 Å from the iron atom. It seems to be displaced from the iron by the thiocyanate. Modelling indicates that in the absence of thiocyanate the Arg183 can approach the iron atom to a distance of 2.8 Å without changing the positions of main chain atoms. At a distance of 12 Å from the iron atom and 6.4 Å from Arg183, a hydrogen carbonate anion is located (Figure 3C; Figure S2), making a hydrogen bond (2.6 Å) with the backbone oxygen from Lys114. Inhibition studies on Cld have suggested the presence of a second, non-Fe coordinating site for ion binding in proximity of the heme, which would be necessary to accommodate the ClO⁻ until further recombination with Compound I¹⁰. The identification of the anion binding site in the Cld crystal structure, currently accommodating the hydrogen carbonate, points at a catalytic mechanism *via* ClO⁻ as proposed by Streit and DuBois¹⁰ and recently experimentally supported by Lee *et al.*¹¹.

5.3.4 Comparison with other structures

The sequence alignment shows that Cld is a highly conserved protein in perchlorate respiring bacteria. This high similarity is also observed when comparing the 31 residues of the haem-binding site of AoCld with its homologues. Except P115, Y177 (identities in 4/6 Cld sequences) and L211,

M212 (identities in 5/6 Cld sequences) all these residues are completely conserved in the 6 Cld sequences shown (Figure 4). No significant homology to any other enzyme could be found using BlastP on all non-redundant protein sequences in the NCBI database ⁴⁵. The highest percentage identity, excluding Cld homologues, was 23% with a ferrochelatase from *Propionibacterium acnes*. Ferrochelatase catalyzes the insertion of ferrous iron into protoporphyrin IX as the terminal step in haem biosynthesis. However, this protein has a 3-layer $\alpha\beta\alpha$ architecture with a chelatase-like fold (PDB code 1ak1) and did not show any similarity with AoCld using Superpose with secondary structure matching ⁴³. Structural alignment of AoCld and proteins in the Protein Data Bank using the Dali server ⁴⁶ revealed the highest similarity with two proteins of unknown function (1t0t and 1vdh) ⁴². The sequence identity for 1t0t and 1vdh compared to Cld is 16% and 12%, respectively. Both proteins were superposed onto Cld using Superpose with secondary structure matching (Figure 6). The main difference between the superposed structures is the orientation of the loop between β 4 and α 6, which is important for haem binding (Figure 5). This loop contains 3 of the 4 residues able to form hydrogen bonds with the two propionate groups of the haem. Both the protein structures of t0t and 1vdh were elucidated by X-ray crystallography, but both without haem present in the binding pocket. The putative Cld from *Bacillus stearothermophilus* with PDB entry 1t0t, present as a pentamer in the crystal, has not been described in literature. The protein from *Thermus thermophilus* HB8 (1vdh) was described as a pentameric complex in the crystal structure but reconstitution with haem did not result in significant

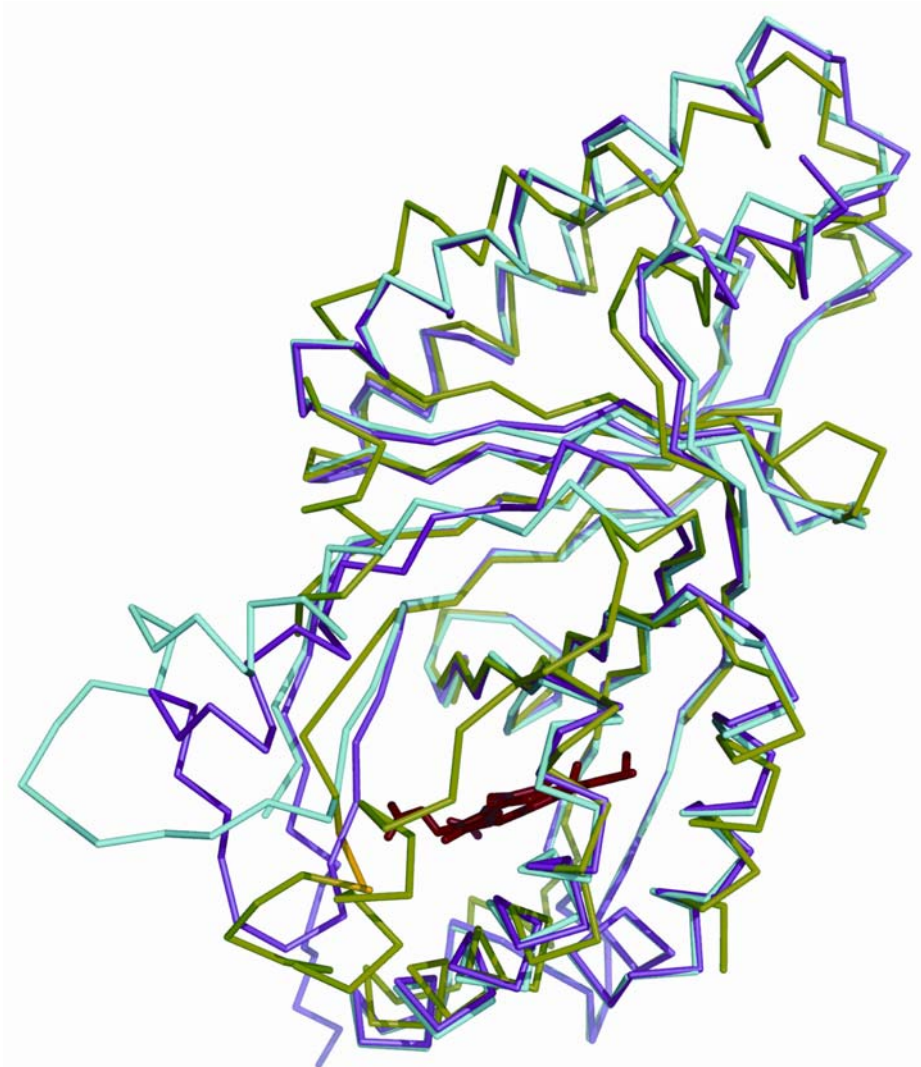


Figure 6 Comparison of AoCld with two structural relatives. Ca superpositions of AoCld, a putative Cld from *Bacillus stearothermophilus* (pdb code 1t0t) and a suggested haem peroxidase from *Thermus thermophilus* remotely homologous to Cld (1vdh) showing that these enzymes share major structural features. Cld (2vxh) is shown in green, the

putative Cld (1t0t) in blue and the suggested haem peroxidase (1vdh) in magenta. The haem, only present in Cld (2vxh), is colored red. The main difference between the superposed structures is the orientation of the loop between β 4 and α 6 (labelling according to Figure 3a), which is important for haem binding. The Cld residues Asn117, Tyr118, and Ile119 are shown in yellow. The superposition was done with Superpose⁴³ using secondary structure matching and the picture was prepared using PyMol²⁹.

Cld activity, indicating that 1vdh catalyzes a reaction other than Cld⁴². Although the haem incorporating AoCld monomeric fold we report here is similar to crystal structures previously linked with Cld activity, the quaternary state is different.

5.3.5 Redox properties of recombinant Cld

An EPR monitored redox titration of recombinant Cld showed the existence of three different haem species (Fig. 7A and 7B; Fig. S3). First, a high-spin species with g -values (6.29, 5.46, 1.99), similar to wild-type Cld⁹ and *I. dechloratans* Cld⁴⁷, which represents the five-coordinate ferric active form of the enzyme. Second, a low-spin species with g -values (2.97, 2.23, 1.49) similar to wild-type Cld with imidazole bound at the sixth coordination site. This species is most likely a remnant of the His-tag purification procedure. And finally, at relatively high potentials another low-spin species is observed, with g -values (2.90, 2.26, 1.55) which is indicative of a nitrogenous ligand at the sixth position. Presumably, this signal derives from a different protonation state of imidazole. In *I. dechloratans* Cld also a new low-spin ferric species was found in the heterologously expressed

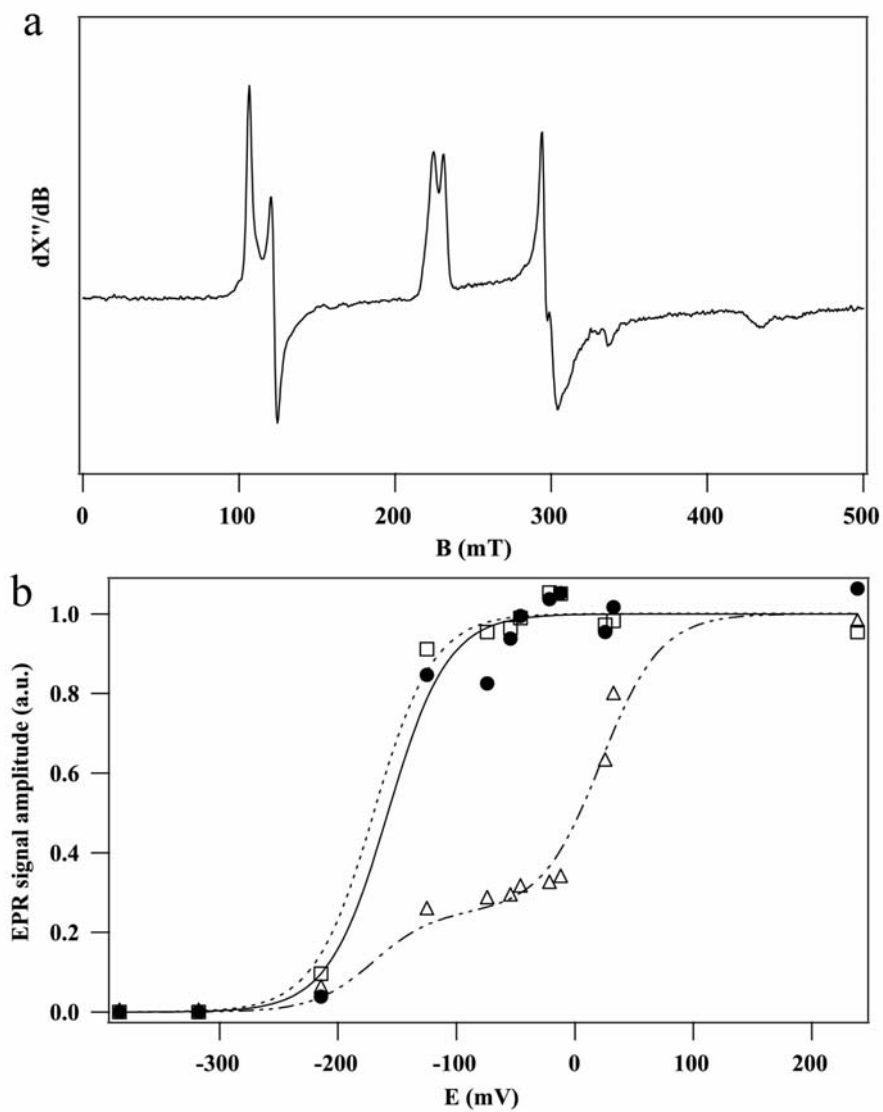


Figure 7 EPR spectroscopy and redox titration of Ao Cld. **a)** EPR spectrum of 0.18 mM Cld poised at +32 mV. EPR conditions: microwave frequency, 9.388 GHz; microwave

power, 126 mW; modulation amplitude, 2.0 mT; temperature, 17.5 K. **b)** Redox titration of Cld. ● five-coordinate haem, □ imidazole adduct, △ putative protonated imidazole bound enzyme. The datapoints are fitted to the Nernst equation for a one electron redox couple. Since the signal of the arginine bound enzyme contains a contribution of the imidazole bound enzyme, that signal is fitted to two independent one electron redox couples.

enzyme, with *g*-values (3.04, 2.25, 1.52). This species, not present in the wild-type enzyme, was attributed to bis-histidine coordinated haem⁴⁷.

The redox titration resulted in the following reduction potentials of the different haem species: -158 ± 9 mV for the five-coordinate Cld, -170 ± 6 mV for imidazole bound Cld, and $+22 \pm 6$ mV for the putative protonated imidazole bound Cld. The reduction potential for the recombinant Cld is 135 mV lower than for the wild-type enzyme⁹, which can be caused by subtle structural differences in the proximity of the haem. The reduction potential of haem iron in enzymes with a proximal histidine ligand is known to be modulated by the basicity of the proximal histidine⁴⁸. Furthermore, the wild-type enzyme, unlike the heterologously expressed enzyme, has been in contact with the highly oxidizing compounds (per)chlorate and chlorite during the cultivation of the organism. This has led to differences between native and recombinant versions of the same enzyme in some previous cases, notably also in *I. dechloratans* Cld⁴⁷. The low reduction potential of recombinant Cld results in a stabilization of the ferric state, which could be expected to be beneficial to its catalytic properties. However, the specific activity of the heterologously expressed Cld is similar to the wild-type enzyme⁹.

By using the relationship between the reduction potentials of the ligand bound and free enzyme the ratio of the K_d values of the ferric and ferrous forms of the enzyme for that ligand can be determined.

$$K_{d,red} = 10^{\frac{(E_{m,bound} - E_{m,free})nF}{2.303RT}} K_{d,ox}$$

From the E_m of the putative protonated imidazole bound form we calculate that the K_d of this ligand for ferrous iron is 150 times lower than for ferric iron. This indicates a clear preference of the protonated ligand for ferrous iron.

5.3.6 Cld catalytic mechanism

The stoichiometry of the Cld reaction is 1 mol Cl^- and 1 mol O_2 out of 1 mol ClO_2^- ⁸. Isotope experiments excluded water as a substrate of Cld, indicating that atoms in the oxygen gas product originate entirely from the ClO_2^- substrate⁴⁹.

The haem groups in two adjacent monomers are too far away from each other (Fe-Fe distance $\sim 31 \text{ \AA}$) to suggest electronic interactions between the Fe centers. Furthermore, recent kinetic experiments on recombinant Cld from *Dechloromonas aromatica* RCB, which is 98 % identical in amino acid sequence to AoCld, show exponential decay of the enzymatic activity with increasing ClO_2^- concentration¹⁰. Since cooperativity between the monomers in Cld would have led to a sigmoidal activity curve, this type of response to ClO_2^- binding could be ruled out. As a consequence, high valence states of the haem iron seem to be crucial for the transfer of the total

four electrons during one complete turnover, while the oxidation state of Cl in ClO_2^- changes from +3 to -1 in the Cl^- product.

Previous spectroscopic and ligand-binding studies of AoCld suggested binding of chlorite to the five coordinate high-spin ferric form of the enzyme (or hexacoordinate with a weak sixth ligand) as the first step of the catalytic mechanism. The accessibility of the ferric iron centers was shown using the substrate analog nitrite which produced a low-spin species upon binding to the ferric form of Cld ⁹. The current crystal structure confirms that all haem groups in the Cld molecule are solvent accessible, both from the outside and the inside of the protein ring.

Hagedoorn found optical and EPR spectroscopic evidence for the formation of a hydrogen peroxide Cld complex, which showed a decrease in the ferric signal and appearance of a radical signal in the EPR spectrum ⁹. Based on these results and the necessity of high valence states of the haem cofactor, we assumed the oxidation of the ferric iron center to an intermediate oxoferryl complex ($\text{Fe}^{\text{IV}}=\text{O}$) like compound I or II ⁵⁰. George ⁵¹ discovered that ClO^- and ClO_2^- were able to form compound I and II in the haem enzyme horseradish peroxidase. Very recently, both compound I and a compound II-associated tryptophanyl radical signal have indeed been observed using EPR on a freeze-quenched Cld sample containing its substrate chlorite ¹¹.

The positively charged guanidinium group at the distal haem site makes Arg183 an ideal candidate to align and activate the ClO_2^- in the active site before oxidation. The ClO^- then released needs to be captured and stabilized by an amino acid nucleophile, presumably a nitrogen or oxygen atom. The

backbone oxygen of the strictly conserved Lys114, which is part of the anion binding site, is positioned near the haem edge and might fulfill this function. A mode of recombining the oxygen atoms of Compound I and ClO^- to give the reaction products has been proposed to occur *via* a peroxyhypochlorite intermediate. A nucleophilic attack of ClO^- onto the electrophilic compound I oxygen could produce this intermediate species before recombination to molecular oxygen, Cl^- and concomitant return to the ferric starting state of Cld¹¹.

5.4 Conclusion

Cld is a haem-based enzyme that selectively and effectively detoxifies chlorite with concomitant O-O bond formation. The removal of the by-product chlorite is essential for survival of perchlorate and chlorate respiring bacteria. Cld from different sources has been described as a tetramer in its native state. However, in our crystal we observed a hexameric Cld ring. Based on the size of the solvent-accessible surface area buried after interaction between the six monomers, the hexamer was classified as a possible quaternary biological assembly. Re-interpreting our chromatographic data we found that based on the experimentally determined elution position, Cld could also be a pentameric or hexameric ring. Native mass spectrometry using a multimeric sample with high enzymatic activity demonstrated the presence of a molecular weight corresponding to a Cld pentamer. Taken all these data together, we conclude that the pentamer is an active state of Cld in solution. We cannot exclude the hexamer to be another

biologically relevant quaternary state although it was impossible to measure its activity due to the presence of the thiocyanate inhibitor. However, since cooperativity between the Cld monomers has been excluded based on kinetics results, indicating the monomers independently catalyse chlorite reduction, the precise quaternary state of the enzyme may be less relevant for enzymatic activity. In this case, different quaternary states might be biologically relevant and enzymatically active. For example, there may be an equilibrium between two states, with a transition influenced by protein concentration, pH or a small molecule or an ion^{52;53}.

The crystal structure of the inhibited, haem incorporated Cld presented here, gives the first insights into the active site of the O-O bond formation and points at some key residues. A strictly conserved histidine (His170) is the axial haem ligand, while a strictly conserved arginine residue (Arg183) occupies a similar position in the distal part of the active site as Arg48 in cytochrome c peroxidase. Arg183 most likely has an essential role in substrate positioning and activation, as the homologous arginine residue in cytochrome c peroxidase. Trp155, another strictly conserved residue in Cld has been identified on geometrical grounds as the electron donor for the reduction of compound I to compound II. Trp155 is also part of the hydrogen bond network that binds the haem cofactor.

The identification of an anion binding site near the haem is an important finding for the interpretation of the catalytic mechanism. The assumed mechanism involving a compound I intermediate would also generate a ClO⁻ anion which must remain close to the active site to perform its nucleophilic attack on the oxy-iron species.

On the basis of the EPR monitored redox titration, the reduction potential for the recombinant Cld haem appeared 135 mV lower than for the wild-type enzyme. However, this does not result in a higher specific activity, as could be expected from the stabilization of the ferric state.

To conclude, our data support the proposed catalytic mechanism for O-O bond formation *via* high valent oxy-iron species and ClO^- . Furthermore, we have analyzed the active site of Cld and indicated some key residues for chlorite conversion. Our work demonstrates that a unique biological function, chlorite detoxification, has led to a unique haem enzyme.

A combination of site directed mutagenesis with spectroscopical and structural approaches is now necessary to complement the current catalytic mechanism. Pre-steady state kinetics experiments should be performed to study the formation of the Cld- ClO_2^- intermediates.

Coordinates

Coordinates and structure factors have been deposited in the Protein Data Bank (accession code 2vxh).

Acknowledgements

We thank Dr Ir Bert Jansen for data collection and Dr R.A.G. de Graaff for helpful discussions. We are grateful to Dr David Flot and other members of the EMBL-ESRF Joint Structural Biology Group for providing crystallographic data collection facilities and help therewith.

Supplementary data

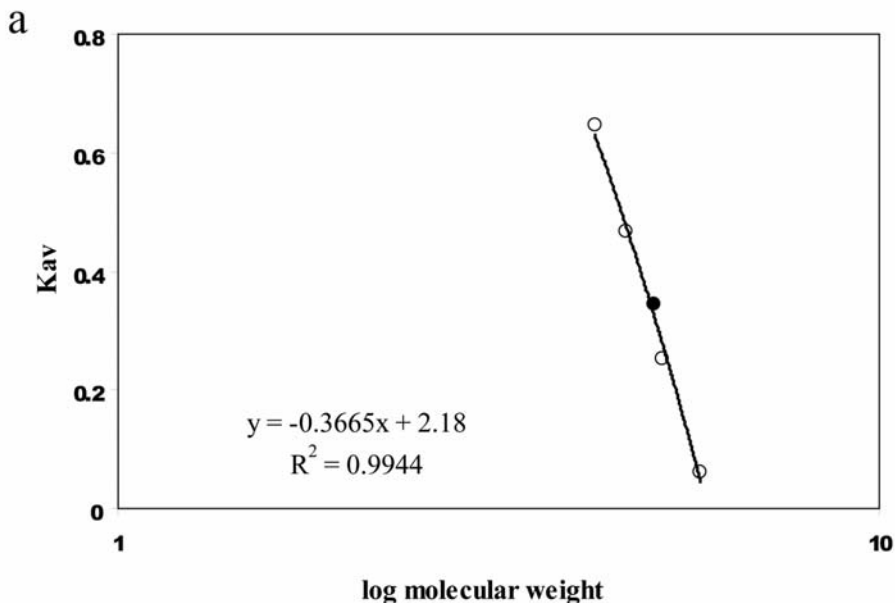


Figure S1. Determination of the quaternary state. Calibration curves created with size exclusion chromatography on a Superdex column. Data for molecular weights standards elution (open circles) have been fitted to the equations shown.

a) The chromatographically determined K_{av} for Cld (closed circle) together with the calibration equation $y = -0.3665x + 2.18$ suggests a molecular weight of 105 kD which if one assumes a globular shape, would correlate with a tetrameric state of Cld in solution. **b)** The apparent molecular radius of 43 Å as calculated from the equation $y = 0.0098x + 0.2596$ agrees very well with the value of 44 Å (closed circle) estimated from the crystal structure of the hexameric Cld ring (right inset) using Crysol software⁵⁴. For completeness, a pentameric Cld constructed by superposing Cld subunits onto the putative Cld pentamer 1t0t is also shown (closed triangle; left inset). The ring structures of Cld therefore elute at a V_e that would also correspond to a globular tetramer in solution.

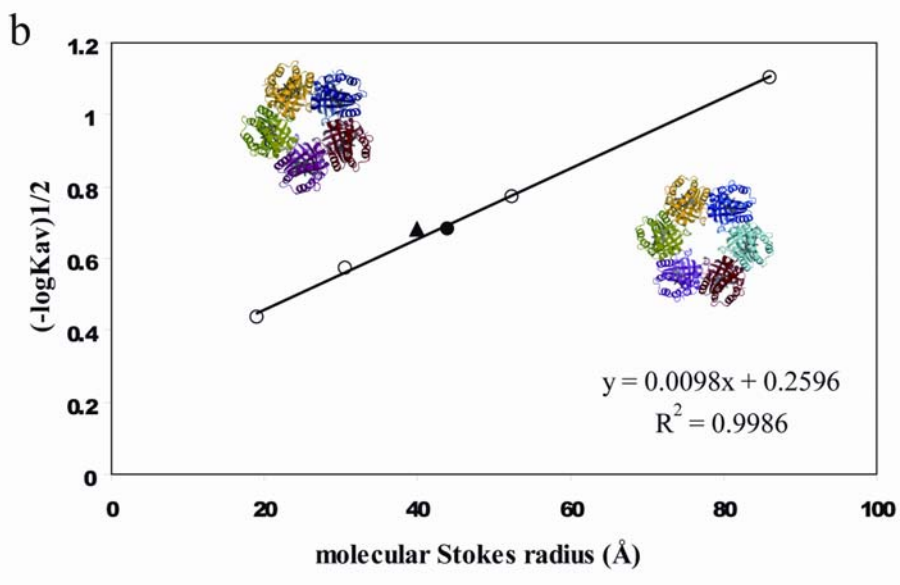


Figure S1. (legend on previous page)

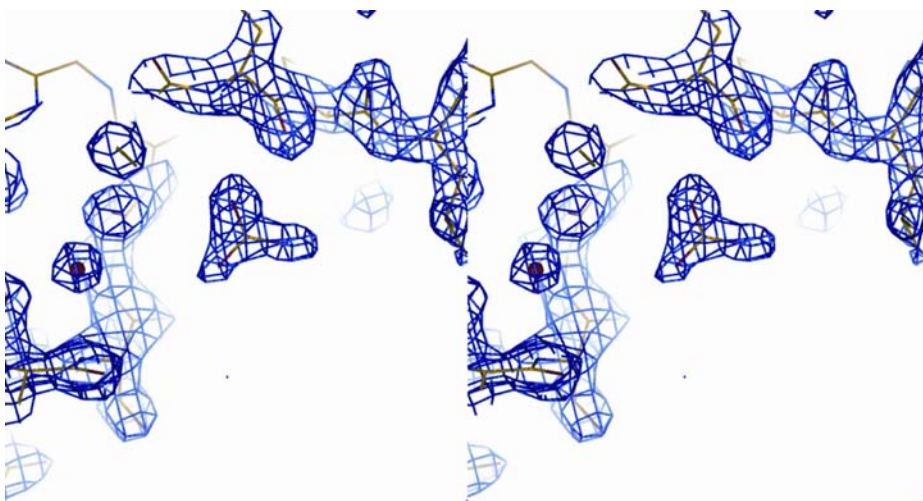


Figure S2. Stereo representation of the anion binding site. Portion of the final 2.1 Å ($2F_o - F_c$) electron density map centered on the anion binding site, which is occupied by HCO_3^- , contoured at the 1.0σ level.

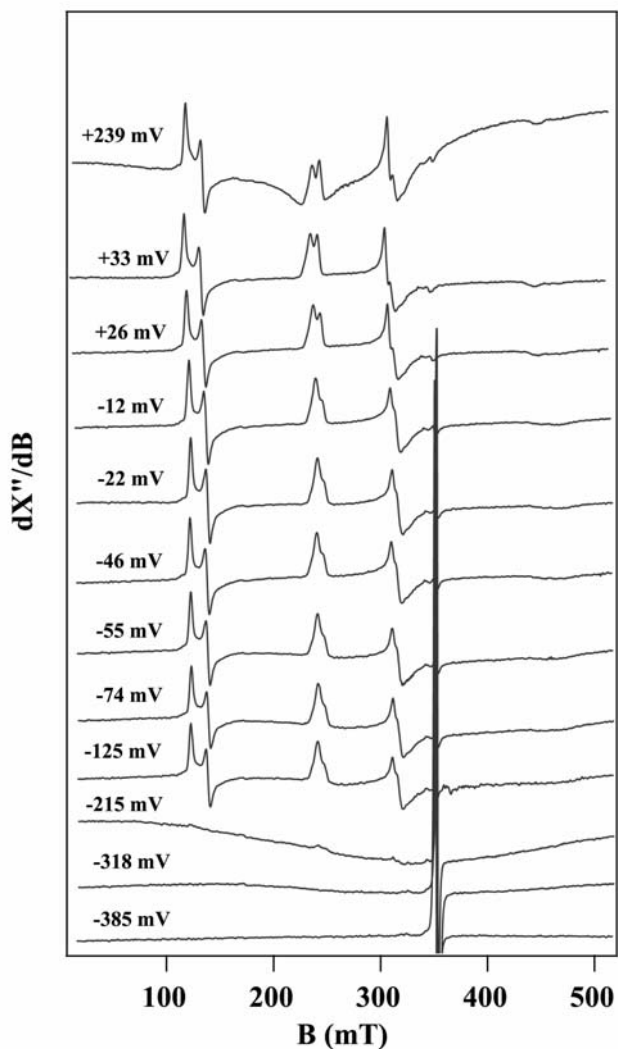


Figure S3. EPR spectra of the samples of the redox titration of Ao Cld. EPR conditions: microwave frequency, 9.388 GHz; microwave power, 126 mW; modulation amplitude, 2.0 mT; temperature, 17.5 K.

References

1. Urbansky, E.T. (2002). Perchlorate as an environmental contaminant. *Environ. Sci. Pollut. Res. Int.* **9**, 187-192.
2. Loomis, W.E., Bissey, R., & Smith, E.V. (1931). Chlorates as herbicides. *Science* **74**, 485.
3. Smith, E.A. & Oehme, F.W. (1991). A review of selected herbicides and their toxicities. *Vet. Hum. Toxicol.* **33**, 596-608.
4. EPA 816-F-03-016. available for download at <http://www.epa.gov/safewater/consumer/pdf/mcl.pdf>. 2003.
5. Rikken, G.B., Kroon, A.G.M., & vanGinkel, C.G. (1996). Transformation of (per)chlorate into chloride by a newly isolated bacterium: Reduction and dismutation. *Applied Microbiology and Biotechnology* **45**, 420-426.
6. Wolterink, A., Kim, S., Muusse, M., Kim, I.S., Roholl, P.J., van Ginkel, C.G., Stams, A.J., & Kengen, S.W. (2005). Dechloromonas hortensis sp. nov. and strain ASK-1, two novel (per)chlorate-reducing bacteria, and taxonomic description of strain GR-1. *Int. J. Syst. Evol. Microbiol.* **55**, 2063-2068.
7. Kengen, S.W., Rikken, G.B., Hagen, W.R., van Ginkel, C.G., & Stams, A.J. (1999). Purification and characterization of (per)chlorate reductase from the chlorate-respiring strain GR-1. *J. Bacteriol.* **181**, 6706-6711.
8. van Ginkel, C.G., Rikken, G.B., Kroon, A.G., & Kengen, S.W. (1996). Purification and characterization of chlorite dismutase: a novel oxygen-generating enzyme. *Arch. Microbiol.* **166**, 321-326.
9. Hagedoorn, P.L., De Geus, D.C., & Hagen, W.R. (2002). Spectroscopic characterization and ligand-binding properties of chlorite dismutase from the chlorate respiring bacterial strain GR-1. *Eur. J. Biochem.* **269**, 4905-4911.
10. Streit, B.R. & DuBois, J.L. (2008). Chemical and steady-state kinetic analyses of a heterologously expressed heme dependent chlorite dismutase. *Biochemistry* **47**, 5271-5280.
11. Lee, A.Q., Streit, B.R., Zdilla, M.J., Abu-Omar, M.M., & DuBois, J.L. (2008). Mechanism of and exquisite selectivity for O-O bond formation by the heme-dependent chlorite dismutase. *Proc. Natl. Acad. Sci. U. S. A* **105**, 15654-15659.

12. De Geus, D.C., Thomassen, E.A., van der Feltz, C.L., & Abrahams, J.P. (2008). Cloning, expression, purification, crystallization and preliminary X-ray diffraction analysis of chlorite dismutase: a detoxifying enzyme producing molecular oxygen. *Acta Crystallogr. Sect. F. Struct. Biol. Cryst. Commun.* **64**, 730-732.
13. Crawford, A.W. & Beckerle, M.C. (1991). Purification and characterization of zyxin, an 82,000-dalton component of adherens junctions. *J. Biol. Chem.* **266**, 5847-5853.
14. Alazard, R., Mourey, L., Ebel, C., Konarev, P.V., Petoukhov, M.V., Svergun, D.I., & Erard, M. (2007). Fine-tuning of intrinsic N-Oct-3 POU domain allostery by regulatory DNA targets. *Nucleic Acids Res.* **35**, 4420-4432.
15. Tahallah, N., Pinkse, M., Maier, C.S., & Heck, A.J. (2001). The effect of the source pressure on the abundance of ions of noncovalent protein assemblies in an electrospray ionization orthogonal time-of-flight instrument. *Rapid Commun. Mass Spectrom.* **15**, 596-601.
16. Pouvreau, L.A., Strampraad, M.J., Van Berloo, S., Kattenberg, J.H., & de Vries, S. (2008). NO, N₂O, and O₂ reaction kinetics: scope and limitations of the Clark electrode. *Methods Enzymol.* **436**, 97-112.
17. Pierik, A.J., Hagen, W.R., Dunham, W.R., & Sands, R.H. (1992). Multi-frequency EPR and high-resolution Mossbauer spectroscopy of a putative [6Fe-6S] prismatic-cluster-containing protein from *Desulfovibrio vulgaris* (Hildenborough). Characterization of a supercluster and superspin model protein. *Eur. J. Biochem.* **206**, 705-719.
18. Leslie, A.G. (1999). Integration of macromolecular diffraction data. *Acta Crystallogr. D. Biol. Crystallogr.* **55**, 1696-1702.
19. Evans, P. (2006). Scaling and assessment of data quality. *Acta Crystallogr. D. Biol. Crystallogr.* **62**, 72-82.
20. Collaborative Computational Project Number 4 (1994). The CCP4 suite: programs for protein crystallography. *Acta Crystallogr. D. Biol. Crystallogr.* **50**, 760-763.
21. Ness, S.R., de Graaff, R.A., Abrahams, J.P., & Pannu, N.S. (2004). CRANK: new methods for automated macromolecular crystal structure solution. *Structure.* **12**, 1753-1761.
22. de Graaff, R.A., Hilge, M., van der Plas, J.L., & Abrahams, J.P. (2001). Matrix methods for solving protein substructures of chlorine and sulfur from anomalous data. *Acta Crystallogr. D. Biol. Crystallogr.* **57**, 1857-1862.

23. Pannu, N.S., McCoy, A.J., & Read, R.J. (2003). Application of the complex multivariate normal distribution to crystallographic methods with insights into multiple isomorphous replacement phasing. *Acta Crystallogr. D. Biol. Crystallogr.* **59**, 1801-1808.
24. Abrahams, J.P. & Leslie, A.G. (1996). Methods used in the structure determination of bovine mitochondrial F1 ATPase. *Acta Crystallogr. D. Biol. Crystallogr.* **52**, 30-42.
25. Cowtan, K. (2006). The Buccaneer software for automated model building. 1. Tracing protein chains. *Acta Crystallogr. D. Biol. Crystallogr.* **62**, 1002-1011.
26. Murshudov, G.N., Vagin, A.A., & Dodson, E.J. (1997). Refinement of macromolecular structures by the maximum-likelihood method. *Acta Crystallogr. D. Biol. Crystallogr.* **53**, 240-255.
27. Pannu, N.S., Murshudov, G.N., Dodson, E.J., & Read, R.J. (1998). Incorporation of prior phase information strengthens maximum-likelihood structure refinement. *Acta Crystallogr. D. Biol. Crystallogr.* **54**, 1285-1294.
28. Emsley, P. & Cowtan, K. (2004). Coot: model-building tools for molecular graphics. *Acta Crystallogr. D. Biol. Crystallogr.* **60**, 2126-2132.
29. DeLano, W.L. (2002). The PyMOL Molecular Graphics System.
<http://pymol.sourceforge.net/>.
30. Laskowski, R.A., MacArthur, M.W., Moss, D.S., & Thornton, J.M. (1993). PROCHECK: a program to check the stereochemical quality of protein structures. *J. Appl. Cryst.* **26**, 283-291.
31. Henrick, K. & Thornton, J.M. (1998). PQS: a protein quaternary structure file server. *Trends Biochem. Sci.* **23**, 358-361.
32. Stenklo, K., Thorell, H.D., Bergius, H., Aasa, R., & Nilsson, T. (2001). Chlorite dismutase from *Ideonella dechloratans*. *J. Biol. Inorg. Chem.* **6**, 601-607.
33. Bender, K.S., O'Connor, S.M., Chakraborty, R., Coates, J.D., & Achenbach, L.A. (2002). Sequencing and transcriptional analysis of the chlorite dismutase gene of *Dechloromonas agitata* and its use as a metabolic probe. *Appl. Environ. Microbiol.* **68**, 4820-4826.
34. Siegel, L.M. & Monty, K.J. (1966). Determination of molecular weights and frictional ratios of proteins in impure systems by use of gel filtration and density

- gradient centrifugation. Application to crude preparations of sulfite and hydroxylamine reductases. *Biochim. Biophys. Acta* **112**, 346-362.
35. Caldinelli, L., Molla, G., Pilone, M.S., & Pollegioni, L. (2006). Tryptophan 243 affects interprotein contacts, cofactor binding and stability in D-amino acid oxidase from *Rhodotorula gracilis*. *FEBS J.* **273**, 504-512.
 36. Pollegioni, L., Iametti, S., Fessas, D., Caldinelli, L., Piubelli, L., Barbiroli, A., Pilone, M.S., & Bonomi, F. (2003). Contribution of the dimeric state to the thermal stability of the flavoprotein D-amino acid oxidase. *Protein Sci.* **12**, 1018-1029.
 37. Bond, C.S. (2003). TopDraw: a sketchpad for protein structure topology cartoons. *Bioinformatics.* **19**, 311-312.
 38. Zhang, C. & Kim, S.H. (2000). The anatomy of protein beta-sheet topology. *J. Mol. Biol.* **299**, 1075-1089.
 39. Larkin, M.A., Blackshields, G., Brown, N.P., Chenna, R., McGettigan, P.A., McWilliam, H., Valentin, F., Wallace, I.M., Wilm, A., Lopez, R., Thompson, J.D., Gibson, T.J., & Higgins, D.G. (2007). Clustal W and Clustal X version 2.0. *Bioinformatics.* **23**, 2947-2948.
 40. Nicholas, K.B., Nicholas, H.B.Jr., & Deerfield, D.W.I. (1997). GeneDoc: Analysis and Visualization of Genetic Variation. *EMBNEW. NEWS* **4**, 14.
 41. Bendtsen, J.D., Nielsen, H., von Heijne, G., & Brunak, S. (2004). Improved prediction of signal peptides: SignalP 3.0. *J. Mol. Biol.* **340**, 783-795.
 42. Ebihara, A., Okamoto, A., Kousumi, Y., Yamamoto, H., Masui, R., Ueyama, N., Yokoyama, S., & Kuramitsu, S. (2005). Structure-based functional identification of a novel heme-binding protein from *Thermus thermophilus* HB8. *J. Struct. Funct. Genomics* **6**, 21-32.
 43. Krissinel, E. & Henrick, K. (2004). Secondary-structure matching (SSM), a new tool for fast protein structure alignment in three dimensions. *Acta Crystallogr. D. Biol. Crystallogr.* **60**, 2256-2268.
 44. Finzel, B.C., Poulos, T.L., & Kraut, J. (1984). Crystal structure of yeast cytochrome c peroxidase refined at 1.7-Å resolution. *J. Biol. Chem.* **259**, 13027-13036.
 45. Altschul, S.F., Madden, T.L., Schaffer, A.A., Zhang, J., Zhang, Z., Miller, W., & Lipman, D.J. (1997). Gapped BLAST and PSI-BLAST: a new generation of protein database search programs. *Nucleic Acids Res.* **25**, 3389-3402.

46. Holm, L. & Sander, C. (1996). Mapping the protein universe. *Science* **273**, 595-603.
47. Danielsson, T.H., Beyer, N.H., Heegaard, N.H., Ohman, M., & Nilsson, T. (2004). Comparison of native and recombinant chlorite dismutase from *Ideonella dechloratans*. *Eur. J. Biochem.* **271**, 3539-3546.
48. Banci, L., Bertini, I., Turano, P., Tien, M., & Kirk, T.K. (1991). Proton NMR investigation into the basis for the relatively high redox potential of lignin peroxidase. *Proc. Natl. Acad. Sci. U. S. A* **88**, 6956-6960.
49. Wolterink, A. F. W. M. Characterization of (per)chlorate-reducing bacteria. Thesis Wageningen University . 2004.
50. Dolphin, D., Forman, A., Borg, D.C., Fajer, J., & Felton, R.H. (1971). Compounds I of catalase and horse radish peroxidase: pi-cation radicals. *Proc. Natl. Acad. Sci. U. S. A* **68**, 614-618.
51. George, P. (1953). Intermediate compound formation with peroxidase and strong oxidizing agents. *J. Biol. Chem.* **201**, 413-426.
52. Cabezón, E., Butler, P.J., Runswick, M.J., & Walker, J.E. (2000). Modulation of the oligomerization state of the bovine F1-ATPase inhibitor protein, IF1, by pH. *J. Biol. Chem.* **275**, 25460-25464.
53. Cabezón, E., Butler, P.J., Runswick, M.J., Carbajo, R.J., & Walker, J.E. (2002). Homologous and heterologous inhibitory effects of ATPase inhibitor proteins on F-ATPases. *J. Biol. Chem.* **277**, 41334-41341.
54. Svergun, D., Barberato, C., & Koch M.H.J. (1995). CRY SOL - a Program to Evaluate X-ray Solution Scattering of Biological Macromolecules from Atomic Coordinates. *Journal of Applied Crystallography* **28**, 768-773.

Chapter

6

Structural insight into the microtubule End Binding protein EB1 by small angle X-ray scattering: orientation of the microtubule binding and the coiled coil interacting domains.

Abstract

The end-binding protein 1 (EB1) is the archetypal member of a highly conserved group of proteins that uses its localization at the plus-ends of microtubules to regulate microtubule dynamics and chromosome segregation. EB1 contains an amino-terminal microtubule binding domain (*En*) and a carboxy-terminal dimerization domain (*Ec*). The latter domain can bind the p150Glued subunit of dynactin and the tumour suppressor protein APC. The crystal structures of both domains are known, but their relative orientation and the structure of the aminoacid sequence linking both domains is not. We used analytical ultracentrifugation, gel filtration and small-angle x-ray solution scattering experiments to show that full length EB1 is a non-globular dimer. In addition, the SAXS data provided a low resolution contour of the EB1 dimer as it exists in solution. We enhanced the resolution of this reconstruction by including the known crystal structures of the N- and C-terminal domains. A consistent picture emerges, whether or not the symmetry of the EB1 dimer is constrained. Essentially, the structure has the shape of a capital T, with the coiled-coil forming the stem of the T and the globular domains the cross. The two peptides linking the N-terminal to C-terminal domains generally lie in the plane of the T. The SAXS data do not provide sufficient resolution to distinguish the direction of the coiled coils, nor the orientation of the globular domains within the dimer. Nevertheless, the distance between the centers of gravity of the globular domains is about 80 to 90 Å. This is close to the distance between adjacent tubulin subunits along a microtubule

protofilament, thus suggesting a potential mode of binding of EB1 to the microtubule plus end.

6.1 Introduction

One of the prime regulators of microtubule dynamics is EB1. This end-binding protein localizes specifically to the plus ends of microtubules (MTs). MTs, the tubular assembled form of tubulin heterodimers, mediate many essential processes in all eukaryotic cells, *e.g.* chromosome segregation. An important feature of the MT is its ability to assemble and disassemble from both sides: fast at the plus end and slow at the minus end. To assemble, the tubulin dimer needs to have bound GTP in the β -subunit, which is hydrolysed shortly after the dimer is incorporated in the MT. The kinetics and conformation of tubulin are different for the GDP- and GTP-forms: while GDP-tubulin dimers are bent and prone to depolymerise in the MT, the GTP bound state is straight and promotes polymerisation. Since tubulin adds to the MT plus-end as GTP-tubulin, a cap is formed that protects the MT from depolymerization. The tendency of GDP-tubulin to bend is constrained when incorporated in the MT by interactions with its neighbouring dimers, which implies that the energy of the GTP hydrolysis is stored in the MT lattice¹⁻⁵. The standard free energy for hydrolysis of a MT-bound nucleotide triphosphate is near-zero and the lattice stored energy is available to do work, as in chromosome movement⁴. When MTs disassemble, the lattice strain is rapidly released by the curling out of

protofilaments^{6,7}. Alternating periods of growth and shrinking of the MTs result in the characteristic process referred to as dynamic instability.

Antimitotic drugs interacting with tubulin disrupt the normal MT behaviour. Colchicine and vinblastine inhibit polymerization, while taxol prevents depolymerization of the MTs. Furthermore in the living cell MT dynamics is regulated by transcription of different tubulin isotypes, folding of α/β -tubulin heterodimers, post-translational modification of tubulin, the nucleotide availability as well as the interaction with microtubule-associated proteins (MAPS)⁸. The MAPs including the motor proteins dynein and kinesin have been extensively researched for the last 20 years (see for exhaustive reviews Refs 8-11). A subset of the MAPS, the plus-end-tracking-proteins or +TIPs accumulate specifically at the MT growing end and regulate MT dynamics. While EB1 is considered to be the prime +TIP, many interactions exist between EB1 and other proteins, suggesting it plays a central role in the regulation of the dynamic instability. This topic has been thoroughly reviewed (see *e.g.* Ref. 12). The fission yeast EB1 homolog Mal3p preferentially binds into specific sites that only form at the MT lattice seam. It has been suggested that more of these binding sites could be exposed at the growing plus-ends if the protofilaments are not yet laterally attached¹³, explaining the plus-end tracking behaviour of EB proteins. More recent sheet formation and closure by EB1 itself has been observed using electron cryomicroscopy¹⁴.

Insight into the functioning of MTs is essential to understand the defects occurring in diseased cells. The aim of the work described in this chapter

was to structurally characterize EB1 and the complex EB1•p150GluedN to shed light on the mechanism of MT dynamics regulation.

6.2 Experimental procedures

6.2.1 Preparation of proteins and complexes

Bovine liver catalase and horse muscle myoglobin were purchased from Sigma (Zwijndrecht, NL).

Murine EB1 (residues 1-268) with His₆-tag was expressed using a pET28a vector (Novagen, Germany) in the *Escherichia coli* host strain Rosetta BL21(DE3) pLysS. The vectors used for this research were kindly provided by Niels Galjart (Erasmus Medical Center, Rotterdam). Bacteria were grown at 37°C in LB medium containing 50 mg/l kanamycin and 25 mg/l chloramphenicol and the cultures were induced at OD₆₀₀ = 0.4 by adding IPTG to 1mM and incubated at 37°C for 3 h. Cells were lysed in PBS buffer containing 1% Triton-X-100, by three times freezing in liquid nitrogen, followed by melting in a room temperature water bath, and sonication on ice. EB1 was pulled out of solution with a HisTrap HP column (GE Healthcare, Netherlands). After elution with Tris buffer containing 200 mM imidazole (pH 7.5), CaCl₂ was added to 5 mM concentration and the His-tag cleaved off by thrombin (Roche, Germany) The protein was loaded onto a Q-Source column equilibrated with 20 mM Tris (pH 7.5) and eluted with 20 mM Tris, 1 M NaCl (pH 7.5).

The protein was further purified by size exclusion chromatography with HiLoad 16/60 Superdex 200 prep grade using 20 mM Tris (pH 7.5) containing 150 mM NaCl and 1 mM DTT. The column (which had been calibrated beforehand with gelfiltration standards from Biorad) was eluted at 1 ml/min. All purification steps were performed at 4°C. EB1 was concentrated using Microcon concentrators (10 kD MWCO) and after snap-freezing in liquid nitrogen, the samples were stored at -80°C until use.

The N-terminal domain of rat p150Glued (residues 1-207 containing the CAP-Gly domain and an adjacent serine-rich domain) was purified in a similar way with the exception that an S-Source replaced the Q-Source column. The complex EB1•p150GluedN was prepared by adding purified p150GluedN to EB1 in a molar ratio 2:1, incubating the mixture on ice for ten minutes and running the sample on the equilibrated size exclusion column as described above. The identity and purity of the proteins and complex were routinely checked on Coomassie stained SDS PAGE gels and analysed with sedimentation velocity measurements.

6.2.2 Sample preparation

Catalase and myoglobin were dissolved at 20 mg/ml in 20 mM phosphate buffer containing 100 mM NaCl (pH 7.0). These solutions were dialyzed against the same buffer to remove traces of heavy metals. All protein solutions were filtered through an Ultrafree 0.22 µm filter unit (Millipore, USA) before the SAXS measurements.

6.2.3 Analytical ultracentrifugation

Sedimentation velocity experiments were performed using Optima XL-A and XL-I analytical centrifuges (Beckman-Coulter, Palo Alto, CA). The XL-A ultracentrifuge was equipped with a UV-visible absorbance detection system, while the XL-I had integrated absorbance and interference optics. The interference optics detected protein through changes in refractive index. The latter detection system allows a greater concentration range of macromolecules and larger data sets can be measured and analysed¹⁵. The sedimentation coefficient distributions were determined by direct linear least-squares boundary fitting using Sedfit¹⁶. All experimental s -values were corrected to the standard state of water at 20°C, which is necessary for comparative purposes of data obtained under different experimental conditions. The corrected $s_{20,w}$ values were calculated with the public domain software Sednterp (<http://www.rasmb.bbri.org>).

6.2.4 SAXS data acquisition

Small angle X-ray scattering measurements were conducted at the ESRF DUBBLE beam line BM26B (Grenoble, France) using 10 keV X-rays. Scattered X-rays were collected with a gas filled 2D Multiwire Proportional Counter positioned at a distance of 2 meters from the sample, covering the wave vector range $0.0008 < Q < 0.008 \text{ \AA}^{-1}$. Absolute values of the wave vector were obtained by reference to the orders of the 58.4 Å diffraction peak repeat in silver behenate¹⁷. The amplitude of the wave vector is defined

as $Q = (4\pi/\lambda)\sin(\theta)$, 2θ being the scattering angle. The cell, which contained approximately 100 μl of sample between mica windows, was translated in a continuous movement during exposure to reduce radiation damage by the intense X-ray beam. Judging from the stability of intensity over time, the proteins suffered negligible radiation damage during a typical data collection of 60 frames of 10 s exposure each. All experiments were performed at room temperature.

6.2.5 SAXS data treatment

The SAXS data were processed using OTOKO¹⁸. The 2D images were reduced to scattering profiles by sector integration. Subsequently, these 1D curves were corrected for the beam intensity and the detector response. After averaging the buffer contribution was subtracted from each corrected scattering profiles using a published procedure¹⁹. The pair distribution function $p(r)$, the forward scattering $I(0)$ and the radius of gyration R_g were calculated using the program GNOM²⁰.

6.3 Results and Discussion

6.3.1 EB1 and EB1•p150GluedN purification

SDS-PAGE of EB1 purified by affinity, ion exchange and size exclusion chromatography indicated that the protein was >95% pure (Figure 1). The crystal structure of the coiled coil domain of EB1 (PDB code 1WU9) is a dimer²¹. However, the elution volume of EB1 during the final purification

step was smaller than expected for a globular dimer implying that either the native state of full length EB1 is larger than a dimer or that the EB1 particle is non-globular (Figure 2). The fractions containing EB1 were pooled and concentrated to 12 mg ml^{-1} for further analysis.

The fragment p150GluedN eluted as a monomer during the final purification step and was concentrated to 23 mg ml^{-1} . The complex EB1•p150GluedN was concentrated to 12.5 mg ml^{-1} .

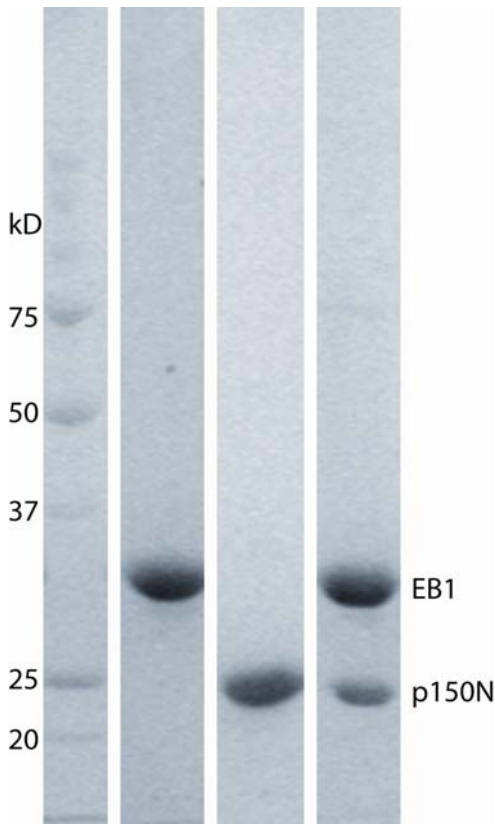


Figure 1 SDS PAGE gel of samples after final gel filtration purification step. From left to right: marker proteins, full length EB1, p150GluedN fragment and the EB1•p150GluedN complex are shown

6.3.2 Shape of EB1 from hydrodynamic data

In a sedimentation velocity experiment a concentration boundary of macromolecules is formed that moves towards the end of the centrifuge cell as a function of time. The goal of the experiment is to determine the

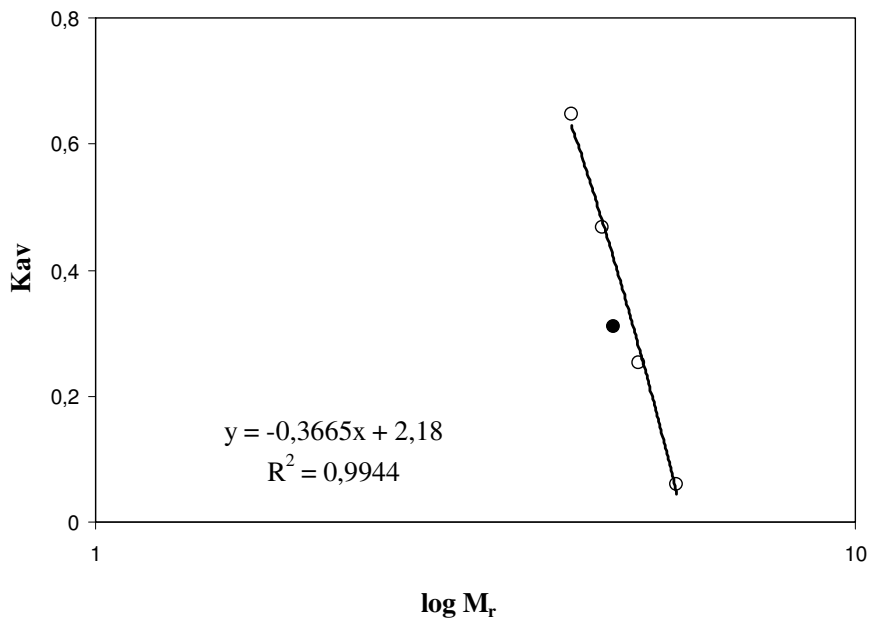


Figure 2 Gel filtration of marker proteins (open circles) and EB1 (closed circle) on Superdex 200. Further details about the method are described in chapter 5

sedimentation coefficient or s -value of the macromolecule (Table 1), defined by the Svedberg equation¹⁵:

$$s = \frac{u}{\omega^2 r} = \frac{M(1 - \bar{v}\rho)}{N_A f} = \frac{MD(1 - \bar{v}\rho)}{RT}$$

with u the observed radial velocity of the macromolecule, ω the angular velocity of the rotor, r the radial position, $\omega^2 r$ the centrifugal field, M the molar mass, \bar{v} the partial specific volume, ρ the density of the solvent, N_A

Table I Experimentally determined s -values after correction to water at 20°C

Sample	M_r	$s_{20,w}$ (S)
EB1	64 359	3.7
p150GluedN	23 723	1.6
EB1•p150GluedN	111 805	4.2

Avogadro's number, f the frictional coefficient, D the diffusion coefficient and R the gas constant.

The inclusion of the molecular parameter f offers the possibility to combine the Svedberg equation with Stokes equation (see Ref. 15) yielding an expression for the maximum s -value that can be obtained for a protein of given mass:

$$s_{sphere} = 0.012 \frac{M^{2/3} (1 - \bar{v}\rho)}{\bar{v}^{1/3}}$$

A compact sphere (with the volume of the true molecule and radius r_0) has the minimum frictional coefficient f_0 for a molecule with that given mass. The ratio of the experimental frictional coefficient f to the minimum frictional coefficient (f/f_0), measures the maximum shape asymmetry from a sphere and is equal to the ratio of the maximum s -value to the observed s -value ($s_{sphere}/s_{20,w}$). In case of EB1 the frictional ratio value calculated with the sedimentation constants is $f/f_0 = s_{sphere}/s_{20,w} = 5.7/3.7 = 1.9$. This relatively high shape asymmetry indicates that the EB1 dimer is not spherical.

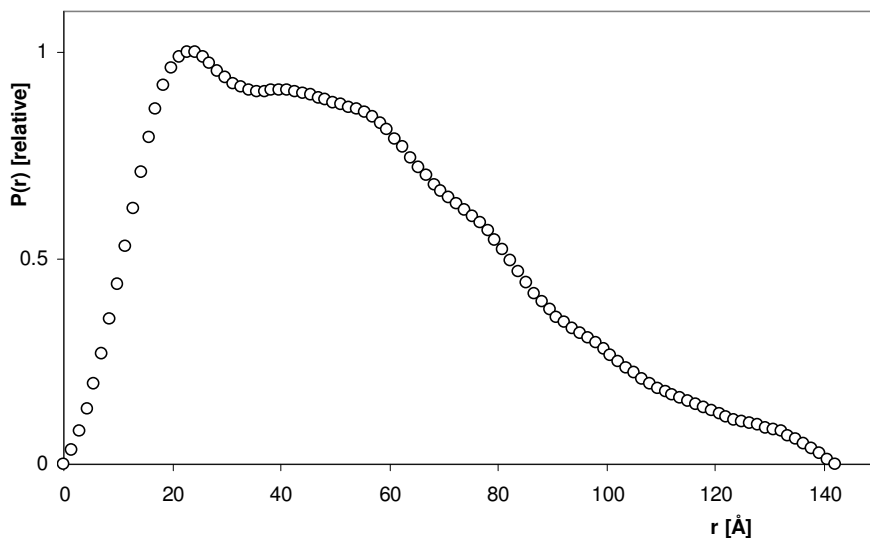


Figure 3 Distance distributions function, $P(r)$ versus r , for EB1.

An independent value of the frictional ratio is obtained from the elution behaviour of EB1 on the Superdex column since $ff/f_0 = R_s/r_0$ ²². As expected for a series of globular proteins a plot of $\log M_r$ versus the elution volume is a straight line. The point for the EB1 dimer deviates from this line (Figure 2) which indicates that its shape is not globular. The Stokes radius R_s is defined as the radius of a sphere that is hydrodynamically equivalent to the true molecule. A sphere of that radius would have the same frictional coefficient f as the molecule. The $R_s = 46 \text{ \AA}$ is read from the calibration line shown in Chapter 5 Figure S1 using the experimentally determined $K_{av} = 0.293$ for EB1. The r_0 calculated from the molecular weight and partial specific volume equals 26.6 \AA . Therefore $ff/f_0 = 1.7$.

Both the ultracentrifugation and gel filtration data consistently indicate that EB1 is a non-globular protein.

6.3.3 SAXS data

A real space representation of the SAXS data was obtained by indirect Fourier transform of the scattered intensities, $I(Q)$, using the GNOM program. The resulting $P(r)$ function is essentially a histogram of the distances between all possible pairs of points in the molecule, for each pair indicating the probability that the corresponding distance indeed occurs within the molecule. The $P(r)$ function for the EB1 dimer shown in Figure 3 clearly indicates that it is an asymmetrical particle.

Table II Experimentally determined structural parameters from solution scattering

Sample	R_g (Å)	D_{\max} (Å)
EB1	41.1 ± 0.5	140 ± 5
p150GluedN	24.9 ± 0.7	40 ± 1
EB1•p150GluedN	30.5 ± 1.5	145 ± 5

The overall structural parameters obtained from the EB1 scattering profile are $R_g = 41.1 \pm 0.5$ Å and $D_{\max} = 140 \pm 5$ Å. The D_{\max} value points at an elongated EB1 particle. The radius of gyration, R_g , is a geometric measurement defined in the same way as the radius of inertia in mechanics: the root-mean square of the distances of all the electrons of the particle from its centre of electronic mass²³. The analysis of the SAXS measurements on

the p150GluedN fragment and the EB1•p150GluedN complex is still in progress. However the preliminary structural parameters shown in Table 2 are consistent with what would be expected. Since complex formation does not result in a significantly larger D_{\max} for EB1, the added mass of the p150GluedN fragment must be located relatively close to the center of mass of the EB1 dimer. Consequently the R_g value for the complex is smaller compared to the EB1 dimer.

The 3D domain structure of EB1 was modelled on the basis of the SAXS data, using the high resolution models of the EB1 *En* and *Ec* domains employing the program Bunch. A simulated annealing protocol calculates the optimal positions and orientations of the domain structures and attaches dummy residues to the appropriate domain termini. The conformation of the dummy residues is adjusted to fit the experimental scattering data. Since the *Ec* domain shows P2 symmetry in the crystal structure, Bunch was run both with and without symmetry restrictions, point groups P1 and P2 respectively. The resulting P2 models converged to two populations. The first and major population showed *En* domains in close proximity to the 4-helix bundle of the *Ec* domain (Figure 4a). In the remainder (~ 40% of the models) the *En* domains were closer to the N-termini of the *Ec* domain (Figure 4b). The distance between the centers of gravity of the two *En* domains is approximately 80-90 Å in nearly all P2 models. This is strikingly close to the distance between two tubulin β -subunits along a microtubule protofilament. Without symmetry restrictions three sets of models were found. Next to the two solutions described above, a new asymmetric conformation appeared with one *En* domain close to the N-terminus of the

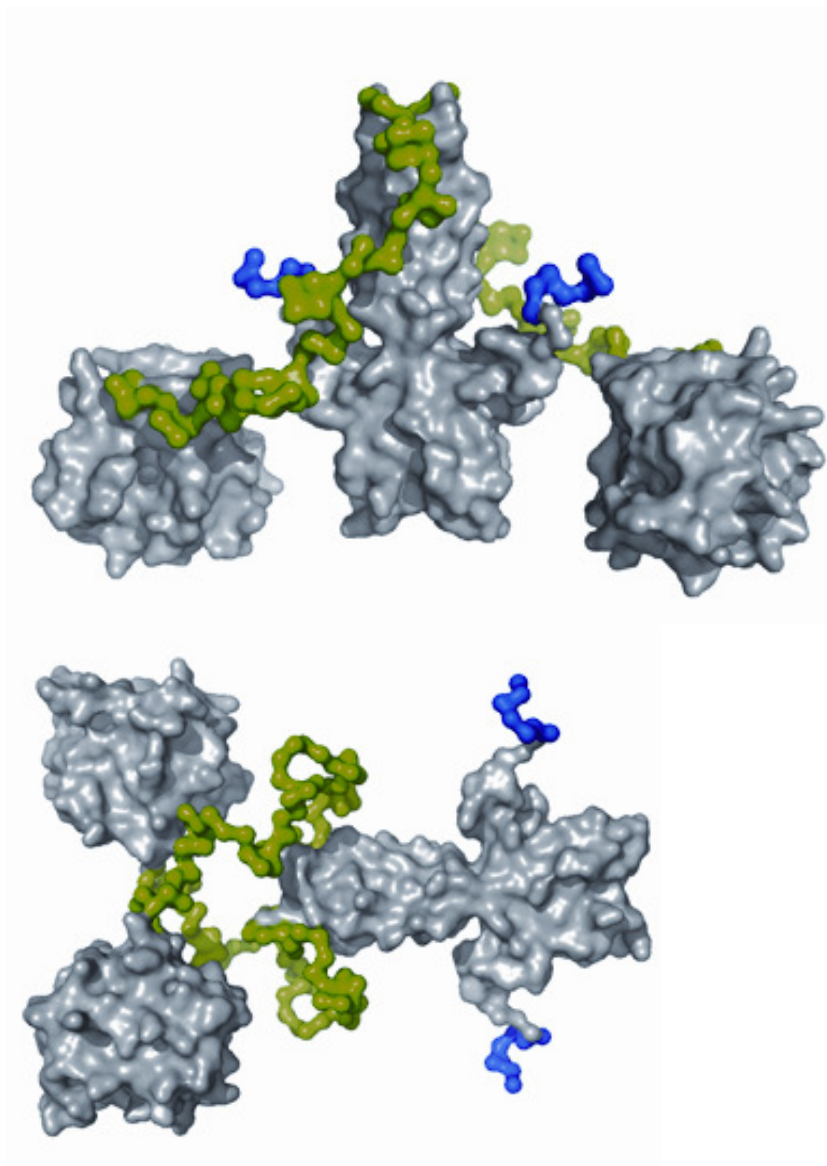


Figure 4 Comparison of representative examples of EB1 models obtained with SAXS data employing Bunch. The known structures of the two globular *En* and the rod-

shaped *Ec* domain are shown in grey, the linker domain in green and the C-terminal acidic tail in blue

Ec domain and the other *En* domain near the *Ec* C-terminal end. It has been shown before that GTP hydrolysis is required for plus-end tracking and it was suggested that EB1 specifically recognizes a distinct lattice structure at the growing MT end²⁴. Recently the antibody hMB11 specific for the GTP or GDP-P_i-bound tubulin conformation became available. In addition to the MT tip staining predicted by the classical GTP cap model, hMB11 labeled long stretches in areas where MTs formed bundles. Whether the GTP conformation is the cause or the consequence of bundling remained unknown. However, if the MTs retain the GTP conformation due to bundling specific binding proteins could be involved²⁵. It is interesting to note that EB1 has a bundling effect on MTs²⁶⁻²⁸. Our structural data suggest that EB1 binds to a dimer in a protofilament. EB1 could recognize the GTP or GDP-P_i-bound tubulin conformation in the MT like the antibody hMB11 does. Through binding EB1 could stabilize the GTP or GDP-P_i conformation and support the anchoring of a protofilament into the MT lattice. Further studies will be needed to characterize the precise localization of EB1 on microtubules. Since several conformations of EB1 are found using SAXS, further investigation of the domain orientation using other techniques, *e.g.* FRET or mild crosslinking followed by digestion and mass spectrometry, would be useful.

Acknowledgements

We are very grateful to Niels Galjart for providing us with the EB1 and p150GluedN constructs. We acknowledge the European Synchrotron Radiation Facility for provision of synchrotron radiation facilities and we would like to thank Dr Kristina Kvashnina and her colleagues for assistance in using beamline BM26. Wim Bras is gratefully acknowledged for useful discussions and advice. We thank Jasper Plaisier, Ramón López, Fernando Díaz for their help with the SAXS analysis and Carlos Alfonso for performing the analytical ultracentrifugation experiments.

References

1. Grishchuk, E.L., Molodtsov, M.I., Ataulkhanov, F.I., & McIntosh, J.R. (2005). Force production by disassembling microtubules. *Nature* **438**, 384-388.
2. Muller-Reichert, T., Chretien, D., Severin, F., & Hyman, A.A. (1998). Structural changes at microtubule ends accompanying GTP hydrolysis: information from a slowly hydrolyzable analogue of GTP, guanylyl (alpha,beta)methylenediphosphonate. *Proc. Natl. Acad. Sci. U. S. A* **95**, 3661-3666.
3. Gigant, B., Curmi, P.A., Martin-Barbey, C., Charbaut, E., Lachkar, S., Lebeau, L., Siavoshian, S., Sobel, A., & Knossow, M. (2000). The 4 Å X-ray structure of a tubulin:stathmin-like domain complex. *Cell* **102**, 809-816.
4. Caplow, M., Ruhlen, R.L., & Shanks, J. (1994). The free energy for hydrolysis of a microtubule-bound nucleotide triphosphate is near zero: all of the free energy for hydrolysis is stored in the microtubule lattice. *J. Cell Biol.* **127**, 779-788.
5. Howard, J. & Hyman, A.A. (2003). Dynamics and mechanics of the microtubule plus end. *Nature* **422**, 753-758.
6. Mandelkow, E.M., Mandelkow, E., & Milligan, R.A. (1991). Microtubule dynamics and microtubule caps: a time-resolved cryo-electron microscopy study. *J. Cell Biol.* **114**, 977-991.

7. Zovko, S., Abrahams, J.P., Koster, A.J., Galjart, N., & Mommaas, A.M. (2008). Microtubule plus-end conformations and dynamics in the periphery of interphase mouse fibroblasts. *Mol. Biol. Cell* **19**, 3138-3146.
8. Nogales, E. (2000). Structural insights into microtubule function. *Annu. Rev. Biochem.* **69**, 277-302.
9. Amos, L.A. & Schlieper, D. (2005). Microtubules and maps. *Adv. Protein Chem.* **71**, 257-298.
10. Galjart, N. & Perez, F. (2003). A plus-end raft to control microtubule dynamics and function. *Curr. Opin. Cell Biol.* **15**, 48-53.
11. Kreis, T. & Vale, R. (1999). *Guidebook to the cytoskeleton and motor proteins* London/New York: Oxford Univ. Press.
12. Lansbergen, G. & Akhmanova, A. (2006). Microtubule plus end: a hub of cellular activities. *Traffic.* **7**, 499-507.
13. Sandblad, L., Busch, K.E., Tittmann, P., Gross, H., Brunner, D., & Hoenger, A. (2006). The Schizosaccharomyces pombe EB1 homolog Mal3p binds and stabilizes the microtubule lattice seam. *Cell* **127**, 1415-1424.
14. Vitre, B., Coquelle, F.M., Heichette, C., Garnier, C., Chretien, D., & Arnal, I. (2008). EB1 regulates microtubule dynamics and tubulin sheet closure in vitro. *Nat. Cell Biol.* **10**, 415-421.
15. Lebowitz, J., Lewis, M.S., & Schuck, P. (2002). Modern analytical ultracentrifugation in protein science: A tutorial review. *Protein Science* **11**, 2067-2079.
16. Schuck, P. (2000). Size-distribution analysis of macromolecules by sedimentation velocity ultracentrifugation and lamm equation modeling. *Biophys. J.* **78**, 1606-1619.
17. Huang, T.C. X-ray powder diffraction analysis of silver behenate, a possible low-angle diffraction standard.
18. Boulin, C., Kempf, R., Koch, M.H.J., & McLaughlin, S.M. (1986). Data appraisal, evaluation and display for synchrotron radiation experiments: hardware and software. *Nucl. Instr. & Meth. in Phys. Res.* **249**, 399-407.
19. Chacon, P., Diaz, J.F., Moran, F., & Andreu, J.M. (2000). Reconstruction of protein form with X-ray solution scattering and a genetic algorithm. *J. Mol. Biol.* **299**, 1289-1302.

20. Semenyuk, A.V. & Svergun, D.I. (1991). GNOM- a program package for small-angle scattering data processing. *Journal of Applied Crystallography* **24**, 537-540.
21. Honnappa, S., John, C.M., Kostrewa, D., Winkler, F.K., & Steinmetz, M.O. (2005). Structural insights into the EB1-APC interaction. *EMBO J.* **24**, 261-269.
22. Bode, W., Engel, J., & Winklmer, D. (1972). A model of bacterial flagella based on small-angle x-ray scattering and hydrodynamic data which indicated an elongated shape of the flagellin protomer. *Eur. J. Biochem.* **26**, 313-327.
23. Guinier, A. & Fournet, G. (1955). *Small-Angle Scattering of X-rays*. Wiley, New York.
24. Dixit, R., Barnett, B., Lazarus, J.E., Tokito, M., Goldman, Y.E., & Holzbaur, E.L. (2009). Microtubule plus-end tracking by CLIP-170 requires EB1. *Proc. Natl. Acad. Sci. U. S. A* **106**, 492-497.
25. Dimitrov, A., Quesnoit, M., Moutel, S., Cantaloube, I., Pous, C., & Perez, F. (2008). Detection of GTP-tubulin conformation in vivo reveals a role for GTP remnants in microtubule rescues. *Science* **322**, 1353-1356.
26. Ligon, L.A., Shelly, S.S., Tokito, M., & Holzbaur, E.L. (2003). The microtubule plus-end proteins EB1 and dynactin have differential effects on microtubule polymerization. *Mol. Biol. Cell* **14**, 1405-1417.
27. Bu, W. & Su, L.K. (2001). Regulation of microtubule assembly by human EB1 family proteins. *Oncogene* **20**, 3185-3192.
28. Bu, W. & Su, L.K. (2003). Characterization of functional domains of human EB1 family proteins. *J. Biol. Chem.* **278**, 49721-49731.

Nederlandse samenvatting

Verschillende biologische systemen, zoals het 50S ribosomale Hsp15 complex, een schistosomiasis diagnostisch antigeen bindend antilichaam fragment (Fab 54-5C10-A), het zuurstof producerende enzym chloriet dismutase (Cld) en het belangrijke regulatoreiwit van microtubule dynamiek (EB1) zijn onderzocht met geavanceerde biochemische technieken. De structurele informatie verkregen met electronenmicroscopie (EM), kleine hoek verstrooiing van Röntgenstraling (SAXS) en Röntgendiffractie aan individuele eiwitkristallen werd aangevuld met informatie uit andere biofysische en biochemische methoden, zoals kolom chromatografie, gel elektroforese, oppervlakte plasmon resonantie (SPR), massa spectrometrie (MS) en electron paramagnetische resonantie (EPR).

Hoewel de in dit proefschrift beschreven biologische systemen uiteenlopen wat betreft chemische samenstelling, oorsprong en biologische functie, is er juist ook gekeken naar een gemeenschappelijk kenmerk: geïnduceerde conformatieveranderingen binnen het eiwit, eiwit-RNA of eiwit-carbohydraat complex.

In het geval van het ribosomale 50S gedeelte, wat ontstaat als een translaterend bacterieel ribosoom uiteenvalt door bijvoorbeeld temperatuursverhoging, zorgt het relatief kleine eiwit Hsp15 door binding met de 50S subeenheid voor een essentiële verandering. In hoofdstuk 2 wordt beschreven hoe het tRNA door Hsp15 wordt gestabiliseerd in de P-locatie waardoor de A-locatie beschikbaar komt voor een release factor. De

Nederlandse samenvatting

release factor kan nu de laatste peptidyl-tRNA binding van de onvoltooide eiwitketen hydrolyseren waarna het vrije polypeptide en het tRNA molecuul kunnen wegdiffunderen van de 50S subeenheid. Het 50S RNA-eiwitcomplex is dan gereed voor hergebruik als belangrijkste component van het ribosoom.

Hoofdstuk 3 heeft een toegepaste, praktische achtergrond. Het geeft een beschrijving van de kristalstructuur van het antilichaam fragment wat wordt gebruikt om de diagnose te stellen van de tropische, parasitaire ziekte schistosomiasis (ook wel bilharzia genoemd). Uit de oppervlakte plasmon resonantie experimenten blijkt dat de aanwezigheid van tenminste drie Lewis X eenheden een vereiste is voor de vorming van een antilichaam-antigen complex. De kristalstructuur, in combinatie met docking studies, laat zien hoe het betreffende antilichaam 54-5C10-A een trimeer Lewis X suiker kan binden. Analyse van de stabiliserende interacties tussen eiwit en koolhydraat maakt duidelijk dat niet alleen alle zes CDRs maar ook alle drie opeenvolgende Lewis X eenheden een rol spelen bij de complexvorming. Het lijkt erop dat ook ketens die bestaan uit meer dan drie repeterende Lewis X zouden kunnen binden, een conformatieverandering van CDR-H3 zou ervoor kunnen zorgen dat de bindingsplaats verruimd wordt. Van andere antilichamen is bekend dat CDR-H3 wel tot 15 Å kan opschuiven.

In hoofdstuk 4 en 5 komt een conformatieverandering ter sprake die van geheel andere orde is. In deze twee hoofdstukken wordt het Cld enzym beschreven, een eiwit wat op een uiterst effectieve manier de giftige stof chloriet omzet in de alledaagse, onschadelijke stoffen zuurstof en chloride. Voor de bacterie waaruit Cld het eerst gezuiverd is, *Azospira oryzae*, is dit

enzym essentieel om chloriet onschadelijk te maken. Dit chloriet wordt gevormd als metabolisch tussenproduct wanneer de bacterie perchloraat of chloraat gebruikt als electronenacceptor. In het eiwitkristal blijkt Cld als hexamere ring voor te komen, terwijl het in oplossing een pentameer is. Hoogstwaarschijnlijk zorgt één van de componenten die nodig is voor het kristalliseren van Cld, thiocynaat, ervoor dat de quaternaire toestand verandert.

Hoofdstuk 6 beschrijft de lage resolutie structuur van het eiwit EB1. In de literatuur is gesuggereerd dat een gedeelte van een belangrijk motoreiwitcomplex wat bindt aan EB1, p150Glued, de EB1 conformatie zou kunnen veranderen. Dus is ook het complex van EB1 met bindende gedeelte van p150Glued gezuiverd. De lage resolutie structuur van dit EB1•p150GluedN complex laat zien dat er geen grote conformatieverandering plaatsvindt ten opzichte van de EB1 structuur. Met de gebruikte SAXS techniek kunnen geen hoge resolutie structuren verkregen worden, maar wel kunnen bijvoorbeeld kristalstructuren in de SAXS electronendichtheidsmap gefit worden. Als dit gedaan wordt met de kristalstructuur van het microtubulus bindende domein van EB1, blijkt de afstand tussen deze twee identieke domeinen in de EB1 dimeer overeen te komen met 80 tot 90 Å. Dit benadert de afstand tussen naast elkaar gelegen tubuline β -subeenheden in een protofilament van een microtubulus.

General acknowledgements

The research described in this thesis was realized with the invaluable help of several people. I would like to thank all co-authors, who are listed elsewhere in this booklet, in the first place. My special gratitude goes to Ellen Thomassen. You were supportive in all possible aspects of the research including the production of artwork for the publications. Marike, many thanks for your explanation and advice relating to the antibody research. I appreciated the help of all other BFSC, MolGen and BC group members.

I am obliged to Nora Goosen for the possibility to join her group temporarily and to Marian van Kesteren for the technical input while performing the protein purification work at the start of my PhD.

Sometimes help appeared unexpectedly, for example when Bert Jansen lended a hand with data collection on a Cld crystal. That really accelerated the structure solution progress.

I would like to thank Jasper Plaisier, Ramón López, Ruth Matesanz and Fernando Díaz for their help with the SAXS analysis and Wim Bras for his advice on the SAXS measurements. Carlos Alfonso is acknowledged for performing the analytical ultracentrifugation experiments. I enjoyed the motivating discussions during the Molecule to Cell meetings and the nocturnal tubulin purifications in Rotterdam.

Mijn moeder, de rest van mijn familie, schoonfamilie en vrienden wil ik graag heel erg bedanken voor hun voortdurende interesse in de voortgang van het onderzoek. Dat helpt!

Tenslotte, last but definitely not least, lieve Annemieke: heel erg bedankt voor je onvoorwaardelijke steun en vertrouwen tijdens de afgelopen jaren. Het is alleen wel wat vreemd dit onder 'general' te verwoorden..

List of publications

- de Geus, D.C.**, Thomassen, E.A.J., Hagedoorn, P.L., Pannu, N.S., van Duijn, E. & Abrahams, J.P. (2009) Crystal structure of chlorite dismutase, a detoxifying enzyme producing molecular oxygen. *J. Mol. Biol.* **387**, 192-206.
- de Geus, D.C.**, van Roon, A.M.M., Thomassen, E.A.J., Hokke, C.H., Deelder, A.M. & Abrahams, J.P. (2009) Characterization of a diagnostic Fab fragment binding trimeric lewis X. *Proteins: Structure, Function, and Bioinformatics* (in press)
- Jiang, L., Schaffitzel, C., Bingel-Erlenmeyer, R., Ban, N., Korber, P., Koning, R.I., **de Geus, D.C.**, Plaisier, J.R., & Abrahams, J.P. (2008) Recycling of Aborted Ribosomal 50S Subunit-Nascent Chain-tRNA Complexes by the Heat Shock Protein Hsp15. *J. Mol. Biol.* **386**, 1357-67.
- de Geus, D.C.**, Thomassen, E.A.J., van der Feltz, C.L., & Abrahams, J.P. (2008) Cloning, expression, purification, crystallization and preliminary X-ray diffraction analysis of chlorite dismutase: a detoxifying enzyme producing molecular oxygen. *Acta Crystallogr. Sect. F. Struct. Biol. Cryst. Commun.* **64**, 730-732.
- Hartley, A., Glynn, S.E., Barynin, V., Baker, P.J., Sedelnikova, S.E., Verhees, C., **de Geus, D.C.**, van der Oost, J., Timson, D.J., Reece, R.J., & Rice, D.W. (2004) Substrate specificity and mechanism from the structure of *Pyrococcus furiosus* galactokinase. *J. Mol. Biol.* **337**, 387-398.
- Akerboom, J., Turnbull, A.P., Hargreaves, D., Fisher, M., **de Geus, D.C.**, Sedelnikova, S.E., Berrisford, J. M., Baker, P.J., Verhees, C.H., van der Oost, J., & Rice, D.W. (2003) Purification, crystallization and preliminary crystallographic analysis of phosphoglucose isomerase from the hyperthermophilic archaeon *Pyrococcus furiosus*. *Acta Crystallogr. D. Biol. Crystallogr.* **59**, 1822-1823.
- Berrisford, J.M., Akerboom, J., Turnbull, A.P., **de Geus, D.C.**, Sedelnikova, S.E., Staton, I., McLeod, C.W., Verhees, C.H., van der Oost, J., Rice, D.W., & Baker, P.J. (2003). Crystal structure of *Pyrococcus furiosus* phosphoglucose isomerase. Implications for substrate binding and catalysis. *J. Biol. Chem.* **278**, 33290-33297.
- de Geus, D.C.**, Hartley, A.P., Sedelnikova, S.E., Glynn, S.E., Baker, P.J., Verhees, C.H., van der Oost, J., & Rice, D.W. (2003) Cloning, purification, crystallization and preliminary crystallographic analysis of galactokinase from *Pyrococcus furiosus*. *Acta Crystallogr. D. Biol. Crystallogr.* **59**, 1819-1821.
- Hagedoorn, P.L., **de Geus, D.C.**, & Hagen, W.R. (2002). Spectroscopic characterization and ligand-binding properties of chlorite dismutase from the chlorate respiring bacterial strain GR-1. *Eur. J. Biochem.* **269**, 4905-4911.

Curriculum vitae

Daniël de Geus was born in Utrecht, the Netherlands on the 26th of June 1977. Immediately after his secondary education at College Blaucapel in Utrecht (1989-1995) he joined the Wageningen University. During his study Molecular Sciences he chose the combined microbiological/biochemical specialization. The master thesis 'Purification and characterization of chlorate respiration key enzymes from bacterial strain GR-1' was written about a research project conducted at the Bioinorganic Chemistry group, supervised by Prof. dr W.R. Hagen and Ir P.L. Hagedoorn. From November 1998 until December 1999 he was a member of the executive committee of Integrand Wageningen. In November 2000 he left Wageningen to perform a 7 months research project at the Department of Molecular Biology and Biotechnology, Krebs Institute for Biomolecular Research, University of Sheffield, England under supervision of Prof. dr D.W. Rice and Dr J. van der Oost. This yielded a second master thesis about the purification, crystallization and X-ray diffraction of three thermostable sugar converting enzymes. Following this, he started to assist the editors of the books 'Economics of Sustainable Energy in Agriculture' (November 2001-April 2002) and 'Risk and Uncertainty in Environmental and Resource Economics' (December 2002-May 2003). Meanwhile he earned his Master of Science degree in January 2003.

In November 2003 he started his PhD at Leiden University in the Biophysical Structural Chemistry department, headed by Prof. dr J.P. Abrahams. His research focused on 3D structure determination of proteins employing X-ray crystallography and small-angle X-ray solution scattering. Some results described in this thesis were produced as part of collaborations with the ETH (Zürich, Switzerland), the LUMC (Leiden, the Netherlands), the LMU (München, Germany), the Delft University of Technology (the Netherlands), the Netherlands Proteomics Center (Utrecht) and the CIB (Madrid, Spain).

As of April 2009 Daniël is employed as a Postdoc researcher on the disturbed heparan sulphate biosynthesis in osteochondroma. This research is a joint project of Leiden University and the LUMC.